[redacted]

[redacted]

M[redacted]ER

Accession No. 10343-65

Copy No. 28

SID 65-1353

FINAL REPORT

STUDY OF FLOW FIELDS ABOUT AXISYMMETRIC BLUNT BODIES AT LARGE ANGLE-OF-ATTACK

(Contract No. NAS9-3159)

29 October 1965

Prepared by

Flight Sciences Department

Approved by

H. G. Webb, Jr.
Project Manager
Gasdynamics Analysis Projects

F. J. Lyon
Chief
Aero-Thermodynamics

NORTH AMERICAN AVIATION, INC.
SPACE and INFORMATION SYSTEMS DIVISION

FOREWORD

This document represents a final report prepared for the Manned Spacecraft Center, National Aeronautics and Space Administration, Houston, Texas presenting the results of a study conducted between July 1964 and November 1965 by the Space and Information Systems Division of North American Aviation, Inc., under Contract NAS9-3159, Study of Flow Fields About Axisymmetric Blunt Bodies at Large Angle-of-Attack.

The use and organization of the computer program are documented in a separate Computer Program Operating Manual, SID 65-1355, in three volumes. The theoretical formulation of the basic method is presented in this report.

This study was performed by the Flight Sciences Department of the S&ID Research and Engineering Division under the direction of H. G. Webb, Jr., Program Manager. The following individuals contributed significantly to this study in the areas indicated: H. S. Dresser, overall development of the computer program; B. K. Adler, formulation of the analytic shock fit, the iterative convergence technique, and the data output options; R. H. C. Lee, basic theoretical formulations; and S. A. Waiter, analysis of the Apollo Command Module entry flow field. Particular appreciation is due R. B. Anderson, N. Rosenblatt, and J. Wallen for their contributions in programming the analysis and in subsequent checkout.

TECHNICAL REPORT INDEX/ABSTRACT

ACCESSION NUMBER	DOCUMENT SECURITY CLASSIFICATION
10343-65	UNCLASSIFIED

TITLE OF DOCUMENT

FINAL REPORT - STUDY OF FLOW FIELDS ABOUT AXISYMMETRIC BLUNT BODIES AT LARGE ANGLE-OF-ATTACK

LIBRARY USE ONLY

AUTHOR(S)

H. G. WEBB, JR.

CODE	ORIGINATING AGENCY AND OTHER SOURCES	DOCUMENT NUMBER
	NAA, S&ID	SID 65-1353

PUBLICATION DATE	CONTRACT NUMBER
29 OCTOBER 1965	NAS9-3159

DESCRIPTIVE TERMS

*ANGLE OF ATTACK, *AXISYMMETRIC, *BLUNT BODIES, *FLOW FIELD, *INVERSE METHOD, *REAL GASES

ABSTRACT

An IBM 7094 computer program has been developed for the calculation of equilibrium, real gas inviscid flow fields about axisymmetric blunt bodies at large angles-of-attack traveling at supersonic speeds. The program will compute the subsonic and transonic flow regions behind the detached bow shock with sufficient supersonic data being generated to allow initiation of a method-of-characteristics solution for the remainder of the flow field.

An inverse method was chosen as the basic method. Starting from an initial estimate of the shock shape, the flow field and resulting body are found. The computed body is compared geometrically with the desired body to establish a set of control point errors. By sequentially perturbing the analytic shock coefficients, a set of influence coefficients is found which is then used to compute shock coefficient corrections which reduce the control point errors in a corrected flow field run. This procedure is convergent if the initial shock shape is sufficiently close to the exact shock shape. The program will handle the Apollo Command Module, as well as a general class of body shapes.

This report presents a detailed derivation of the theoretical formulation, an explanation of the numerical procedures used in the finite difference solution, followed by sample results for two cases, one of which is the Apollo Command Module in a real gas flow at 22° angle-of-attack.

FORM 131-V REV. 6-64

SUMMARY

Based on a thorough review of existing methods for the computation of inviscid subsonic-transonic real gas flow fields over blunt axisymmetric bodies traveling at supersonic speed at high angle-of-attack, the inverse method was selected for the development of an IBM 7094 computer program for calculation of flow fields over the Apollo Command Module and a generalized class of shapes. The program was checked out on several sample cases, two of which are documented herein. One of these is the real gas angle-of-attack flow field over the Apollo Command Module.

A minimum number of assumptions were made in formulating the computer program from the exact partial differential equations. The only major assumption made in the analytical development of the solution was the use of a finite difference technique in the numerical analysis. An accurate empirically fitted set of equations was used to represent real air properties. In the inverse method, the flow field and predicted body shape result from the integration of flow properties marching to the body in a body-oriented cylindrical coordinate system from an assumed or predicted bow shock wave. An analytic shock fit using up to 20 coefficients was developed which proved very accurate in representing a wide range of blunt body detached shocks. An automatic iteration procedure, required in this approach, was developed for correcting the shock to obtain the correct body shape. This procedure is based on the assumption that the initial shock shape is sufficiently close to the correct shape so that the necessary corrections in the coefficients of the analytic shock equation result in linearly related corrections in the coordinates of a set of body control points.

A sample case was chosen for the program development period as a check on the formulation and programming. Since sphere flow fields have already been accurately computed and reported in the open literature, this shape and shock were rotated 40 degrees to obtain the input conditions for a perfect gas angle-of-attack case. Typical results are presented herein. The real gas Apollo Command Module flow field results are presented to show the ability of the program to accurately predict the entire subsonic flow field at an angle-of-attack of 22 degrees, including the region near the small shoulder radius on this capsule shape.

In addition to the formulation of an analytic shock fit and the iterative convergence technique, the two chief technical problems solved were the handling of instabilities in the flow calculations and the coupling of a body determination routine into the finite difference integration procedure. The instability problem was solved by establishing two tests for removable singularities and by using a two-dimensional smoothing procedure to overcome nonessential instabilities observed near the body axis of symmetry. Smoothing was not found to be required for the zero angle-of-attack case. The body

determination procedure predicts the body location by using a stream function, extrapolates to find body properties, and controls the deletion of calculations for grid points which fail the instability tests or which lie within the predicted body where calculations proved unreliable.

TABLE OF CONTENTS

Section	Page
FOREWORD	iii
ABSTRACT	v
SUMMARY	vii
INTRODUCTION	1
THEORETICAL FORMULATION	3
Principles of Inverse Method	3
Governing Equations	4
Conditions Behind Shock	17
Determination of Streamlines and Body Shape	22
Shock Shape Formulation	25
Iterative Convergence Technique	30
Instabilities and Data Smoothing	32
Thermodynamic Properties	38
COMPUTER PROGRAM DEVELOPMENT	41
General Description	41
Numerical Procedures	44
Data Output Program	80
SHOCK SHAPE PREDICTION	109
Curve Fitting Procedures	109
Shock Prediction for Sample Cases	115
RESULTS FOR SAMPLE CASES	121
Sphere, $\alpha = 40°$	121
Apollo, $\alpha = 22°$	121
Behavior of Iterative Convergence Technique	132
NOMENCLATURE	133
REFERENCES	139
APPENDIXES	141
A. Transformation of Conservation Equations in Vector Notation Into a Cylindrical Coordinate System	141
B. Investigation of the Influence Coefficient Method	145

ILLUSTRATIONS

Figure		Page
1	Typical Zero Angle-of-Attack Flow Field Over an Axisymmetric Blunt Body	3
2	Coordinate System	6
3	Definition of Transformed Lateral Velocities	11
4	Free-Stream Velocity Vector Components	18
5	Transformed Cartesian Coordinate System	27
6	Grid Point Locations in Cylindrical Coordinate System	35
7	Typical Property Variation in the Radial Direction	37
8	Orientation of Grid Points in Marching Plane	42
9	Description of Three-Point and Five-Point Finite Difference Fit	47
10	Typical Finite Difference Fit for Lateral Derivatives	52
11	Variation of Stream Functions in x Direction	53
12	Streamline Behavior Near the Body Surface	54
13	Measurement of Predicted Body Shape Errors	58
14	Location of Translation and Control Points	59
15	Definition of General Body Shape	63
16	General Body Shape with Hemispherical Nose	65
17	Apollo Command Module Shape	70
18	Symmetry Properties of Data About Pitch Plane	75
19	Treatment of Radial Distribution of Properties	76
20	Least Square Smoothing Parabola	77
21	Block Diagram of Data Output Program	82
22	Bounding Grid Points for Data Interpolation	85
23	Relative Coordinate System	88
24	Vector Relationships in Coordinate Transformation	90
25	Bounding K's and C_x	92
26	Bounding Grid Point within Body	94
27	Bounding Grid Points for Streamlines in Pitch Plane	97
28	Output at Specified Intervals	100
29	Streamline Trace on a Body Axis Projection	101
30	Definition of S_1, S_2, and S_3	112
31	Typical Radial Distribution of Parameters C_0, C_1, and C_2	113
32	Preliminary Apollo Command Module Shock Shape	116
33	Coordinate Transformation for Sphere Flow Field at Angle-of-Attack	117
34	Analytic Sphere Shock Shape	119
35	Pitch Plane and Frontal View of Flow Field for Sphere at 40° Angle-of-Attack ($\gamma' = 1.4$)	122
36	Flow Field in Plane $\theta = 45°/225°$ and $\theta = 90°/270°$, Sphere at 40° Angle-of-Attack ($\gamma' = 1.4$)	123
37	Pressure Distributions, Sphere at 40° Angle-of-Attack ($\gamma' = 1.4$)	124

Figure		Page
38	Flow Field Around Apollo Command Module, $\theta = 0°, 180°$	128
39	Flow Field Around Apollo Command Module, $\theta = 45°, 90°, 135°$	129
40	Body Pressure Distribution, Apollo Command Module	130
41	Body Surface Streamline Pattern, Apollo Command Module	131
42	Variation of Body Shape Parameters with R_S	149
43	Variation of Body Shape Parameters with A_{5S}	149
44	Variation of Body Shape Parameters with A_{7S}	150

TABLES

Table		Page
1	Comparison of Thermodynamic Properties of Real Air, $\log_{10}(\rho/\rho_0) = -2$	38
2	Apollo Analytic Shock Shape Coefficients	127
3	Smoothing Weighting Factors	127

INTRODUCTION

The determination of the fluid properties in the subsonic-transonic flow field over a blunt body has been the focus of numerous gasdynamic investigations. Not only does it provide the necessary data for the subsequent evaluation of the attenuation of electromagnetic signals through the shock layer and the radiant and convective heat transfer to the nose cap, but it also serves as an essential step toward initiating downstream supersonic flow field calculations. Past investigations in this area have dealt mostly with two-dimensional and axisymmetric bodies at zero angle-of-attack, mainly because of the simplification in the analysis for these cases. However, the flow field about a typical re-entry vehicle is generally three-dimensional; and, complex as it may appear, the calculation of three-dimensional flow fields has become a task of increasing urgency.

The objective of this study was to develop a computer program for calculating flow fields about axisymmetric blunt bodies at large angle-of-attack with a higher order approximation to the flow properties than the one presented in Reference 1 . The basic approach of Reference 1 was to use the method of integral relations with the following assumptions: 1) a number of flow properties vary linearly across the shock layer (Belotserkovski's one-layer method, Reference 2), and 2) the flow properties vary sinusoidally around the stagnation point.

Prior to undertaking this effort, a survey was conducted to determine the current state of the art in blunt body flow field analysis and to determine which approach should be taken to develop the required computer program. The methods presented in the literature are classified into two categories; the inverse and the direct methods. The inverse method assumes a known shock geometry and computes the entire flow field, including the body geometry. The direct method, on the other hand, uses a known body geometry, assumes additional information about the flow field properties, and iterates to a final converged solution. Examples of the inverse method are those of Fuller (Reference 3), and Lomax and Inouye (Reference 4) in which instabilities in the calculations are removed by smoothing. Garabedian and Lieberstein (Reference 5) also solved the inverse problem, but in a complex plane where instabilities were not present. The direct approach has been used by Maslen and Moeckel (Reference 6), Gravalos, et al (Reference 7) and Ushida and Yasuhara (Reference 8), as well as in the work based on the method of integral relations.

The conclusion to use the inverse method with smoothing in the present study was reached after a review of these methods. The direct methods using the streamline curvature principle (References 6,7 and 8) cannot define the flow field accurately near the stagnation point. This drawback is troublesome for the three-dimensional case where the maximum entropy streamline does not necessarily coincide with the stagnation streamline. The method of

integral relations (even with two strips) may not yield enough flow field details to obtain accurate starting conditions for the solution of the supersonic flow region. The work of Bohachevsky, et al. (Reference 9) is a new promising formulation of the direct method that was presented after the decision was made to use the approach taken in this study. The inverse method has been used for two-dimensional blunt body flow field analysis using smoothing techniques and has proven to be both fast and accurate and is simpler than the method of Reference 5. The inverse method will yield sufficiently detailed flow fields, even in the vicinity of the stagnation point, without any assumption on the entropy of the stagnation streamline. Its chief drawback is its dependence on an advance knowledge of the shock shape. The approach used in the present study overcomes this deficiency by development of an automatic iterative technique for converging on the correct shock and body shape using a predicted shock shape for the initial conditions. If the predicted shock is sufficiently close to the correct shock the technique is convergent.

This report, supplemented by the Computer Program Operating Manual, Reference 10, describes the theoretical analysis and presents a detailed description of the formulation and operational use of the computer program developed for the calculation of the subsonic-transonic flow field about a blunt body of revolution at angle-of-attack. In order to simplify the computation, air is assumed to be either a perfect gas with constant specific heats or a real gas at thermodynamic and chemical equilibrium. The general approach described here can be extended to the case of nonequilibrium flow.

THEORETICAL FORMULATION

In the theoretical analysis of the inverse method angle-of-attack blunt body solution, many critical decisions must be made which will affect the formulation of the resulting computer program. Since the derivation must be based on a specific coordinate system, it is in order to give the choice of a suitable system a high priority. A body-oriented cylindrical system has advantages in this analysis because of its ability to handle axially symmetric body shapes. This system also has advantages at hypersonic speeds when the shock lies close to the body. Another item to consider is the high degree of accuracy required in the final results. This is extremely important in the inverse method. Thus, the approach taken herein is to derive the fundamental equations and then introduce a minimum number of necessary assumptions to simplify the analysis for programming.

Problem areas to consider include selection of an accurate analytic shock fit equation and exploration of a means of correcting the shock to obtain a more accurate body shape. The well-known problem of integration instability in numerical solutions using the inverse method is also of utmost importance. Although perfect gas thermodynamic properties offer no problem, a procedure for introducing equilibrium real air properties must be chosen.

PRINCIPLES OF THE INVERSE METHOD

The inverse method of solution computes the flow properties behind a given shock when free stream conditions and the thermodynamic properties of the gas are specified. It is desired to compute a solution which extends sufficiently into the supersonic region to allow a method-of-characteristics solution to be started. Consider the zero angle-of-attack flow field over an axisymmetric shape as shown in Figure 1 .

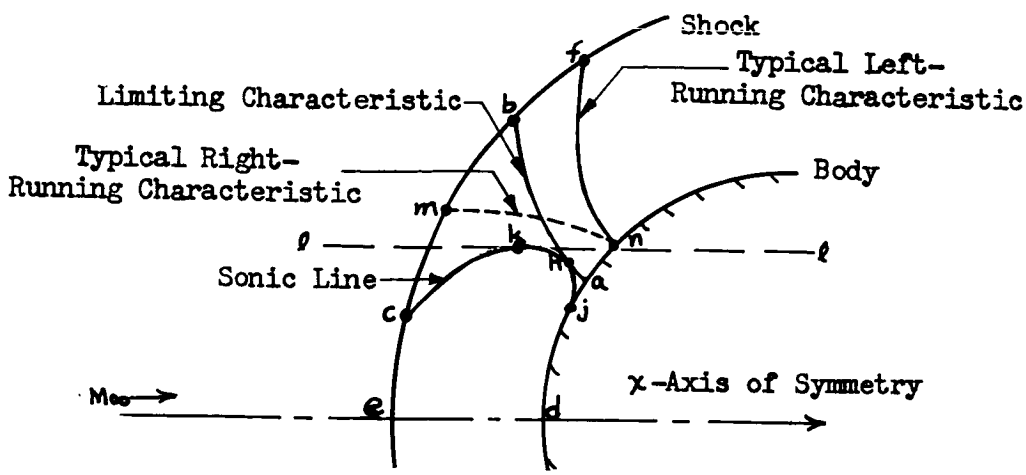

Figure 1. Typical Zero Angle-of-Attack Flow Field Over an Axisymmetric Blunt Body

The following discussion considers the free stream conditions and thermodynamic properties of the gas to be held constant. The features of the flow field are worth noting, for their understanding is important in establishing the operation of the inverse method.

1. The shock ecmb is analytic, and any segment of the curve can be continued to the entire curve.

2. The shock ecmb and the entire flow field eckhad are uniquely defined by the body shape dja. Since the converse is also true, it follows from analytic continuation that the body dja is determined uniquely from any segment of the shock ecmb.

3. The sonic line ckhj is also determined uniquely by any segment of the shock ecmb.

4. The segment of the sonic line jh uniquely defines the body segment ja, and the segment ch of the sonic line determines uniquely the flow in the region chbmc.

Since the body segment ja is defined by the sonic line segment jh, it is necessary to verify with the inverse method that the correct body shape ja is obtained before initiating the characteristics solution slightly downstream of the line ckha with the body shape na given.

Thus it may be stated that it is necessary to define the flow field in the region eckhad with the inverse method. The method of characteristics can then be used to solve for the region fbmchan. Note that the body shape may be altered downstream of point a without altering the flow upstream of the limiting characteristic ab.

The consequence of the existence of an analytic shock is that in principle the segment em of the shock is sufficient to start the inverse method. By marching in the x-direction, the required region will thus be computed; and the required data will be available for the characteristics solution. A difficulty arises, of course, in the numerical solution of the partial differential equations. Since a finite number of grid points are selected, for example, along the segment em, there exists an increasing loss of accuracy in the evaluation of higher order derivatives as the end of the array, point m, is approached. In practice the initial values must be prescribed somewhat past point m to allow accurate calculation of the required subsonic-supersonic flow field.

GOVERNING EQUATIONS

The subsonic-transonic flow field about a blunt body of revolution at a large angle-of-attack is to be considered. The resulting flow field in the shock layer will be three-dimensional with symmetry about the pitch plane. An inverse method has been chosen for the analysis. In this method, a shock shape is assumed; and the thermodynamic and flow properties in the shock layer are obtained from step-by-step integration of the governing equations, starting from the shock. The body supporting the assumed shock is obtained as part of the solution. With air assumed to be either a perfect gas with a constant

specific heat ratio or a real gas at thermodynamic equilibrium, the governing equations in the shock layer are the following:

Continuity: $$\nabla \cdot (\rho \vec{U}) = 0 \tag{1}$$

Momentum: $$\vec{U} \cdot \nabla \vec{U} = -\frac{1}{\rho} \nabla p \tag{2}$$

Energy: $$h + \frac{1}{2} \vec{U} \cdot \vec{U} = h_\infty + \frac{1}{2} U_\infty^2 \tag{3}$$

State: $$h = h(p, \rho) \tag{4}$$

A body-oriented cylindrical coordinate system has been chosen for this analysis. The reasons for this choice are:

1. The required body shapes are axially symmetric. The starting grid network of points on the shock is thus most suitably selected in a cylindrical system. The point spacing can be varied to result in satisfactory detail in property distributions over the body surface. For the Apollo shape, for example, the radial spacing can be easily reduced in the region of the smaller radius of curvature on the shoulder where properties will change rapidly over the surface.

2. The shock shape is more easily expressed analytically in a body-oriented cylindrical coordinate system.

3. Data output as required by the three options is facilitated in the cylindrical system.

This coordinate system is shown in Figure 2 in which the x-axis is the axis of the body, θ is the meridional angle measured from the x-y plane, and r is the distance perpendicular to the x-axis.

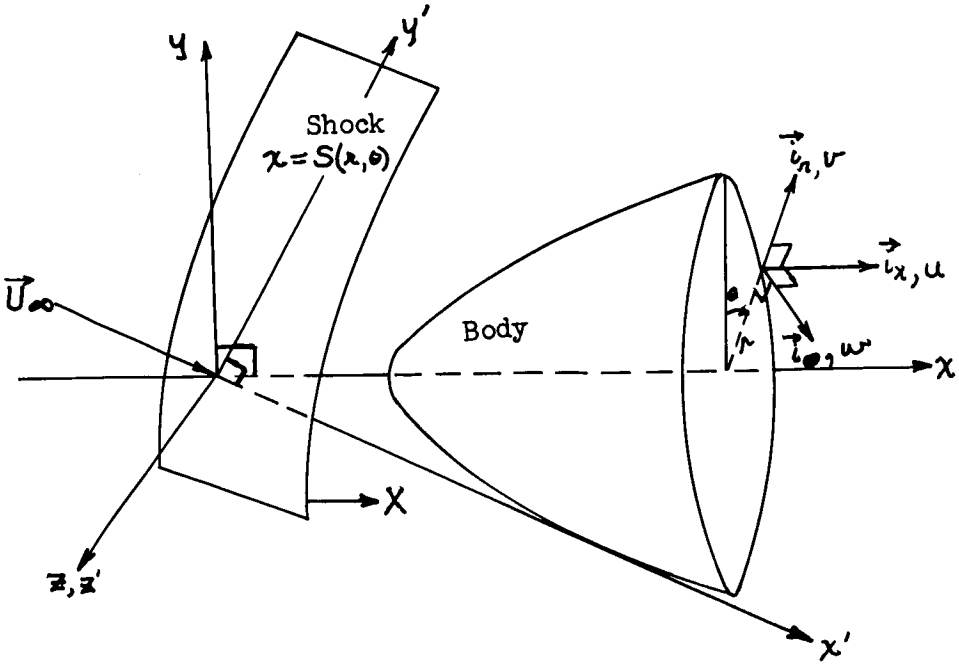

Figure 2. Coordinate System

In cylindrical coordinates, Equations (1) through (3) become

$$\frac{\partial}{\partial x}(\rho u) + \frac{1}{r}\frac{\partial}{\partial r}(r\rho v) + \frac{1}{r}\frac{\partial}{\partial \theta}(\rho w) = 0 \tag{5}$$

$$u\frac{\partial u}{\partial x} + v\frac{\partial u}{\partial r} + \frac{w}{r}\frac{\partial u}{\partial \theta} = -\frac{1}{\rho}\frac{\partial p}{\partial x} \tag{6}$$

$$u\frac{\partial v}{\partial x} + v\frac{\partial v}{\partial r} + \frac{w}{r}\frac{\partial v}{\partial \theta} - \frac{w^2}{r} = -\frac{1}{\rho}\frac{\partial p}{\partial r} \tag{7}$$

$$u\frac{\partial w}{\partial x} + v\frac{\partial w}{\partial r} + \frac{w}{r}\frac{\partial w}{\partial \theta} + \frac{vw}{r} = -\frac{1}{\rho r}\frac{\partial p}{\partial \theta} \tag{8}$$

$$h + \frac{1}{2}(u^2 + v^2 + w^2) = h_\infty + \frac{1}{2}U_\infty^2 \tag{9}$$

where u, v, w are the velocity components in the x, r, and θ directions, respectively. The details of this transformation are given in Appendix A.

For the convenience of numerical integration of the above partial differential equations, the coordinate system is transformed into a shear coordinate system in which the distance in the x direction is measured from the shock surface instead of from the y-z plane. This shear coordinate system is shown in Figure 2. Let the shock be described by:

$$x = S(r, \theta) \tag{10}$$

The transformation to the shear coordinate is

$$X = x - S(r, \theta) \tag{11}$$

$$r = r$$

$$\theta = \theta$$

The partial derivatives in the cylindrical system are related to those in the shear coordinates by

$$\left(\frac{\partial}{\partial x}\right)_{r,\theta} = \left(\frac{\partial}{\partial X}\right)_{r,\theta} \tag{12a}$$

$$\left(\frac{\partial}{\partial r}\right)_{x,\theta} = \left(\frac{\partial}{\partial r}\right)_{X,\theta} - \left(\frac{\partial S}{\partial r}\right)_{x,\theta}\left(\frac{\partial}{\partial X}\right)_{r,\theta} \tag{12b}$$

$$\left(\frac{\partial}{\partial \theta}\right)_{x,r} = \left(\frac{\partial}{\partial \theta}\right)_{X,r} - \left(\frac{\partial S}{\partial \theta}\right)_{x,r}\left(\frac{\partial}{\partial X}\right)_{r,\theta} \tag{12c}$$

Using Equation (12) and denoting a partial derivative by a subscript, Equations (4) through (9) become

$$r u_x - r S_r v_x - S_\theta w_x + \frac{Q \rho_x}{\rho} + r v_r + \frac{r v \rho_r}{\rho} + w_\theta + \frac{w \rho_\theta}{\rho} + v = 0 \tag{13}$$

$$Q u_x + r v u_r + w u_\theta = -\frac{r p_x}{\rho} \tag{14}$$

$$Q v_x + r v v_r + w v_\theta - w^2 = \frac{r p_r}{\rho} + \frac{r S_r p_x}{\rho} \tag{15}$$

$$Q w_x + r v w_r + w w_\theta + v w = -\frac{p_\theta}{\rho} + \frac{S_\theta p_x}{\rho} \tag{16}$$

$$h_p p_x + h_\rho \rho_x + u u_x + v v_x + w w_x = 0 \tag{17}$$

where Equation (9) has been differentiated with respect to x, and

$$Q \equiv r u - r v S_r - w S_\theta \quad ,$$

$$h_p \equiv \left(\frac{\partial h}{\partial p}\right)_\rho \quad ,$$

$$h_\rho \equiv \left(\frac{\partial h}{\partial \rho}\right)_p$$

It should be noted that the r and θ partial derivatives above are taken with x holding constant instead of χ. Equations (13) through (17) consist of five partial differential equations for the solutions of the five dependent variables: u, v, w, ρ, and p. These equations can be further rearranged into the following forms suitable for the step-by-step integration scheme:

For equilibrium air,

$$p_x = \left\{ Q^2\left(h_p - \frac{1}{\rho}\right) + h_\rho\left(r^2 + r^2 S_r^2 + S_\theta^2\right)\right\}^{-1} \cdot \tag{18}$$

$$\left\{(Qu - r\rho h_\rho)(rvu_r + wu_\theta) + (Qv + r\rho h_\rho S_r)\left(rvv_r + wv_\theta + \frac{rp_r}{\rho} - w^2\right)\right.$$

$$\left. + (Qw + \rho h_\rho S_\theta)\left(rvw_r + ww_\theta + \frac{p_\theta}{\rho} + vw\right) + \rho Q h_\rho\left(rv_r + w_\theta + \frac{rv\rho_r}{\rho} + \frac{w\rho_\theta}{\rho} + v\right)\right\}$$

$$u_x = -\frac{1}{Q}\left[rvu_r + wu_\theta + \frac{rp_x}{\rho}\right] \tag{19}$$

$$v_x = -\frac{1}{Q}\left[rvv_r + wv_\theta + \frac{rp_r}{\rho} - w^2 - \frac{rS_r p_x}{\rho}\right] \tag{20}$$

$$w_x = -\frac{1}{Q}\left[rvw_r + ww_\theta + \frac{p_\theta}{\rho} + vw - \frac{S_\theta p_x}{\rho}\right] \tag{21}$$

$$\rho_x = -\frac{\rho}{Q}\left[ru_x - rv_x S_r - w_x S_\theta + rv_r + \frac{rv\rho_r}{\rho} + w_\theta + \frac{w\rho_\theta}{\rho} + v\right] \tag{22}$$

For a perfect gas with constant γ, we have

$$h = \frac{\gamma}{\gamma - 1}\frac{p}{\rho} \tag{23}$$

therefore,

$$h_p = \left(\frac{\gamma}{\gamma - 1}\right)\frac{1}{\rho} \tag{24}$$

$$h_\rho = -\left(\frac{\gamma}{\gamma - 1}\right)\frac{p}{\rho^2} \tag{25}$$

Substituting Equations (24) and (25) into Equation (18) and rearranging, we obtain

$$\begin{aligned} p_x = {} & \left\{-\frac{Q^2\rho}{\gamma p} + \left(r^2 + r^2 S_r^2 + S_\theta^2\right)\right\}^{-1} \\ & \left\{\left(-r\rho - \frac{\gamma-1}{\gamma}\frac{\rho^2 Q u}{p}\right)\left(r v u_r + w u_\theta\right) + \left(r\rho S_r - \frac{\gamma-1}{\gamma}\frac{\rho^2 Q v}{p}\right) \cdot \right. \\ & \left(r v v_r + w v_\theta + \frac{r p_r}{\rho} - w^2\right) + \left(\rho S_\theta - \frac{\gamma-1}{\gamma}\frac{\rho^2 Q w}{p}\right) \cdot \\ & \left. \left(r v w_r + w w_\theta + \frac{p_\theta}{\rho} + v w\right) + \rho Q\left(r v_r + w_\theta + \frac{r v \rho_r}{\rho} + \frac{w \rho_\theta}{\rho} + v\right)\right\} \end{aligned} \tag{26}$$

The formulation actually used in the program requires one additional transformation of variables. It will be shown in a later section that a data smoothing procedure is required to control noise buildup in the data as the X integration proceeds toward the body. To most accurately smooth the data near the X axis $(r = 0)$ it is desirable to introduce the velocity components $\bar{v}$ and $\bar{w}$, defined in Figure 3 and by the following equations.

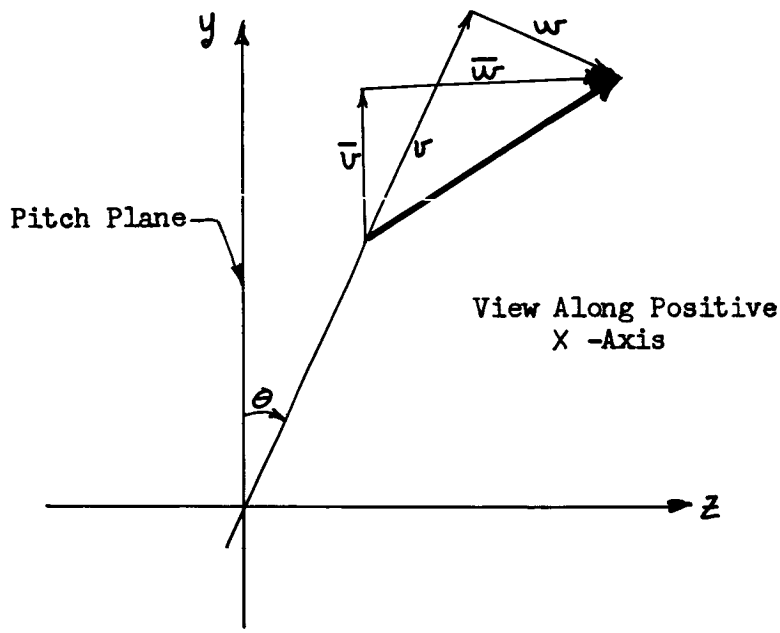

Figure 3. Definition of Transformed Lateral Velocities

$$\bar{v} = v \cos\theta - w \sin\theta \tag{27}$$

$$\bar{w} = v \sin\theta + w \cos\theta \tag{28}$$

These variables have the desirable characteristic that only one value of each exists on the X-axis $(r = 0)$ whereas the components v and w are also functions of the coordinate θ. Thus the components $\bar{v}$ and $\bar{w}$ are only slightly dependent on θ near the axis (where the noise is greatest) and can be smoothed with the least error.

The transformation of the X-derivative equations is readily accomplished by deriving expressions for v and w and their r, θ, and X-derivatives in terms of $\bar{v}$ and $\bar{w}$ and their r, θ, and X-derivatives.

Equations (27) and (28), when solved for w and v yield,

$$v = \bar{v} \cos\theta + \bar{w} \sin\theta$$

and

$$w = \bar{w} \cos\theta - \bar{v} \sin\theta$$

Straightforward differentiation of these expressions with respect to r, θ, and X yield the following derivative transformations,

$$v_r = \bar{v}_r \cos\theta + \bar{w}_r \sin\theta$$

$$v_\theta = -\bar{v} \sin\theta + \bar{v}_\theta \cos\theta + \bar{w} \cos\theta + \bar{w}_\theta \sin\theta$$

$$v_X = \bar{v}_X \cos\theta + \bar{w}_X \sin\theta$$

$$w_r = -\bar{v}_r \sin\theta + \bar{w}_r \cos\theta$$

$$w_\theta = -\bar{v} \cos\theta - \bar{v}_\theta \sin\theta - \bar{w} \sin\theta + \bar{w}_\theta \cos\theta$$

$$w_X = -\bar{v}_X \sin\theta + \bar{w}_X \cos\theta$$

The derivatives of the expressions for $\bar{v}_x$ and $\bar{w}_x$ require the solution of two simultaneous algebraic equations. Otherwise the transformation involves only straight substitution. The results are,

$$Q = r u - r S_r (\bar{v} \cos\theta + \bar{w} \sin\theta) - S_\theta (\bar{w} \cos\theta - \bar{v} \sin\theta) \quad (29)$$

$$p_x = \left\{ Q^2 \left(h_p - \frac{1}{\rho}\right) + h_\rho \left(r^2 + r^2 S_r^2 + S_\theta^2\right) \right\}^{-1} \cdot \quad (30)$$

$$\Big\{ \left[Qu - r\rho h_\rho\right]\left[r u_r (\bar{v} \cos\theta + \bar{w} \sin\theta) + u_\theta (\bar{w} \cos\theta - \bar{v} \sin\theta)\right]$$

$$+ \left[Q(\bar{v} \cos\theta + \bar{w} \sin\theta) + r\rho h_\rho S_r\right]\Big[r(\bar{v} \cos\theta + \bar{w} \sin\theta)(\bar{v}_r \cos\theta + \bar{w}_r \sin\theta)$$

$$+ \bar{w} \cos\theta (\bar{v}_\theta \cos\theta + \bar{w}_\theta \sin\theta) - \bar{v} \sin\theta (\bar{v}_\theta \cos\theta + \bar{w}_\theta \sin\theta) + \frac{r p_r}{\rho}\Big]$$

$$+ \left[Q(\bar{w} \cos\theta - \bar{v} \sin\theta) + \rho h_\rho S_\theta\right]\Big[r(\bar{v} \cos\theta + \bar{w} \sin\theta)(\bar{w}_r \cos\theta - \bar{v}_r \sin\theta)$$

$$+ \bar{w} \cos\theta (-\bar{v}_\theta \sin\theta + \bar{w}_\theta \cos\theta) + \bar{v} \sin\theta (\bar{v}_\theta \sin\theta - \bar{w}_\theta \cos\theta) + \frac{p_\theta}{\rho}\Big]$$

$$+ \rho Q h_\rho \Big[r(\bar{v}_r \cos\theta + \bar{w}_r \sin\theta) - \bar{v}_\theta \sin\theta + \bar{w}_\theta \cos\theta$$

$$+ \frac{r \rho_r}{\rho}(\bar{v} \cos\theta + \bar{w} \sin\theta) + \frac{\rho_\theta}{\rho}(\bar{w} \cos\theta - \bar{v} \sin\theta)\Big]\Big\}$$

$$\rho_x = -\frac{\rho}{Q}\Big\{ r u_x - r S_r\left[\bar{v}_x \cos\theta + \bar{w}_x \sin\theta\right] - S_\theta\left[\bar{w}_x \cos\theta - \bar{v}_x \sin\theta\right] \tag{31}$$

$$+ r\left[\bar{v}_r \cos\theta + \bar{w}_r \sin\theta\right] + \frac{r\rho_r}{\rho}\left[\bar{v}\cos\theta + \bar{w}\sin\theta\right]$$

$$+ \left[-\bar{v}_\theta \sin\theta + \bar{w}_\theta \cos\theta\right] + \frac{\rho_\theta}{\rho}\left[\bar{w}\cos\theta - \bar{v}\sin\theta\right]\Big\}$$

$$u_x = -\frac{1}{Q}\left[r u_r\left(\bar{v}\cos\theta + \bar{w}\sin\theta\right) + u_\theta\left(\bar{w}\cos\theta - \bar{v}\sin\theta\right) + \frac{r p_x}{\rho}\right] \tag{32}$$

$$\bar{v}_x = -\frac{1}{Q}\Big[r\left(\bar{v}\cos\theta + \bar{w}\sin\theta\right)\bar{v}_r + \bar{w}\bar{v}_\theta \cos\theta - \bar{v}\bar{v}_\theta \sin\theta \tag{33}$$

$$+ \frac{r p_r \cos\theta}{\rho} - \frac{p_\theta \sin\theta}{\rho} - \frac{r S_r p_x \cos\theta}{\rho} + \frac{S_\theta p_x \sin\theta}{\rho}\Big]$$

$$\bar{w}_x = -\frac{1}{Q}\Big[r\left(\bar{v}\cos\theta + \bar{w}\sin\theta\right)\bar{w}_r + \bar{w}\bar{w}_\theta \cos\theta - \bar{v}\bar{w}_\theta \sin\theta \tag{34}$$

$$+ \frac{r p_r \sin\theta}{\rho} - \frac{r S_r p_x \sin\theta}{\rho} + \frac{p_\theta \cos\theta}{\rho} - \frac{S_\theta p_x \cos\theta}{\rho}\Big]$$

Equation (30) is applicable to the perfect gas case and the explicit equations for h_p and h_ρ; Equations (24) and (25) may be substituted directly as was demonstrated previously. The result for P_x is,

$$P_x = \left\{ \frac{1}{-\frac{Q^2\rho}{\gamma P} + \left(r^2 + r^2 S_r^2 + S_\theta^2\right)} \right\} \cdot \tag{35}$$

$$\Big\{ \Big[-r\rho - \left(\frac{\gamma-1}{\gamma}\right)\frac{\rho^2 Q u}{P} \Big] \Big[r u_r \left(\bar{v}\cos\theta + \bar{w}\sin\theta\right) + u_\theta \left(\bar{w}\cos\theta - \bar{v}\sin\theta\right) \Big]$$

$$+ \Big[r\rho S_r - \left(\frac{\gamma-1}{\gamma}\right)\frac{\rho^2 Q}{P}\left(\bar{v}\cos\theta + \bar{w}\sin\theta\right) \Big] \Big[r\left(\bar{v}\cos\theta + \bar{w}\sin\theta\right) \cdot$$

$$\left(\bar{v}_r \cos\theta + \bar{w}_r \sin\theta\right) + \bar{w}\cos\theta\left(\bar{v}_\theta \cos\theta + \bar{w}_\theta \sin\theta\right)$$

$$- \bar{v}\sin\theta\left(\bar{v}_\theta \cos\theta + \bar{w}_\theta \sin\theta\right) + \frac{r P_r}{\rho} \Big]$$

$$+ \Big[\rho S_\theta - \left(\frac{\gamma-1}{\gamma}\right)\frac{\rho^2 Q}{P}\left(\bar{w}\cos\theta - \bar{v}\sin\theta\right) \Big] \Big[r\left(\bar{v}\cos\theta + \bar{w}\sin\theta\right) \cdot$$

$$\left(\bar{w}_r \cos\theta - \bar{v}_r \sin\theta\right) + \bar{w}\cos\theta\left(-\bar{v}_\theta \sin\theta + \bar{w}_\theta \cos\theta\right)$$

$$+ \bar{v}\sin\theta\left(\bar{v}_\theta \sin\theta - \bar{w}_\theta \cos\theta\right) + \frac{P_\theta}{\rho} \Big]$$

$$+ \rho Q \Big[r\left(\bar{v}_r \cos\theta + \bar{w}_r \sin\theta\right) + \bar{w}_\theta \cos\theta - \bar{v}_\theta \sin\theta$$

$$+ \frac{r\rho_r}{\rho}\left(\bar{v}\cos\theta + \bar{w}\sin\theta\right) + \frac{\rho_\theta}{\rho}\left(\bar{w}\cos\theta - \bar{v}\sin\theta\right) \Big] \Big\}$$

The numerical integration of the governing equations starts from the shock. With the values of p, ρ, u, v, and w specified by the shock relations which will be discussed in the next section, their derivatives with respect to r and θ can be numerically calculated. Equations (30) through (35) can then be applied to generate the X-derivatives.

These dependent variables can then be integrated in the X-direction to yield their values at a surface parallel to the shock surface. This process will be repeated until the entire body, including the body sonic line, is reached. The total velocity

$$U = \sqrt{u^2 + \bar{v}^2 + \bar{w}^2} \tag{36}$$

is calculated and subsequently used to compute the local Mach number at each point.

At each step of the forward integration, knowledge of p and ρ will be used to generate other thermodynamic properties such as enthalpy, h, entropy, s, temperature, T, and local Mach number, M. Thus, for the equilibrium air case, h, s, and T can be obtained from the existing S&ID equilibrium air subroutine. The equilibrium air speed of sound is

$$a_e^2 = \left(\frac{\partial p}{\partial \rho}\right)_s$$

The second Law of Thermodynamics can be expressed as

$$T\,ds = dh - \frac{1}{\rho}dp \tag{37}$$

The differential of h can be written as

$$dh = \left(\frac{\partial h}{\partial p}\right)_\rho dp + \left(\frac{\partial h}{\partial \rho}\right)_p d\rho$$

Substituting into (37), we obtain

$$T\,ds = \left[\left(\frac{\partial h}{\partial p}\right)_\rho - \frac{1}{\rho}\right] dp + \left(\frac{\partial h}{\partial \rho}\right)_p d\rho$$

From which one obtains,

$$a_e^2 = \frac{\left(\frac{\partial h}{\partial \rho}\right)_p}{\frac{1}{\rho} - \left(\frac{\partial h}{\partial p}\right)_\rho}$$

Thus the equilibrium local Mach number is given by

$$M_e = U\sqrt{\frac{\frac{1}{\rho} - h_p}{h_\rho}} \tag{38}$$

For a perfect gas, the thermodynamic properties can be calculated directly as follows:

$$T = \frac{p}{\rho R} \tag{39}$$

$$h - h_\infty = \frac{1}{2}\left(U_\infty^2 - u^2 - \bar{v}^2 - \bar{w}^2\right) \tag{40}$$

for any γ.

CONDITIONS BEHIND SHOCK

In this section, a method of determining the flow and thermodynamic properties behind an asymmetric shock will be described. The method is an extension of the usual oblique shock relations to the general three-dimensional case. Let the shock surface be described by the equation

$$g(x, r, \theta) = x - S(r, \theta) = 0 \tag{41}$$

and let $\vec{n}$ be a unit vector normal to the shock surface, as shown in Figure 4.

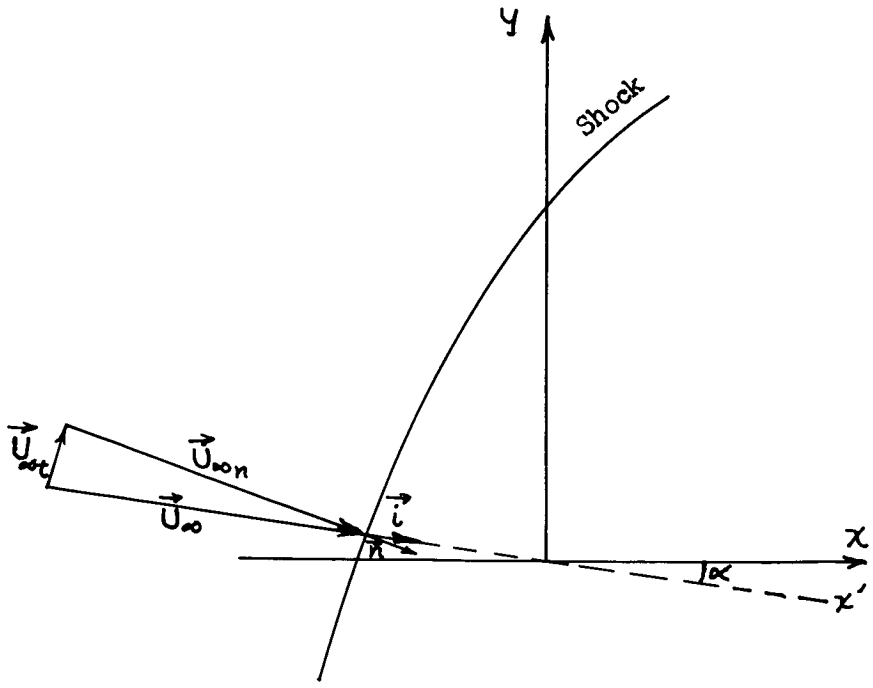

Figure 4. Free-Stream Velocity Vector Components

$$\vec{n} = \frac{\nabla g}{N} = \frac{1}{N}\left(\vec{i}_x - \vec{i}_r S_r - \vec{i}_\theta \frac{S_\theta}{r}\right) \tag{42}$$

where

$$N \equiv |\nabla g| = \left(1 + S_r^2 + \frac{S_\theta^2}{r^2}\right)^{\frac{1}{2}}$$

In order to apply the oblique shock relations, the free-stream velocity $\vec{U}_\infty$ is resolved into components normal and tangential to the shock surface. If $\vec{i}'$ is a unit vector in the free-stream direction (i.e., in the direction of the x'-axis of Figure 4), then

$$\vec{U}_\infty = \vec{i}' U_\infty \tag{43}$$

$$\vec{U}_{\infty_n} = \vec{n}\,(\vec{n}\cdot\vec{U}_\infty) = U_\infty \vec{n}\,(\vec{n}\cdot\vec{i}')$$

$$U_{\infty_n} = U_\infty\,(\vec{n}\cdot\vec{i}') \tag{44}$$

$$\vec{U}_{\infty_t} = \vec{U}_\infty - \vec{U}_{\infty_n} = U_\infty\left[\vec{i}' - \vec{n}(\vec{n}\cdot\vec{i}')\right] \tag{45}$$

$$U_{\infty_t} = \sqrt{U_\infty^2 - U_{\infty_n}^2} = U_\infty\sqrt{1-(\vec{n}\cdot\vec{i}')^2} \tag{46}$$

where $$\vec{i}' = \vec{i}_x \cos\alpha - \vec{i}_r \cos\theta \sin\alpha + \vec{i}_\theta \sin\theta \sin\alpha \tag{47}$$

and $\vec{U}_{\infty_n}$, $\vec{U}_{\infty_t}$, U_{∞_n}, U_{∞_t} are the normal and tangential components of the free-stream velocity vector and their magnitudes.

Substituting Equations (42) and (47) into Equations (43) through (46), we obtain

$$\vec{U}_{\infty_n} = \frac{U_\infty K}{N^2}\left(\vec{i}_x - \vec{i}_r S_r - \vec{i}_\theta \frac{S_\theta}{r}\right) \tag{48}$$

$$U_{\infty_n} = \frac{K\,U_\infty}{N} \tag{49}$$

$$\vec{U}_{\infty_t} = U_\infty\left\{\vec{i}_x\left(\cos\alpha - \frac{K}{N^2}\right) + \vec{i}_r\left(\frac{K S_r}{N^2} - \cos\theta\sin\alpha\right) + \vec{i}_\theta\left(\sin\theta\sin\alpha + \frac{K S_\theta}{N^2 r}\right)\right\} \tag{50}$$

$$U_{\infty_t} = U_\infty\left(1 - \frac{K^2}{N^2}\right)^{\frac{1}{2}} \tag{51}$$

where $$K \equiv \cos\alpha + S_r \cos\theta \sin\alpha - \frac{S_\theta}{r}\sin\theta\sin\alpha \tag{52}$$

Equations (48) through (52) are used in the following oblique shock relations to determine the flow and thermodynamic variables behind the shock, u_s, v_s, w_s, p_s, and ρ_s :

$$\rho_\infty U_{\infty_n} = \rho_s U_{s_n} \tag{53}$$

$$p_\infty + \rho_\infty U_{\infty_n}^2 = p_s + \rho_s U_{s_n}^2 \tag{54}$$

$$h_\infty + \frac{1}{2} U_\infty^2 = h_s + \frac{1}{2}\left(U_{s_n}^2 + U_{s_t}^2\right) \tag{55}$$

$$U_{\infty_t} = U_{s_t} \tag{56}$$

where the subscripts n and t denote the components normal and tangential to the shock surface. These oblique shock relations can be rearranged to give:

$$U_{s_n} = \epsilon\, U_{\infty_n} \tag{57}$$

$$p_s = p_\infty + \rho_\infty U_{\infty_n}^2 (1 - \epsilon) \tag{58}$$

$$h_s = h_\infty + \frac{U_{\infty n}^2}{2}\left(1 - \epsilon^2\right) \tag{59}$$

$$h_s = h_s\left(p_s, \rho_s\right) \tag{60}$$

and

$$\epsilon \equiv \frac{\rho_\infty}{\rho_s} \tag{61}$$

For equilibrium air, an iteration scheme is necessary for the solution of the above shock relations since h_s in Equation (60) is a complicated function of p_s and ρ_s. Corresponding to each value of ϵ, p_s and ρ_s can be determined from Equations (58) and (59) and h_s determined from Equation (60). Call this value h_s^*. Using the energy equation, Equation (59), another

value of the enthalpy can also be computed and denoted by h_s . The method of iterating on the shock properties consists of starting with an assumed density ratio, ϵ , and modifying this value until the two enthalpy curves (h vs. ϵ) cross one another. An alternating interpolation and extrapolation scheme is then used to converge on the value of ϵ which produces the condition $h_s^* - h_s = 0$.

For a perfect gas, iteration on the density ratio is not necessary since ϵ is explicitly given by the following equation:

$$\epsilon = \frac{\gamma - 1 + \frac{2\gamma p_\infty}{\rho_\infty U_{\infty n}^2}}{\gamma + 1} \tag{62}$$

The velocity components behind the shock can now be determined after a vector addition of Equations (48) and (50) has been made. Thus,

x -component
$$u_s = U_\infty \left\{ \cos\alpha - \frac{K}{N^2}(1-\epsilon) \right\} \tag{63}$$

r -component
$$v_s = U_\infty \left\{ -\cos\theta_s \sin\alpha + \frac{K S_r}{N^2}(1-\epsilon) \right\} \tag{64}$$

θ -component
$$w_s = U_\infty \left\{ \sin\theta_s \sin\alpha + \frac{K S_\theta}{N^2 r}(1-\epsilon) \right\} \tag{65}$$

The component velocities v_s and w_s are next transformed to $\bar{v}_s$ and $\bar{w}_s$ using Equations (27) and (28). These velocity components and the converged values of p_s and ρ_s completely specify the boundary conditions behind the shock and permit their r and θ derivatives to be determined numerically. Using Equations (30) through (35) in the previous section, the forward integration of the governing equations can then be initiated. Calculations of other thermodynamic properties behind the shock are carried out in exactly the same manner as described in the previous section.

DETERMINATION OF STREAMLINES AND BODY SHAPE

For the purpose of determining the streamline trajectories and the body shape, a pair of stream functions are introduced so as to satisfy the following relationship:

$$\nabla\phi \times \nabla\psi = \rho\vec{U} \tag{66}$$

By using the following identity

$$\nabla\cdot(\vec{g}\times\vec{h}) = (\nabla\times\vec{g})\cdot\vec{h} - (\nabla\times\vec{h})\cdot\vec{g}$$

with the assumption that

$$\vec{g} = \nabla\phi$$
$$\vec{h} = \nabla\psi$$

the divergence of $\rho\vec{U}$ may be written as

$$\nabla\cdot\rho\vec{U} = \nabla\cdot(\nabla\phi\times\nabla\psi) = (\nabla\times\nabla\phi)\cdot\nabla\psi - (\nabla\times\nabla\psi)\cdot\nabla\phi = 0$$

Since $\nabla\cdot(\rho\vec{U}) = 0$ is in fact the continuity equation, the stream functions that satisfy Equation (66) will thus identically satisfy the continuity equation. The vector $\vec{U}$ is perpendicular to both vectors $\nabla\phi$ and $\nabla\psi$ and the vectors $\nabla\phi$ and $\nabla\psi$ are perpendicular to the surfaces ϕ = constant and ψ = constant, respectively. Hence the vector $\vec{U}$ lies in both the planes ϕ = constant and ψ = constant at the point in question. The consequence is that both the ϕ = constant and ψ = constant family of surfaces are <u>stream surfaces</u>, and their intersection is a <u>streamline</u>.

Application of Equation (66) to the shock layer region yields the following scalar equations

$$\phi_r\psi_\theta - \phi_\theta\psi_r = r\rho u \tag{67}$$

$$\phi_\theta\psi_x - \phi_x\psi_\theta = r\rho v \tag{68}$$

$$\phi_x\psi_r - \phi_r\psi_x = \rho w \tag{69}$$

where the subscripts r and θ denote partial differentiations, holding x constant. After transforming the coordinates x, r, and θ to X, r, and θ according to Equation (12), the above equations take the following forms:

$$\phi_r \psi_\theta - \phi_\theta \psi_r = \rho \left(r u - r v S_r - w S_\theta \right) \tag{70}$$

$$\phi_\theta \psi_X - \phi_X \psi_\theta = r \rho v \tag{71}$$

$$\phi_X \psi_r - \phi_r \psi_X = \rho w \tag{72}$$

Equations (71) and (72) can now be used to solve for ϕ_X and ψ_X. The result is

$$\phi_X = \frac{\rho \left(r v \phi_r + w \phi_\theta \right)}{\phi_\theta \psi_r - \phi_r \psi_\theta} \tag{73}$$

$$\psi_X = \frac{\rho \left(r v \psi_r + w \psi_\theta \right)}{\phi_\theta \psi_r - \phi_r \psi_\theta} \tag{74}$$

Since the velocities v and w have been transformed to $\bar{v}$ and $\bar{w}$ in the basic formulation, Equations (73) and (74) must also be rewritten in terms of $\bar{v}$ and $\bar{w}$. The results are

$$\phi_X = \frac{\rho \left[r \phi_r \left(\bar{v} \cos\theta + \bar{w} \sin\theta \right) + \phi_\theta \left(\bar{w} \cos\theta - \bar{v} \sin\theta \right) \right]}{\phi_\theta \psi_r - \phi_r \psi_\theta} \tag{75}$$

$$\psi_x = \frac{\rho\left[r\psi_r\left(\bar{v}\cos\theta + \bar{w}\sin\theta\right) + \psi_\theta\left(\bar{w}\cos\theta - \bar{v}\sin\theta\right)\right]}{\phi_\theta\,\psi_r - \phi_r\,\psi_\theta} \tag{76}$$

Since uniform conditions prevail in the free stream flow, an infinite number of choices of the initial values of ϕ and ψ can be selected. Note that the values of the stream functions are invariant in crossing the shock, and that the working equations, i.e., Equations (75) and (76), are independent of the initial conditions. A pair of stream functions which satisfy Equation (66) and behave well throughout the flow field are now defined in terms of the free stream oriented coordinates (x', y', z' in Figure 2) as follows:

$$\phi = \sqrt{\rho_\infty U_\infty}\; y' \tag{77}$$

$$\psi = \sqrt{\rho_\infty U_\infty}\; z' \tag{78}$$

Transforming Equations (77) and (78) into the body-oriented cylindrical coordinates and making use of Equation (10), we obtain the stream functions immediately behind the shock:

$$\phi_s = \sqrt{\rho_\infty U_\infty}\left\{S(r_s, \theta_s)\sin\alpha + r_s\cos\theta_s\cos\alpha\right\} \tag{79}$$

$$\psi_s = \sqrt{\rho_\infty U_\infty}\; r_s \sin\theta_s \tag{80}$$

The above equations are used to calculate ϕ_r, ϕ_θ, ψ_r, and ψ_θ behind the shock which in turn allows calculation of ϕ_x and ψ_x from Equations (75) and (76). The stream functions are then numerically integrated toward the body with the subsequent r and θ derivatives evaluated numerically at each constant X surface instead of using Equations (79) and (80). A record of the values of these stream functions will be kept in the entire shock layer so that the streamlines corresponding to each set of values of ϕ_s and ψ_s at the shock can be easily traced.

To determine the body, we note that the body is wetted by the stagnation streamline. Therefore, both stream functions at the body must be invariant and equal to the respective ones at the stagnation point. The stagnation point is defined, because of the flow symmetry about the pitch plane, by

$$\psi_{BODY} = \psi_{STAG} = 0 \tag{81}$$

$$\phi_{BODY} = \phi_{STAG} \tag{82}$$

Thus body locations other than in the pitch plane, where $\psi = 0$ at all points, are obtained by searching for points in the shock layer where $\psi = 0$. These points should also satisfy the relation $\phi = \phi_{STAG}$ and thus serve to determine the value of ϕ_{STAG}. The body location in the pitch plane may then be obtained by searching for points in the shock layer on the pitch plane where $\phi = \phi_{STAG}$. This point will be given more detailed consideration in a later section on the body determination procedure used in the computer program.

SHOCK SHAPE FORMULATION

The inherent instability of the integration of the elliptic type flow equation in the subsonic regime for an initial value (or Cauchy) problem has long been recognized. This is referred to as nonessential instability in Reference 4. It is precisely this phenomenon which requires the statistical smoothing of the data which is described in a later section. This instability becomes troublesome whenever an initial error is introduced into the calculations because the tendency is for this error to grow rapidly. It is thus mandatory to ensure the use of smooth inputs to the program. The easiest way of ensuring smooth initial conditions is to use an analytically fitted shock shape. Needless to say, all subsequent steps in the integration procedure should also be done accurately; and these considerations will be dealt with in the appropriate section of the report.

The equation which is used to represent the shock should be versatile so that a variety of surfaces can be represented. Since angle-of-attack effects are included, the shock shape in cylindrical coordinates will not have axial symmetry even for axially symmetric body shapes. Thus referring to Figure 2 the shock shape can be described either as,

$$S = S(r, \theta)$$

or

$$r = f(S, \theta)$$

Power series and Fourier series are very versatile functions. These two series can be combined into either a Fourier series having power series coefficients or vice versa (both equivalent), i.e.,

$$S = \sum_{g=0}^{\infty} \left(\sum_{n=1}^{\infty} a_{n,g}\, r^n \right) \cos g\theta = \sum_{n=1}^{\infty} \left(\sum_{g=0}^{\infty} a_{n,g} \cos g\theta \right) r^n \tag{83}$$

$$r = \sum_{g=0}^{\infty} \left(\sum_{n=1}^{\infty} a_{n,g}\, S^n \right) \cos g\theta = \sum_{n=1}^{\infty} \left(\sum_{g=0}^{\infty} a_{n,g} \cos g\theta \right) S^n \tag{84}$$

where all $(\sin g\theta)$ terms can be eliminated because of symmetry of the shock about the pitch plane. Upon examination of the derivatives, it is seen that Equation (84) can never yield a blunt body at the origin because the slope can never be infinite. Thus only the two forms of Equation (83) are of further interest. While these two forms are mathematically equivalent, there will be differences in manipulations when a finite number of coefficients are determined mathematically for the program input.

The only information found concerning angle-of-attack effects on the shock shape about blunt bodies was Kaattari's work, References 11, 12, and 13 where he determined that a correction (to the zero angle-of-attack shock) of the form

$$\left(a_1 r + a_2 r^3 \right) \cos \theta$$

proved very satisfactory. Using this information, it would seem that the form

$$S = \sum_{g=0}^{\infty} \left(\sum_{n=1}^{\infty} a_{n,g}\, r^n \right) \cos g\theta$$

would give the Kaattari terms most explicitly. Also, this form allows the pitch plane shock, about which the most information would be available, to be fitted more accurately than the other form which would stress the θ variation.

It has already been stated that it is desired that the function be completely analytic, and it is at this point that the implications of using a body-oriented cylindrical coordinate system must be examined. The main problem is concerned with continuity of the various r derivatives across

the origin $r = 0$. For purposes of analysis, consider a Cartesian system lying in a plane inclined at an angle θ_1 and passing through the x - axis as shown in Figure 5.

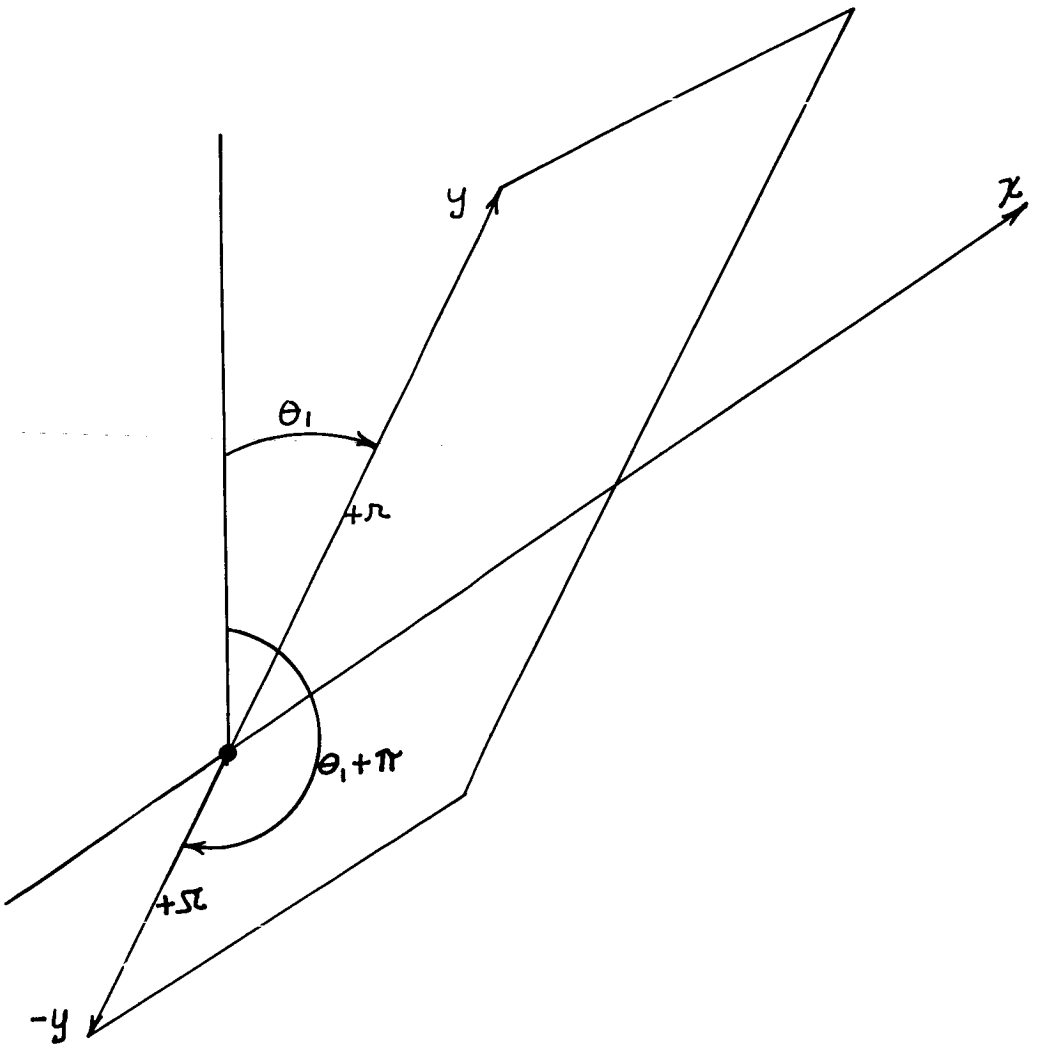

Figure 5. Transformed Cartesian Coordinate System

By transforming the series expression to a form using the variable y we obtain two expressions which may be compared for continuity in the r direction. For $\theta = \theta_1$, $y = r$ while for $\theta = \theta_1 + \pi$, $y = -r$.

Since

$$\cos g(\pi+\theta_1) = \cos g\pi \cos g\theta_1 = (-1)^g \cos g\theta_1 ,$$

we obtain

$$\theta = \theta_1 , \qquad S = \sum_{g=0}^{\infty}\left(\sum_{n=1}^{\infty} a_{n,g}\, y^n\right)\cos g\theta$$

$$\theta = \pi+\theta_1 , \qquad S = \sum_{g=0}^{\infty}\left(\sum_{n=1}^{\infty} a_{n,g}(-1)^n y^n\right)(-1)^g \cos g\theta$$

Or, for $\theta = \pi+\theta_1$

$$S = \sum_{g=0}^{\infty}\left(\sum_{n=1}^{\infty} a_{n,g}\,(-1)^{n+g} y^n\right)\cos g\theta$$

Since both expressions must be identical in this coordinate system, it follows that

$$(-1)^{n+g} = 1$$

This requirement may be also stated as,

$$n+g = 2N$$

where N is any integer from 0 to ∞ .

Thus if g is odd, only the odd powers of n may be present; and if g is even, only the even powers of n may be present. The partials with respect to θ are always continuous at the origin because r goes to zero. Therefore, the final series is of the form

$$\begin{aligned} S = {} & (a_{2,0}\, r^2 + a_{4,0}\, r^4 + a_{6,0}\, r^6 + \text{-----}) \\ & + (a_{1,1}\, r + a_{3,1}\, r^3 + a_{5,1}\, r^5 + \text{------})\cos\theta \\ & + (a_{2,2}\, r^2 + a_{4,2}\, r^4 + \text{--------})\cos 2\theta \end{aligned}$$

or

$$S = \sum_{p=0}^{\infty} \left(\sum_{n=1}^{\infty} a_{2n,2p} \; r^{2n} \right) \cos 2p\theta \tag{85}$$
$$+ \sum_{m=1}^{\infty} \left(\sum_{n=1}^{\infty} a_{2n-1,2m-1} \, r^{2n-1} \right) \cos\left((2m-1)\theta\right)$$

It is to be noted that the Kaattari terms remain.

Equation (85) gives smooth, analytic, non-pointed surfaces; but it is limited in the fact that for each value of r there is only one value of S or, i.e., the curve can never be double valued in S. In such cases as the Apollo capsule types, it may well be desirable to fit a shock shape with a negative first derivative, $\partial r / \partial S$. To allow for such a possibility, the first symmetric terms $(p=0)$

$$a_{2,0} \, r^2 + a_{4,0} \, r^4 + a_{6,0} \, r^6 + \cdots$$

can be replaced by S_0, where S_0 is defined by

$$r^2 = a_{1,0} S_0 + a_{2,0} S_0^2 + a_{3,0} S_0^3 + \cdots + a_{10,0} S_0^{10} \tag{86}$$

and the Equation (85) becomes

$$S = S_0 + \sum_{p=1}^{\infty} \left(\sum_{n=1}^{\infty} a_{2n,2p} \; r^{2n} \right) \cos 2p\theta \tag{87}$$
$$+ \sum_{m=1}^{\infty} \left(\sum_{n=1}^{\infty} a_{2n-1,2m-1} \; r^{2n-1} \right) \cos\left((2m-1)\theta\right)$$

where $$r^2 = \sum_{n=1}^{\infty} a_{n,0} \, S_0^n$$

The computer program will accept the shock fit given by Equation (83) with terms included through $q = 2$ and $n = 20$ with or without the $q = 0$ term replaced by Equation (86) . The program user should, in general, follow the restrictions just derived for the allowable terms, and the remainder of this report will be based on the observation of these restrictions. The user may, however, wish to add one or more of the non-allowable terms for the purpose of convenience in hand alteration of the shock fit. This may be justified by the fact that the program uses a finite difference technique with a five point fit for determining the lateral derivatives (in which the discontinuity would appear). By restricting the use of non-allowable terms to the higher order terms in Ω , the discontinuity at the origin may be effectively smoothed out.

ITERATIVE CONVERGENCE TECHNIQUE

The iterative convergence technique as applied to the inverse method consists of linearly relating changes in the predicted body coordinates to changes in the coefficients used in the shock fit. The justification and use of this linear influence technique as applied to the blunt body problem is presented below.

Given a function of the form

$$S = F(a_1, a_2, a_3, a_4, ---)$$

where S is the dependent variable, a_1 , a_2, a_3---- all represent independent variables, and

$$\epsilon_1 = f_1(a_1, a_2, a_3 ----)$$

$$\epsilon_2 = f_2(a_1, a_2, a_3 ----)$$

$$\epsilon_3 = f_3(a_1, a_2, a_3 ----)$$

$$- -$$

where ϵ_1, ϵ_2 ....represent dependent variables which are functions of the same independent variables. Then if the number of a_j's and ϵ_i's are equal, it can be said

$$S = G(\epsilon_1, \epsilon_2, \epsilon_3 ----)$$

However, if the ϵ_i's and a_j's are related implicitly, $G(\epsilon_1, \epsilon_2, \epsilon_3 --)$ cannot be solved for analytically, and other methods must be resorted to.

For the present purposes, the function $F(a_1, a_2, a_3 ----)$ represents the equation of the shock wave

$$S = (a_1 r^2 + a_2 r^4 + \cdots\cdots + a_n r^{2n}) + (a_{n+1} r + a_{n+2} r^3 \ldots) \cos\theta + (\cdots\cdots) \cos 2\theta$$

or

$$S = S_0 + (a_{n+1} r + a_{n+2} r^3 \ldots\ldots) \cos\theta + (\cdots\cdots) \cos 2\theta$$

where

$$r^2 = a_1 S_0 + a_2 S_0^2 + a_3 S_0^3 \cdots\cdots$$

and ϵ_1, ϵ_2, ϵ_3, etc., are measures of the error between the desired body and the body obtained by using the input shock equation. The number of ϵ_i's is equal to the number of a_j's which actually are the constant coefficients in the shock wave equation but are considered as variables because they are to be varied so that the desired body is obtained from the input shock equation.

From the Taylor series expansion, changes in ϵ_i are related to changes in the 'variable' a_j by

$$\delta\epsilon_i = \sum_{n=1}^{\infty} \frac{1}{n!} \left(\sum_{j=1}^{p} \left(\frac{\partial}{\partial a_j} \delta a_j \right) \right)^n \epsilon_i$$

$$\delta\epsilon_i = \sum_{n=1}^{\infty} \frac{1}{n!} \left(\frac{\partial}{\partial a_1} \delta a_1 + \frac{\partial}{\partial a_2} \delta a_2 + \frac{\partial}{\partial a_3} \delta a_3 \cdots\cdots + \frac{\partial}{\partial a_p} \delta a_p \right)^n \epsilon_i$$

$$i = 1, p$$

where $\left(\frac{\partial}{\partial a_1} \delta a_1 + \frac{\partial}{\partial a_2} \delta a_2 \cdots\cdots \right)$ is an operator on ϵ_i. It is seen that as δa_j approaches $d a_j$, the higher order terms consisting of $n \geq 2$ will approach zero; and so for vanishingly small δa_j

$$\delta\epsilon_i = \left(\frac{\partial \epsilon_i}{\partial a_1} \delta a_1 + \frac{\partial \epsilon_i}{\partial a_2} \delta a_2 + \frac{\partial \epsilon_i}{\partial a_3} \delta a_3 \cdots\cdots \frac{\partial \epsilon_i}{\partial a_p} \delta a_p \right) \qquad (88)$$

$$i = 1, p$$

If p such simultaneous equations are derived with the ϵ_i's representing the initial errors between the desired body and the body obtained from the initial shock input, and if $\partial\epsilon_i/\partial a_j$ can be found, then the δa_j's can be found by requiring $\delta\epsilon_i = -\epsilon_i$. These δa_j's are the required changes in the shock shape coefficients to reduce all errors to zero. It is to be remembered that this is only true if the shock coefficient corrections are small enough for a linearized approach to be valid.

The partial derivatives, by definition, are the ratio of the differential change in ϵ_i to a differential change in a_j, keeping all the other a_j's constant. They are approximated as follows. The a_1 coefficient of the shock is perturbed an amount Δa_1 so that the new $a_1 = a_1 + \Delta a_1$. Now the program is run and a body obtained from this perturbed shock equation. The new errors, $\epsilon_i = \epsilon_i + \Delta\epsilon_i$, are now compared to the original errors, ϵ_i, and the perturbations in the errors are obtained from

$$(\epsilon_i + \Delta\epsilon_i) - \epsilon_i = \Delta\epsilon_i$$

similarly

$$(a_1 + \Delta a_1) - a_1 = \Delta a_1$$

and $\dfrac{\partial\epsilon_i}{\partial a_1} \approx \dfrac{\Delta\epsilon_i}{\Delta a_1}$ $\quad i = 1, p$ can then be formed.

By similarly perturbing $a_2, a_3 \cdots a_p$ all the partial derivatives can then be formed and p simultaneous equations written. The resulting p equations in p unknowns, $\delta a_1, \delta a_2, \cdots, \delta a_p$, are linear and algebraic. Thus they can be solved and the resulting solutions be used to correct the shock coefficients for the new input.

The corrected shock equation coefficients are

$$\begin{aligned} a_{1e} &= a_1 + \delta a_1 \\ a_{2e} &= a_2 + \delta a_2 \\ &\vdots \\ a_{pe} &= a_p + \delta a_p \end{aligned}$$

and the procedure repeats itself until the ϵ_i's are all below acceptable values.

INSTABILITIES AND DATA SMOOTHING

The solution of the flow field behind a prescribed shock amounts mathematically to solving an initial value or Cauchy-type problem. The difficulties which arise in this solution have been widely discussed (e.g., References 4,

and 14). The discussion in Reference 4 gives an excellent treatment of this topic and presents the results and conclusions of a thorough study of the various instabilities that are of interest in the development of a finite difference solution of the inverse method. In Reference 4, Lomax and Inouye identify two classes of instability--inherent instability and induced instability.

Induced instability is caused by the specific behavior of a particular numerical procedure as applied to a given type of equation. This instability has been experienced with the computer program in running the Apollo body at angle-of-attack and occurred in the pitch plane on the outer radii grid points on the windward side of the flow field. The instability can be eliminated by an appropriate reduction of integration step size but is unfavorably affected by using a closer radial grid spacing.

Examination of Equations (18) and (19) through (22) shows that two removable singularities also exist in the flow. The denominator of Equation (18) may be shown to be zero when the characteristic line becomes parallel to the marching plane. For the perfect gas case, for example, if the denominator is set equal to zero, one obtains

$$\left(\frac{Q}{r}\right)^2\left(h_p-\frac{1}{\rho}\right)+h_\rho\left[1+S_r^2+\left(\frac{S_\theta}{r}\right)^2\right]=0$$

From Equation (24)

$$h_p-\frac{1}{\rho}=\frac{\gamma}{\gamma-1}\frac{1}{\rho}-\frac{1}{\rho}=\frac{1}{\gamma-1}\frac{1}{\rho}$$

And from Equation (25)

$$h_\rho=-\frac{\gamma}{\gamma-1}\frac{p}{\rho^2}$$

Or

$$\frac{h_\rho}{h_p-\frac{1}{\rho}}=-\frac{\gamma p}{\rho}=-a^2$$

Thus

$$\frac{\left(\frac{Q}{r}\right)^2}{1+S_r^2+\left(\frac{S_\theta}{r}\right)^2}=a^2 \tag{89}$$

The velocity component normal to the marching plane is the scalar product of the velocity vector and a unit vector normal to the plane. Using Equation (42),

$$U_n = \vec{U}\cdot\vec{n} = \left(u\vec{i}_x + v\vec{i}_r + w\vec{i}_\theta\right)\cdot\left(\vec{i}_x - \vec{i}_r S_r - \vec{i}_\theta \frac{S_\theta}{r}\right) \Big/ \left(1 + S_r^2 + \left(\frac{S_\theta}{r}\right)^2\right)^{1/2}$$

$$U_n = \frac{u - v S_r - \frac{w S_\theta}{r}}{\left(1 + S_r^2 + \left(\frac{S_\theta}{r}\right)^2\right)^{1/2}} = \frac{\frac{Q}{r}}{\left(1 + S_r^2 + \left(\frac{S_\theta}{r}\right)^2\right)^{1/2}} \tag{90}$$

So that

$$U_n = a$$

To avoid encountering this condition, which experience has shown is only found in the high supersonic regions of the flow field, a test of normal Mach number is made. If

$$M_n > M_{n_{TEST}},$$

the integration of that grid point is terminated.

The second removable singularity occurs when $Q = 0$, which is the condition for zero velocity normal to the marching plane. This may be verified from Equation (90) above. Since this condition occurs in a limited region very near the body surface, the approach has been adopted in which the integration of that grid point is terminated when the value of

$$\left(\frac{Q}{Q_{SHOCK}}\right)_{i,j} < Q_{TEST} .$$

The body location and properties are then obtained from the extrapolation technique used in the body determination procedure.

Inherent instabilities are stated in Reference 4 to arise from either of two sources: (1) due to singularities (2) due to ill conditioning. The presence of singularities in the flow field is obviously unrealistic and implies that an unacceptable shock shape has been used. Special cases where the desired body is non-analytic (e.g., the discontinuous curvature on Gemini, Apollo, etc.) result in singularities occurring on the body surface. For these cases, the problem is handled by limiting the integration to the region outside of the body.

The instability due to ill conditioning is nonessential and would not occur in an analytic solution of the flow behind a given analytic shock. It arises from the inherently unstable solution of the differential equations starting from any initial inaccuracy. In numerical solutions, these inaccuracies result from round-off, truncation errors in integration, and curve fit errors in computing derivatives. Considerable discussion exists in the literature on this problem as it exists in the subsonic region of the flow. Lomax and Inouye reported that they used smoothing to control the error buildup. No such problem was encountered with the S&ID program at zero angle-of-attack, since the radial grid point spacing was much larger than that used by Lomax and Inouye. The closeness of grid points in the θ -direction near the body axis is not a problem, since properties have axial symmetry. The procedures followed by the S&ID computer program do not treat the zero angle-of-attack case differently from a general case. These data are separately computed at all grid points, and axial symmetry of flow property values for the zero angle-of-attack case results entirely from the axial symmetry of the shock and not from special treatment. The result, however, is that despite this general treatment, the flow property values do have exact axial symmetry (even though they may have errors due to round-off, truncation, etc.). This is true even for the reformulation in terms of $\bar{v}$ and $\bar{w}$ since examination of the x -derivative equations reveals that the θ -derivatives of all flow properties are multiplied by w (which is zero for this case). Thus perfect smoothness of the data in the θ -direction is evident in the results. An instability was found to develop near the x -axis for non-zero angle-of-attack cases without smoothing. Its origin can be traced to the choice of coordinate system through the following arguments.

When the angle-of-attack is not zero, the axial symmetry of property values is not present. The round-off and truncation, etc., errors are now not identical for all grid points at r = constant, and the perfect smoothness of the data is lost. Now in itself this lack of smoothness would be no worse than a similar lack of smoothness that is always present in the r -direction and which caused no trouble for zero angle-of-attack. The cause of the severe instability which was found is due to the cylindrical coordinate system. The choice of a cylindrical coordinate system inherently results in a closer spacing of grid points near the x -axis as shown in Figure 6 .

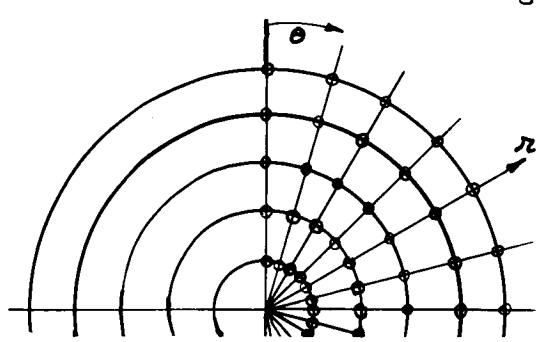

Figure 6. Grid Point Locations in Cylindrical Coordinate System

In examination of Equations (5) and (6), for example, it is observed that all θ-derivatives are weighted by the factor $1/r$. Thus for the same degree of random inaccuracy in property values the θ-derivatives of these properties exhibit a noise component which increases as $1/r$. This becomes disastrous for small enough values of r. The simplest cure for this problem would be to eliminate progressively more grid points on the inner radii. As the axis is approached the properties approach the constant values at the axis, and only one point is required to carry all necessary information. The presence of other points and inaccurate values adds nothing to the information but adds progressively increasing noise as the axis is approached. This entire problem is adversely affected by the original choice of v and w as the lateral velocity components. These velocities do not approach constant values as the axis is approached but approach functions of θ.

In practice the dropping of grid points as just suggested is not practical. r-derivatives are required for outer radii grid points and the calculation of these derivatives uses property values on the inner radii. Carrying the logic two steps further it is seen that inner grid points could be dropped if the necessary intermediate point values were obtained by interpolation. But the operation of interpolation is basically inaccurate so that the application of statistical smoothing comes to mind as a means of increasing smoothness while basically retaining the information in the data. This is the approach used to control the instabilities in the calculations. Coupled with smoothing the velocities v and w were transformed to the velocities $\bar{v}$ and $\bar{w}$ as described in Equations (27) and (28) and shown in Figure 3. The advantages of using the new variables is that: 1) their approach to constant values as $r \rightarrow 0$ effectively furnishes another point at the origin in the data grid, thus aiding in the smoothing as actually programmed; and 2) by effectively replacing the lowest frequency term in a Fourier series expression for the velocities at $r = 0$ by a constant term, the filtering technique (smoothing) is much less critical and more easily done with a simple approach.

The flow field computer program is written in double precision to reduce round-off errors to a minimum. Although it was not expected that this feature would eliminate the need for smoothing, it was expected that the number of smoothings could possibly be reduced and that smoothing could possibly be started at a point farther downstream of the shock, thus promoting increased accuracy of the final program results.

The properties to be smoothed may be represented by a two-dimensional set of data points, $p_{i,j}$, where the subscripts on the property p are related to r and θ respectively, as defined in the Operating Manual, Reference 10. Although consideration was initially given to smoothing by fitting a least square surface to a subset of these points, from which an interior point could be corrected or smoothed, the simpler procedure of smoothing alternately in the orthogonal r and θ directions was adopted. As will be noted later, the program will allow the user to apply arbitrary weighting factors, dependent only on the r coordinate, in applying the correction indicated by the smoothing procedure.

The actual filtering technique adopted is a modification of that used by Lomax and Inouye, Reference 4. The method is to move the central point

in a group of five to the curve defined by a least square parabolic fit to these same data points. Since the S&ID program uses variable point spacing the least square fit calculation is complicated somewhat but is still straightforward.

Smoothing is applied alternately, first in the radial direction and then in a circumferential direction, and can be justified by the following considerations, In smoothing, the data should preferably be weighted in such a manner that values in which there is a high confidence level are smoothed the least, whereas values in which the confidence level is low are smoothed or corrected the most. In our case calculated values on the inner radii have the lowest level of accuracy and should be given the least weight in smoothing. By smoothing alternately in the r and θ directions, the data points can be weighted somewhat by using a particular sequence. In smoothing data in the r direction first (that is, on a line $\theta =$ constant) most of the data points will be accurate and hence the data will be smooth. The plot of some property on a line $\theta = \theta_1$ is shown in Figure 7 .

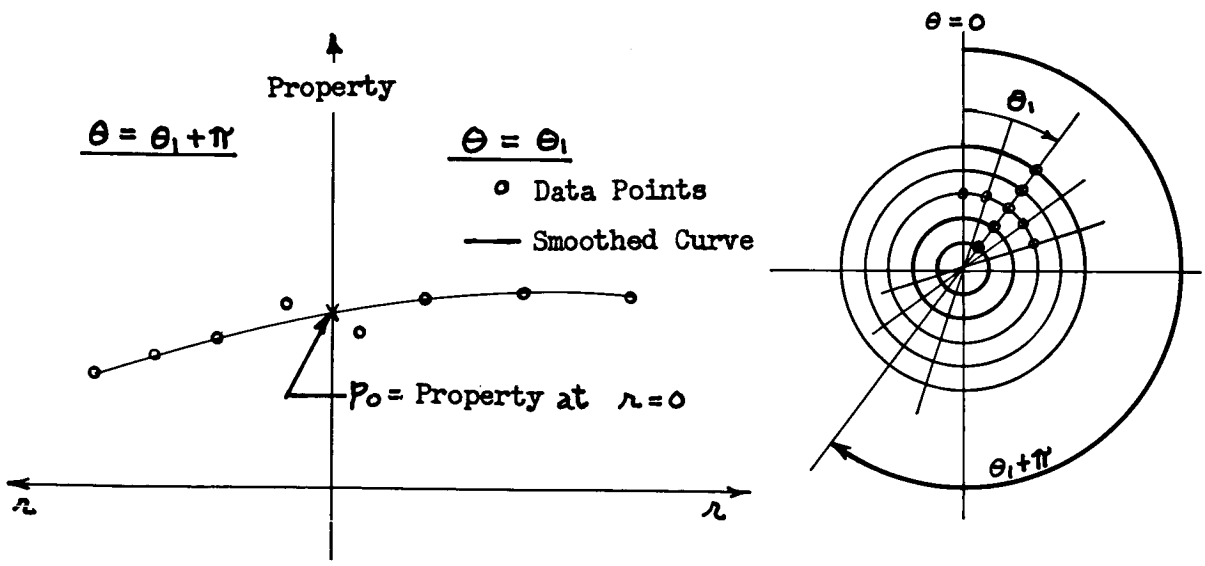

Figure 7 . Typical Property Variation in the Radial Direction

The value of a property at $r = 0$, called p_0 , being independent of θ , aids in the smoothing operations since all smoothed curves must have a common value at $r = 0$. Thus the smoothed curve is tied down by a constraint at the origin and by the existence of mostly smooth data.

By using the particular sequence stated above, neighboring data points to the origin on the line $\theta =$ constant are more heavily weighted (since they are considered first) than neighboring data points on the curve $r =$ constant (since they are used second-only after being smoothed). This is consistent

with the weighting considerations just presented since most data values on a line θ = constant are accurate - only the points near the axis will be inaccurate.

THERMODYNAMIC PROPERTIES

The program has been formulated with the provision for running both the perfect gas case (i.e., constant specific heats) and a real gas, equilibrium air case. The thermodynamic state properties for the real air are based principally on the Hilsenrath and Beckett tabulated data for argon-free air presented in Reference 15 supplemented by information from References 16, 17, and 18.

The subprogram used to compute the real gas thermodynamic properties is based on empirically-fitted equations to the Hilsenrath and Beckett data and for the most part is capable of reproducing the tabulated data to within one percent. A sample, for instance, of the reproducibility of enthalpy is shown in the table below:

Table 1 . Comparison of Thermodynamic Properties of Real Air, $\log_{10}(\rho/\rho_0) = -2$

Temperature (Degrees K)	$H_{Program}$ (BTU/lb_m)	$H_{H\&B}$ (BTU/lb_m)	Percent Error
2000	987.3	984.3	0.305
3000	2166.8	2157.3	0.440
4000	4278.0	4251.4	0.625
5000	5858.7	5820.4	0.658
6000	10792.0	10712.8	0.739
7000	22480.4	22279.2	0.903
7500	28568.3	28277.8	1.027
8000	32935.4	32576.8	1.102
8500	35876.4	35468.3	1.150
9000	38157.6	37722.8	1.150

The empirical equations are developed in Reference 19 as dimensionless parameters of the form $H/\mathfrak{z}RT$, $\mathfrak{z}$, and s/R, each of which is given as a function of pressure and density. The program is capable of operating over a density range of 10^{-6} to 10^{2} relative atmospheres and up to a temperature of 15,000 K. A relative atmosphere is defined as ρ/ρ_0 where ρ_0 is the density at standard conditions of temperature and pressure. The terms in the empirical equations consist of eighth-degree polynomial expressions joined by transition functions stemming from Bose-Einstein and Fermi-Dirac quantum statistics as applied to molecular dissociation processes. These two transition functions are of the following form:

Fermi-Dirac Function

$$\frac{1}{1 + \exp(kx)}$$

Bose-Einstein Function

$$\frac{1}{1 - \exp(kx)}$$

The thermodynamic properties procedure for real air is formulated as a subroutine in the program and can easily be exchanged for other gas medias if so desired. However, this would require the formulation of a new set of equations empirically-fitted to the new gas media.

COMPUTER PROGRAM DEVELOPMENT

GENERAL DESCRIPTION

The Blunt Body Computer Program produces the inviscid, subsonic-transonic shock layer flow field for a convex, axisymmetric body shape at angle-of-attack. An estimated shock shape and specified requirements for altering this shock shape along with free-stream flow conditions and certain control information are entered as input information to the program. The program then uses this information to generate the flow field and a perturbed shock shape. This process is repeated automatically until each coefficient in the shock equation has, in turn, been perturbed. The body shape perturbations resulting from each flow field calculation and the incremental changes in the shock coefficients are then employed in a linear influence coefficient matrix solution to find a final correct shock shape. This final shock shape is then used to generate a final flow field. A second program, following this basic flow field computation program, uses the final flow field data to generate additional flow field parameters and to output data according to pre-specified plans or options designed specifically to aid in the study of reentry flow field and heating analyses.

The program has been designed with the capability for handling a perfect gas media (specified constant γ) or a real gas air media. An increased run time is associated with the real gas case due to the iterative procedure required in the evaluation of certain thermodynamic functions. The program has been formulated such that other atmospheric medias can readily be incorporated provided suitable empirically-fitted expressions, similar to those used for the air media, can be formulated for the thermodynamic properties.

The basic formulation of the program is based on a body oriented cylindrical coordinate system wherein grid points on the marching planes are defined by a radial distance, r, measured from the body axis of symmetry and an angular distance, θ, measured from the pitch plane. A marching plane is a computing plane in the program which is parallel (i.e., everywhere equidistant in the X-direction) to the shock surface. These planes form the basis for the X-integration of the flow properties in that one starts at the shock surface and works downstream until the body surface is defined. Figure 8 shows a typical grid point pattern on a marching plane together with the i, j subscripting notation used to identify grid points in the program. The pattern is viewed from the shock looking downstream along the body axis of symmetry.

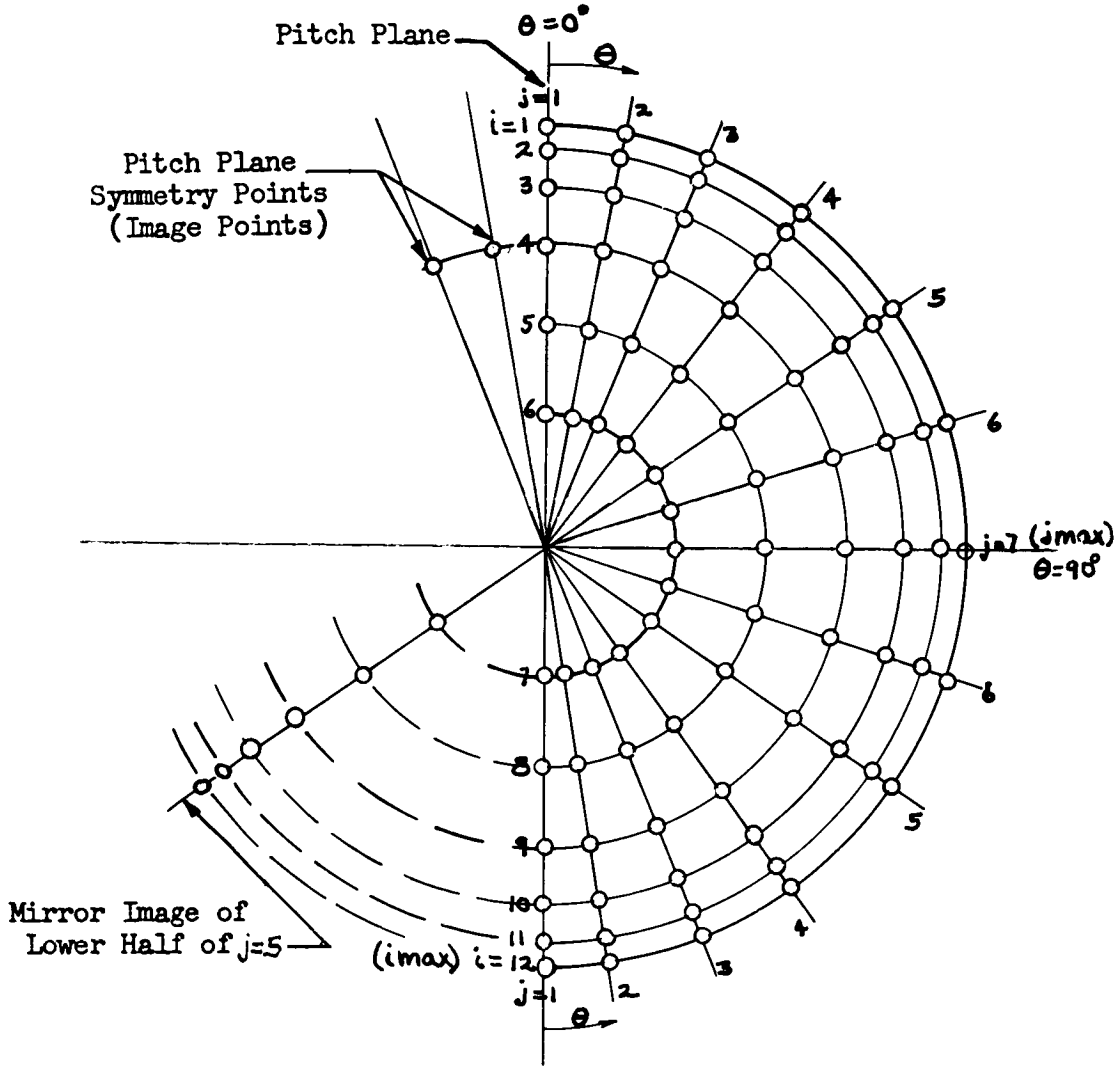

Figure 8. Orientation of Grid Points in Marching Plane

Only the flow field to the right of the pitch plane is considered because of the flow symmetry existing about the pitch plane. Advantage is taken of this symmetry in the evaluation of θ-derivatives for points on $j = 1$ and 2 by artificially using mirror-image points to the left of the pitch plane. It is also to be noted that symmetry exists between the lower half of each j plane and its image plane with respect to the origin making it possible to consider points and properties along the mirror-image of the lower half of a j plane in the evaluation of lateral derivatives and the smoothing of data in the r-direction.

It is not necessary to use the entire network of grid points shown in the illustration. Provision for eliminating a portion of the grid network has been incorporated in the program. This is a highly desirable feature when computing flow fields for bodies at large angle-of-attack where the outer extremities of the flow field on the leeward side of the body are highly supersonic and instabilities commonly arise due to an alignment of the local characteristic line with the marching plane. This feature eliminates this undesirable region and limits the calculations to the desired subsonic-transonic flow region.

The entire program consists of two basic parts: Part (1) - A program for computing a flow field based on a given shock including a systematic means of iterating on the shock shape; Part (2) - A program for calculating additional flow field parameters and the output of data according to pre-specified options. The basic flow field computation program is subdivided into five parts linked to a main program. Such an elaborate procedure is required because of the lack of adequate machine-storage space introduced by the three-dimensional requirements of the problem to be solved. The first link (Link 5) called by the main program reads in the input data and sets up certain arrays of information in storage in the program. The second link called (Link 4) establishes the shock shape, forms certain geometrical lateral derivatives of the shock surface, and solves for the properties at each grid point immediately behind the shock. Link 1 contains the marching procedure which integrates plane by plane from the shock to the body. This link also contains the body determination procedure. Link 2 provides the routines for smoothing property data on the marching planes as the flow field is developed. The last link called in the flow field program, Link 3, pertains to the procedure for perturbing systematically the shock shape and solving the influence coefficient matrix for a more correct shock shape. A final flow field is then obtained for this more correct shock and stored on tape for use in the Data Output Program (Part 2 of the over-all program).

The Data Output Program performs certain basic functions in addition to the options specified as input to the program. Included in these mandatory functions are traces of the stagnation streamline and all other specified streamlines in the pitch plane. Body streamline traces emanating from the stagnation point are also furnished. These body streamlines are actually shown as projected traces on a planar surface normal to the body axis of symmetry. Properties at specified stations along the body surface are always obtained with the data output program. These stations lie along lines formed by the intersection of a θ = constant plane and the body surface and

emanate from the point of intersection formed by the axis of symmetry and the body surface.

In addition to these basic forms of data output, one can call for certain specified data output options. The first, known as Option B, presents flow properties (i.e., pressure, density, temperature, enthalpy, entropy, velocity, and Mach number) at specified intervals along any or all of the specified streamline traces. The other two options, A and C, are somewhat related in that Option A is a degenerate case of Option C. If Option A is specified, properties are obtained along the normal at a body station. Option C produces a complete description of the flow field properties using a cylindrical coordinate system based on the normal at a body station.

The Data Output Program consists of a main program and four links. Link 1 deals with the output requirements of Option B. Links 2, 3 and 4 apply to Options A and C. Link 2 provides the procedure for transforming local cylindrical coordinates based on the local body normal to the cylindrical coordinate system used in the Flow Field Program. Link 3 determines bounding grid coordinates for both the flow field and body stations. Link 4 reads from tape and strips-off the flow field properties at the bounding points and interpolates between them.

NUMERICAL PROCEDURES

Lateral Derivatives

In the process of marching from the shock to the body it is necessary to first evaluate property derivatives in the lateral plane (i.e., marching plane) before obtaining property derivatives in the marching direction. These lateral derivatives are usually determined by the application of finite difference principles to a set of specific points in the lateral plane. A typical network of points is shown in Figures 8 and 10.

In general, finite difference schemes are applied to a network of evenly spaced points in which the geometrical aspects of the method are vastly simplified by the uniform point spacing. In many problems, such as the blunt body flow field problem, it is impractical to use a uniform point spacing because of the complexities of the body shape and associated flow field. This becomes obvious when one considers current reentry bodies of the capsule-type which consist of a large face radius followed by a small shoulder radius. The most desirable point spacing in the radial direction for such a case, based on the body axis as the origin, consists of a coarse spacing over the face radius and a fine spacing in the shoulder region. This is not only true from the standpoint of economy in program operational time but is necessary for good accuracy. A close point spacing is required in the shoulder region where properties are changing rapidly. However, this same close point spacing over the face of the body would probably introduce noise in the data due to an insufficient change in properties between adjacent points. A non-uniform point spacing also proves beneficial in the angular direction for angle-of-attack cases where it is desirable to obtain

more detail and accuracy in the vicinity of the stagnation point. It should not be misconstrued that this procedure will handle only cases of unequally spaced grid points. The procedure is general and will readily handle the simpler case of equal point spacing.

Another desirable feature that is incorporated into the lateral derivative procedure in the program is the ability to limit the lateral extent of the flow field to an arbitrary region of the entire grid point matrix by working strictly within a cutoff flow field boundary, Figure 10. The program begins with the complete matrix of points at the shock, but immediately reverts to the cutoff boundary once the march to the body has been initiated. This cutoff boundary is for the most part tailored to the specific problem being solved and attempts to limit the solution to the subsonic and transonic regions of the flow field. Supersonic flow can be obtained with the program provided there is no alignment of the local characteristic line with the marching plane. Flow singularities of a removable nature will occur in such cases.

The basic formulation of the lateral derivative procedure employs a five-point central difference fit to the grid points. In the last section mention was made of the various flow field symmetries obtained with the form of the cylindrical grid system employed in the program. This is particularly true in the angular direction about the pitch plane making it possible to use a five-point central difference scheme to compute lateral derivatives for all points in the angular (theta) direction. On the other hand, the radial direction contains no such condition at the outer edges of the flow field, and it is necessary to employ five point off-side finite difference formulae for the outer two radii. In the original lateral derivative formulation no attempt was made to eliminate grid points that fell inside of the predicted body shape. This approach was changed when it was found that the properties at these grid points could become completely unreliable due to their proximity to singular regions in the flow field. These singularities may be essential or may be of a removable type associated with the particular coordinate system employed in the program. The decision was made to drop the forward integration for such points, prior to reaching the body, and to obtain the body location and properties for this grid point by extrapolation. This step cured the problem of inaccuracies in the data but necessitated a reformulation of the lateral derivative procedure to include off-side or end point finite difference schemes for grid points in the central region of the marching plane. At the same time it was realized that a cutoff flow field would be highly desirable from the standpoint of eliminating singular point instabilities occurring in the supersonic region. The use of a cutoff flow field introduced a further need for a finite difference scheme with off-side or end-point provisions. Thus, a three-point finite difference scheme with end-point provisions was incorporated in the lateral derivative procedure. A three-point fit was considered for two reasons. First, storage space in the program was limited because of the need for carrying large arrays of double precision numbers. Second, the three-point fit provided greater flexibility once the body was encountered and grid points were dropped. The only disadvantage of the three-point fit is its poorer accuracy in comparison with a five-point

off-side formula. However, it was reasoned that the end-of-array points, where the marching plane intersected the body, were being dropped continually as the integration proceeded and the propagation of errors into the remaining grid points would be somewhat self-limiting.

To summarize, a five-point central difference formula is used when possible. Otherwise a three-point central difference or end-point formula is used except at the outer radial edge of the cut-off grid where five-point off-side or end-point formulas are used to determine $\mathcal{R}$-derivatives on the outer two grid points.

A short summary of the three-point and five-point lateral derivative formulas is presented below along with appropriate illustrations, Figure 9 , of the symbols used. Considering the five-point fit, a fourth degree polynomial,

$$y = a + bx + cx^2 + dx^3 + ex^4 \quad , \tag{91}$$

is passed through the five points with the center point as the origin. Rewriting this polynomial for each point in terms of the local coordinate system and eliminating the translation distance, a , one obtains the following expressions:

$$y_{(-2)} \equiv S' = bF + cF^2 + dF^3 + eF^4 \tag{92}$$

$$y_{(-1)} \equiv R' = bG + cG^2 + dG^3 + eG^4 \tag{93}$$

$$y_{(0)} = a = 0 \tag{94}$$

$$y_{(+1)} \equiv T' = bB + cB^2 + dB^3 + eB^4 \tag{95}$$

$$y_{(+2)} \equiv U' = bE + cE^2 + dE^3 + eE^4 \tag{96}$$

The solution of these equations to obtain expressions for the coefficients , b, c , d and e in terms of the property parameters S', R', T' and U' and the relative distances F, G, B and E can be obtained by a matrix solution. The denominator is strictly a function of the local distances and once a grid pattern has been chosen remains the same for each marching plane. The job of forming lateral derivatives is further simplified by noting that the radial point spacing is the same for each j plane and the angular point spacing is the same for each i line. The resulting expression for the denominator in the expressions for the polynomial coefficients are as follows:

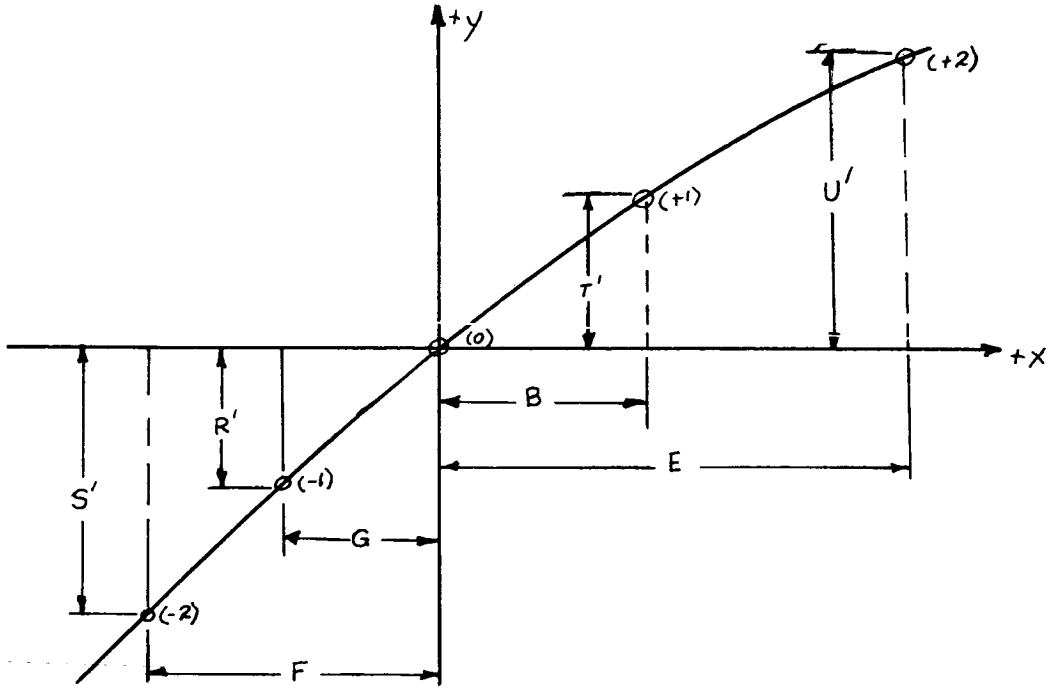

a. Five-Point Fit

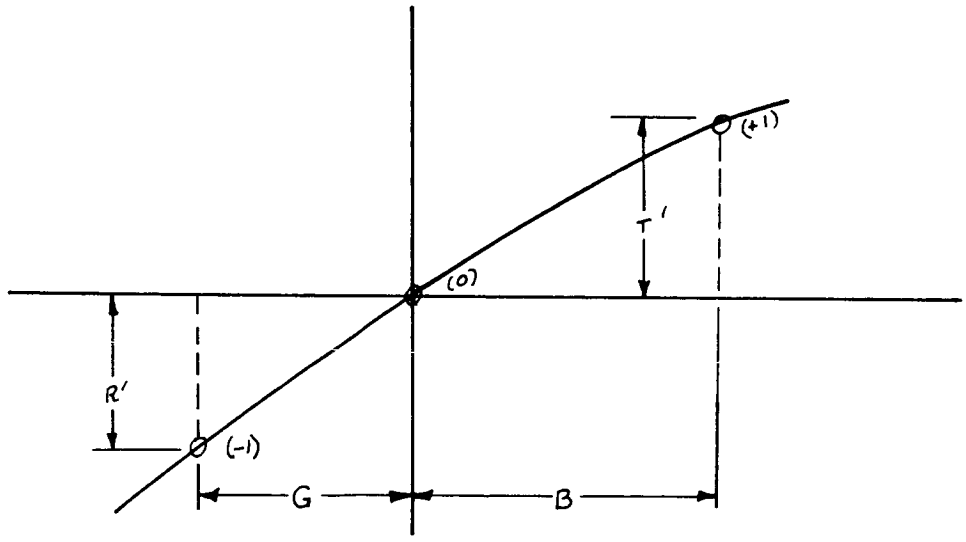

b. Three-Point Fit

Figure 9. Description of Three-Point and Five-Point Finite Difference Fit

$$
\begin{aligned}
DEN = {} & F\left[B^3E^4G^2 + B^4E^2G^3 + B^2E^3G^4 - B^3E^2G^4 - B^2E^4G^3 - B^4E^3G^2\right] \\
& -G\left[B^3E^4F^2 + B^4E^2F^3 + B^2E^3F^4 - B^3E^2F^4 - B^2E^4F^3 - B^4E^3F^2\right] \\
& +B\left[E^4F^2G^3 + E^3F^4G^2 + E^2F^3G^4 - E^2F^4G^3 - E^3F^2G^4 - E^4F^3G^2\right] \\
& -E\left[B^4F^2G^3 + B^3F^4G^2 + B^2F^3G^4 - B^2F^4G^3 - B^3F^2G^4 - B^4F^3G^2\right]
\end{aligned}
\tag{97}
$$

The expressions for each of the coefficients are presented below:

$$
\begin{aligned}
b = \frac{1}{DEN}\Big\{ & S'\left[B^3E^4G^2 + B^2E^3G^4 + B^4E^2G^3 - B^3E^2G^4 - B^2E^4G^3 - B^4E^3G^2\right] \\
& -R'\left[B^3E^4F^2 + B^4E^2F^3 + B^2E^3F^4 - B^3E^2F^4 - B^2E^4F^3 - B^4E^3F^2\right] \\
& +T'\left[E^4F^2G^3 + E^3F^4G^2 + E^2F^3G^4 - E^2F^4G^3 - E^4F^3G^2 - E^3F^2G^4\right] \\
& -U'\left[B^4F^2G^3 + B^3F^4G^2 + B^2F^3G^4 - B^2F^4G^3 - B^3F^2G^4 - B^4F^3G^2\right]\Big\}
\end{aligned}
\tag{98}
$$

$$
\begin{aligned}
c = \frac{-1}{DEN}\Big\{ & S'\left[B^3E^4G + B^4EG^3 + BE^3G^4 - B^3EG^4 - BE^4G^3 - B^4E^3G\right] \\
& -R'\left[B^3E^4F + B^4EF^3 + BE^3F^4 - B^3EF^4 - BE^4F^3 - B^4E^3F\right]
\end{aligned}
\tag{99}
$$

$$+T'\left[E^4FG^3+E^3F^4G+EF^3G^4-EF^4G^3-E^4F^3G-E^3FG^4\right]$$

$$-U'\left[B^4FG^3+B^3F^4G+BF^3G^4-BF^4G^3-B^4F^3G-B^3FG^4\right]\Big\}$$

$$d=\frac{1}{DEN}\Big\{S'\left[B^2E^4G+B^4EG^2+BE^2G^4-B^2EG^4-BE^4G^2-B^4E^2G\right] \qquad (100)$$

$$-R'\left[B^2E^4F+BE^2F^4+B^4EF^2-B^2EF^4-BE^4F^2-B^4E^2F\right]$$

$$+T'\left[E^4FG^2+E^2F^4G+EF^2G^4-EF^4G^2-E^2FG^4-E^4F^2G\right]$$

$$-U'\left[B^4FG^2+B^2F^4G+BF^2G^4-BF^4G^2-B^2FG^4-B^4F^2G\right]\Big\}$$

$$e=\frac{-1}{DEN}\Big\{S'\left[B^2E^3G+B^3EG^2+BE^2G^3-B^2EG^3-BE^3G^2-B^3E^2G\right] \qquad (101)$$

$$-R'\left[B^2E^3F+B^3EF^2+BE^2F^3-B^2EF^3-BE^3F^2-B^3E^2F\right]$$

$$+T'\left[E^3FG^2+E^2F^3G+EF^2G^3-EF^3G^2-E^3F^2G-E^2FG^3\right]$$

$$-U'\left[B^3FG^2+B^2F^3G+BF^2G^3-BF^3G^2-B^2FG^3-B^3F^2G\right]\Big\}$$

Differentiating Equation (91) one can obtain the following expressions for the derivative at each of the five points shown in Figure 9a in terms of its distance from the center point.

$$y' = b + 2cx + 3dx^2 + 4ex^3 \tag{102}$$

$$y'_{(-2)} = b + 2cF + 3dF^2 + 4eF^3 \tag{103}$$

$$y'_{(-1)} = b + 2cG + 3dG^2 + 4eG^3 \tag{104}$$

$$y'_{(0)} = b \tag{105}$$

$$y'_{(+1)} = b + 2cB + 3dB^2 + 4eB^3 \tag{106}$$

$$y'_{(+2)} = b + 2cE + 3dE^2 + 4eE^3 \tag{107}$$

The three-point finite difference fit is obtained in a similar manner using the nomenclature presented in Figure 9b . In this case a quadratic equation is passed through three points with the center point again as the origin. The resulting equations are

$$y_{(-1)} \equiv R' = bG + cG^2 \tag{108}$$

$$y_{(0)} = a = 0 \tag{109}$$

$$y_{(+1)} \equiv T' = bB + cB^2 \tag{110}$$

In the three-point fit the analysis is greatly simplified as shown below:

$$DEN = G^2B - B^2G \tag{111}$$

$$b = \frac{1}{DEN}\left[G^2T' - B^2R'\right] \tag{112}$$

$$c = \frac{1}{DEN}\left[-GT' + BR'\right] \tag{113}$$

The corresponding expressions for the derivatives in the three-point fit are

$$y'_{(-1)} = b + 2cG \tag{114}$$

$$y'_{(0)} = b \tag{115}$$

$$y'_{(+1)} = b + 2cB \tag{116}$$

Figure 10 is presented to illustrate the various ways in which the finite difference formulas are used to obtain lateral derivatives. The typical cases shown illustrate most of the common situations. The same grid points are examined from both the radial and angular viewpoints since the points may be treated differently in the two directions. In the case of the five-point fit in the radial direction there are two off-side formulas, one for the outer radius and the other for the next to the outer radius point.

The grid network for the body-oriented cylindrical coordinate system used in the program offers considerable advantages in the formation of the lateral derivatives due to the manner of subscripting and handling grid points. With reference to Figure 8, it is noted that the j subscript, defining points in the angular direction, runs from $j = 1$ at $\theta = 0°$ (i.e., pitch plane) to $j = j_{max}$ at $\theta = 90°$. The i subscript, on the other hand, runs continuously from top to bottom for each j meridian plane. The j planes are thus symmetrically located about the $\theta = 90°$ plane as well as the pitch plane. Considering the mirror image of each j plane in the lower half of the flow field, one can compute radial derivatives in a continuous manner across the origin. One must reverse the sign of r and consider the properties in a Cartesian sense. In using image points to the left of the pitch plane it is also necessary to temporarily assign the opposite sign to the flow field properties $\bar{w}$ and ψ. The sign attached to the other flow field properties remains the same on either side of the pitch plane. Symmetry conditions also exist in computing lateral derivatives in the θ-direction using the pitch plane as a plane of reflection. This is the reason that θ-derivatives for points in the pitch plane and its neighboring plane are shown in Figure 10 as having been computed with a five-point central difference formula. Once one considers end points away from the pitch plane in the θ-direction, it is necessary to revert to an end point formula. This situation arises immediately when one considers using a cutoff flow field in the solution.

The five-point scheme for obtaining lateral derivatives is naturally more accurate than the three-point scheme because of the increased information that is made available. The central difference fit is preferred over an end-point fit because of its greater accuracy. Probably the most inaccurate evaluation of the lateral derivatives occurs when a three-point end-point formula must be used in both the radial and angular directions. Fortunately, this should not occur until very near the body after most of the flow field has been computed. It is quite important to make the transition from one radius to the next along the cutoff boundary as smooth as possible to minimize the use of the three-point end-point formula.

Body Determination

From the definition of ϕ and ψ given in the theoretical development, it follows from the existence of a single stagnation streamline which wets the entire body surface that,

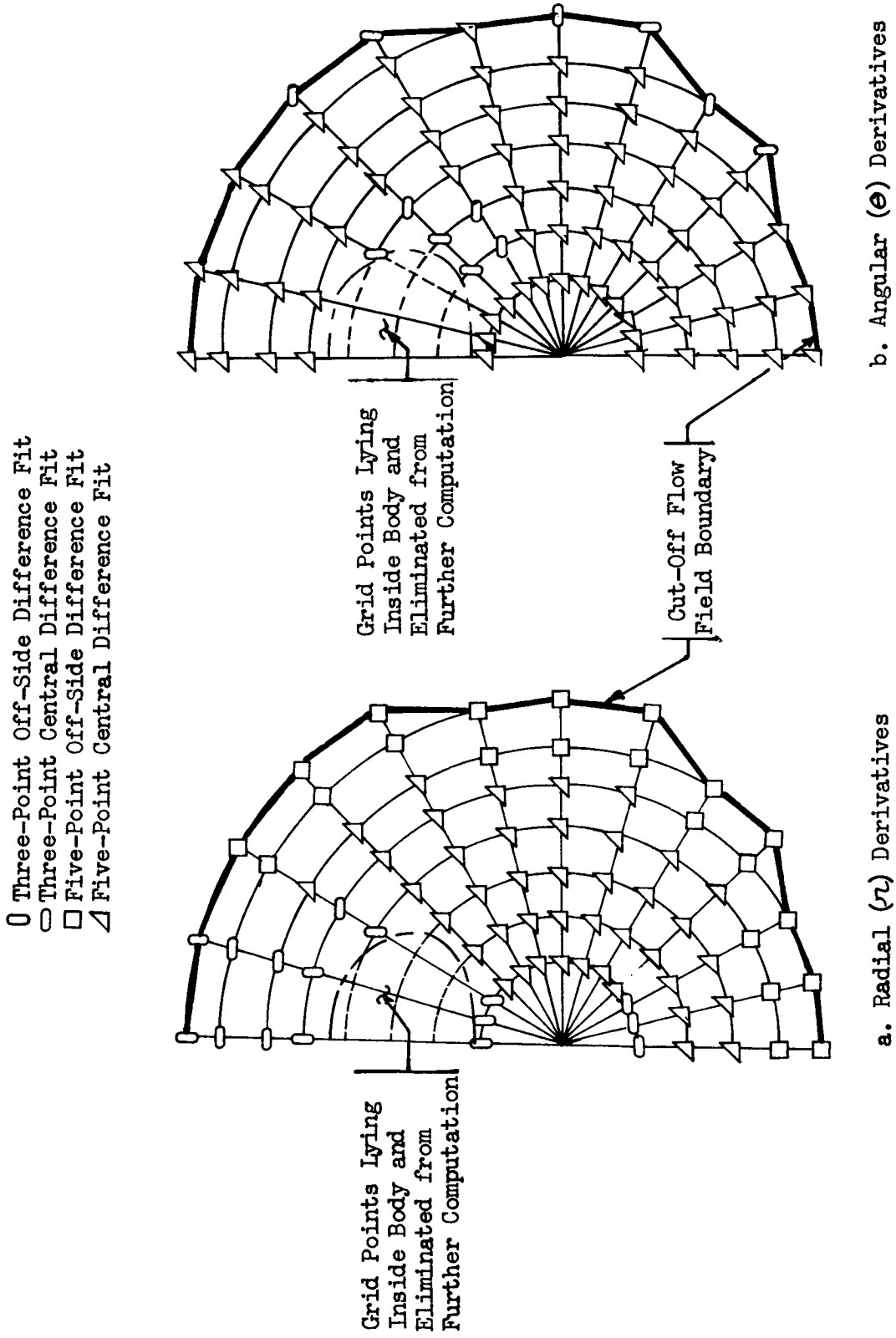

a. Radial (r) Derivatives

b. Angular (θ) Derivatives

Figure 10. Typical Finite Difference Fit for Lateral Derivatives

$$\phi_{BODY} = \phi_{STAG} \tag{117}$$

$$\psi_{BODY} = \psi_{STAG} \tag{118}$$

Since the stagnation streamline lies in the pitch plane

$$\psi_{STAG} = 0 \tag{119}$$

A simple procedure for locating the body surface outside of the pitch plane is to search for points where $\psi = 0$. At these points ϕ should be $\phi_{body} = \phi_{stag}$ = a constant. It was found that a more accurate procedure for computing ϕ_{stag} is by linearly interpolating between body points in the pitch plane to determine the value of ϕ at the location where $\bar{v} = 0$. This calculation is made in the Data Output Program.

It will be shown in the next section that the stream functions vary with X in such a manner that their X-derivatives become infinite at the body surface as shown in Figure 11 . The ψ curve is extrapolated to the body by fitting a parabola to the last two computed values while requiring symmetry about the $\psi = 0$ line.

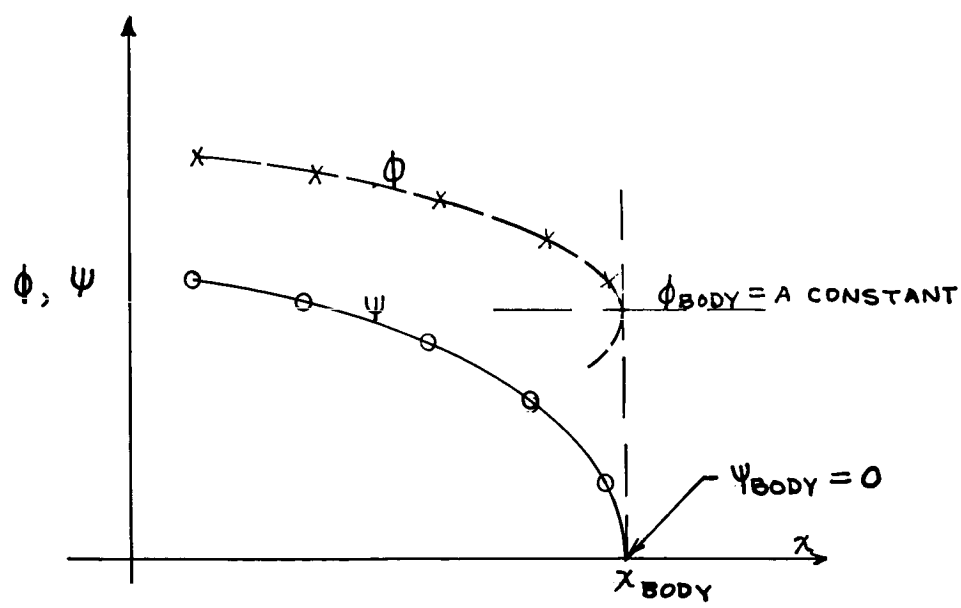

Figure 11 . Variation of Stream Functions in X -Direction

The plot of ϕ vs X for the same grid point has its vertex at $X = X_{body}$, this uniquely determining ϕ_{body}.

The gradients of the stream functions ϕ and ψ can be readily shown to be infinite at the body. Consider a flow field about a blunt body at angle-of-attack shown in Figure 12 .

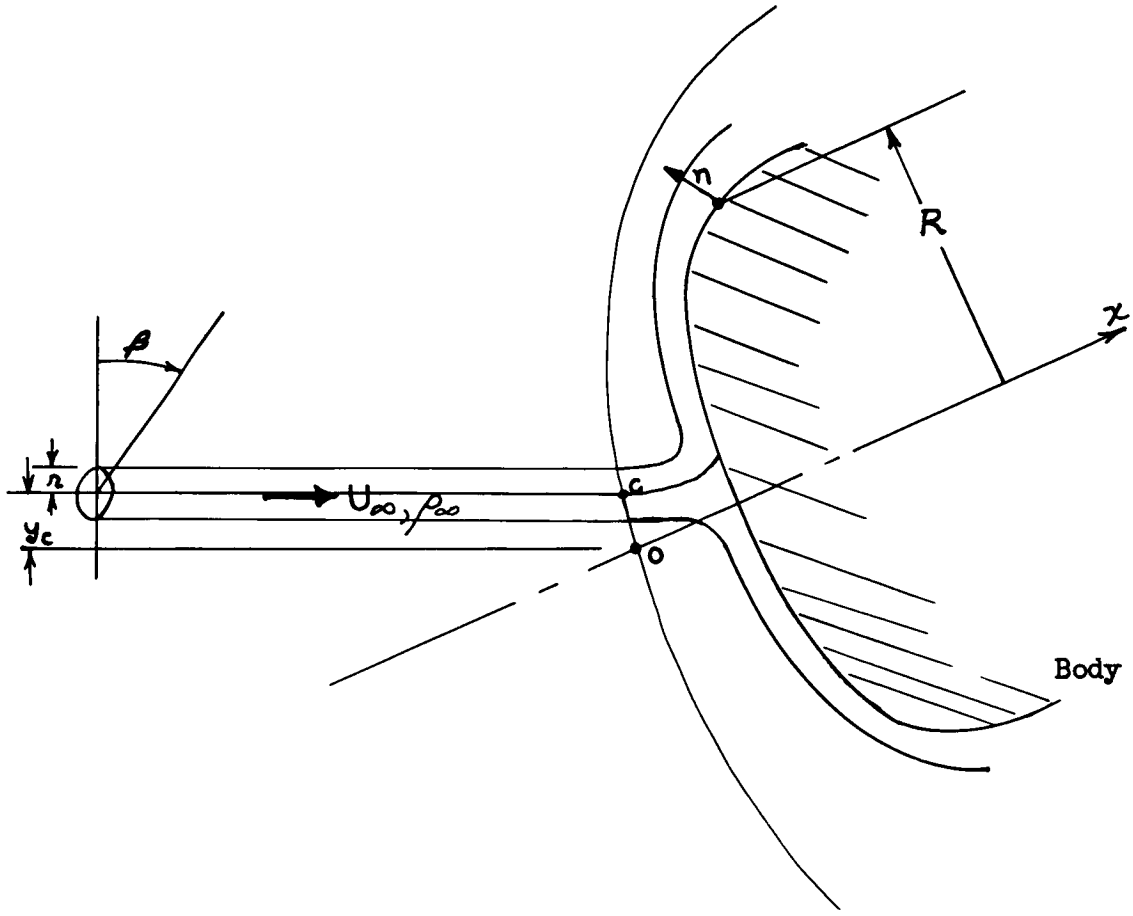

Figure 12 . Streamline Behavior Near the Body Surface

$$\text{MASS FLOW} = \pi \rho_\infty U_\infty r^2 = \int_0^r \int_0^{2\pi} \rho U f R \, d\theta \, dr \tag{120}$$

where f accounts for non-radial flow at radius R .

Differentiating the mass flow expression with respect to n,

$$2\pi\rho_\infty U_\infty r \frac{dr}{dn} = \int_0^{2\pi} \rho U f R d\theta = F(R, \theta, n)$$

From the definition of ϕ,

$$\phi = \sqrt{\rho_\infty U_\infty}\,(y_c + r\cos\beta)$$

or

$$\phi - \phi_c = \sqrt{\rho_\infty U_\infty}\; r\cos\beta$$

Differentiating this equation with respect to r,

$$\frac{d(\phi-\phi_c)}{dr} = \sqrt{\rho_\infty U_\infty}\;\cos\beta$$

Since

$$\frac{dr}{dn} = \frac{dr}{d(\phi-\phi_c)}\,\frac{d(\phi-\phi_c)}{dn}$$

Thus,

$$\frac{2\pi\rho_\infty U_\infty(\phi-\phi_c)\,d(\phi-\phi_c)}{\left(\sqrt{\rho_\infty U_\infty}\cos\beta\right)^2 dn} = \int_0^{2\pi} \rho U f R d\theta = F(R,\theta,n) \qquad (121)$$

The variables ρ, U, f, and $\cos\beta$ may be expanded in a Taylor series at the body surface. It can be shown that after performing the above integration, and then evaluating the resulting equation on the surface that to first

order in n all terms of the series drop out except the constant values on the surface. The final form is,

$$\int_0^{\phi-\phi_c} (\phi-\phi_c)\, d(\phi-\phi_c) = n\, G(R,\theta)$$

or

$$(\phi-\phi_c)^2 = 2n\, G(R,\theta) \tag{122}$$

Thus ϕ varies parabolically with n at the body surface. ϕ_c is recognized as the body value of ϕ. The analogous derivation of the behavior of ψ is straightforward.

A simple explanation of the existence of infinite gradients of ϕ and ψ at the body surface may also be found from examination of Equation (66). Since both $\nabla\phi$ and $\nabla\psi$ are normal to the surface and thus parallel, we must have an indeterminancy with either $\nabla\phi = \infty$ or $\nabla\psi = \infty$ or both $\nabla\phi$ and $\nabla\psi = \infty$ in order to have a finite U result from the vector cross product.

Locating the body in the pitch plane by parabolic extrapolation of ϕ has two problems,

1. The calculation is inaccurate near the stagnation point where the flow velocities approach zero.

2. ϕ may equal ϕ_{body} at points other than on the body surface. This introduces the difficult problem of discriminating between correct and incorrect body location predictions.

Both problems have been overcome in the program by using a simple approximation that is considered acceptable to engineering accuracy. The body location predictions for the pitch plane are assumed to be identical to the predictions for the nearest grid plane ($j = 2$). This is justified by the following considerations,

1. Only axially symmetric bodies are considered.

2. The variation of predicted body shape with θ near the pitch plane is at most a $\cos\theta$ type effect due to symmetry of the flow field with respect to the pitch plane.

3. The grid plane nearest the pitch plane may be located by the program user at such a value of θ that the error introduced may be controlled.

The procedure in the program for locating body points is conducted in the following manner. After computing properties in the kth plane, a prediction of the distance to the body is made for each remaining (i, j)

grid point. A check is then made to see if the predicted body point lies within the next integration interval. If so, the point is identified in such a manner that it will be dropped during the predictor step in the next integration interval. The body properties for these points are obtained by linear extrapolation.

After identifying these points, the program also checks the remaining available grid points for two conditions. First, are there any pockets in the grid network where only two points remain. This check is made in both the Ω and θ directions. These points are also identified in a special manner as it is impossible to determine lateral derivatives for these points after performing the predictor integration step in the next interval. The reason lies in the fact that properties are not determined for grid points lying within the body. Therefore, properties are not computed on the next marching plane for those grid points intersecting the body in the next integration interval. This means there would only be two remaining points in this local region on the next plane at the end of the predictor step. Thus, it would be impossible to finish the corrector step in the integration procedure since the program requires a minimum of three points in any direction to form lateral derivatives. The grid points falling in this category are permitted to predict properties on the next plane so that they will be of aid in forming lateral derivatives for adjacent points. They are subsequently dropped on the integration corrector cycle in the next interval. Using the predicted body location, the program extrapolates for the body properties at these grid points.

The second check is performed on the remaining grid points and has to do more with the accuracy of subsequent calculations. It is a check to identify those groups of grid points in which there are only three points remaining at the completion of the integration cycle for the next interval. While there are sufficient points (i.e., the minimum of three) to form lateral derivatives in both the predictor and corrector integration steps, the accuracy of these derivatives starts to become questionable beyond one more integration interval due to the use of end-point lateral derivative formulas. Therefore, the program identifies these points in a manner that they also will be dropped after the next interval. Body properties for these points are obtained by linear extrapolation.

Two other conditions enter into this body determination or point-dropping procedure. There is provision in the program for dropping points when the grid points approach singularities in the flow field and computations become too inaccurate to continue. Although the source of these singularities and the specific tests used for their control has already been discussed, it is appropriate to restate this information. One singularity results from the alignment of the local characteristic line with the marching plane. This condition is determined by observing when the normal Mach number approaches unity. The other singularity occurs when the marching plane becomes aligned with the local streamline slope. The previously described test for each of these conditions is made for each grid point on the corrector integration step, and the point is dropped upon failing the test. Again the body properties are obtained by extrapolation. Although the singular region

may be confined to a thickness of only a few marching planes at most, no attempt is made to resume the forward integration of this point after passing through the singular region. In theory, however, it should be possible to resume the calculations for this grid point downstream of the singularity. The extrapolation for body properties for points encountering the second singularity does not produce unreasonable results as this singularity generally occurs very near the body surface and only a short extrapolation is required. The extrapolation for points failing the normal Mach number test may be over a greater distance, and the resulting accuracy may be more questionable. However, these points usually lie at the outer edges of the flow field where the flow is supersonic and are not essential to the required solution.

Iterative Convergence Technique

Error Measurement

The body obtained from a given shock shape is introduced into the iteration (influence coefficient) subroutine as a series of points having the same radial and angular coordinates as the grid points for the flow field integration. The errors between the predicted and desired body are defined to be the distances between the bodies as measured along a perpendicular from the desired body to the body predicted by the shock equation. This perpendicular is erected at certain points on the desired body which are designated control points, and the errors at the control points will be called simply the errors.

Since the predicted body is given in terms of discrete points and not an analytic curve the predicted body surface must be defined in the region between these computed body points. The approach used is to connect adjacent points with straight line segments. The error is the distance along the normal from the body to the intersection of the normal and the line segment as shown in Figure 13. The control point will always have the same r as a predicted body point so that the errors will approach zero as the iteration procedure converges.

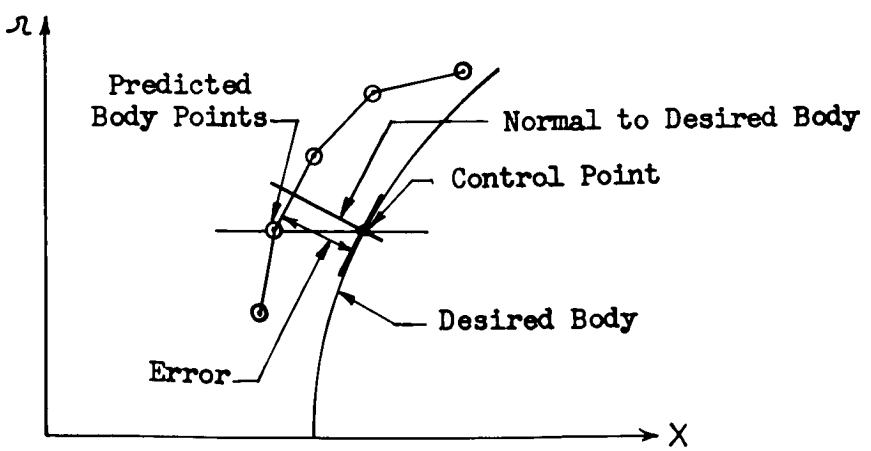

Figure 13. Measurement of Predicted Body Shape Errors

In order to establish some reference system from which to measure the errors a particular point on the desired body is designated as a <u>translation point.</u> This point, shown in Figure 14, has r and θ coordinates equal to that of a predicted body point, and after each run the predicted body point and this translation point on the desired body are made to coincide by translating the entire desired body shape. Thus, errors are a measure of the body shape error, and the X -translational location of the body is not considered in the error evaluation.

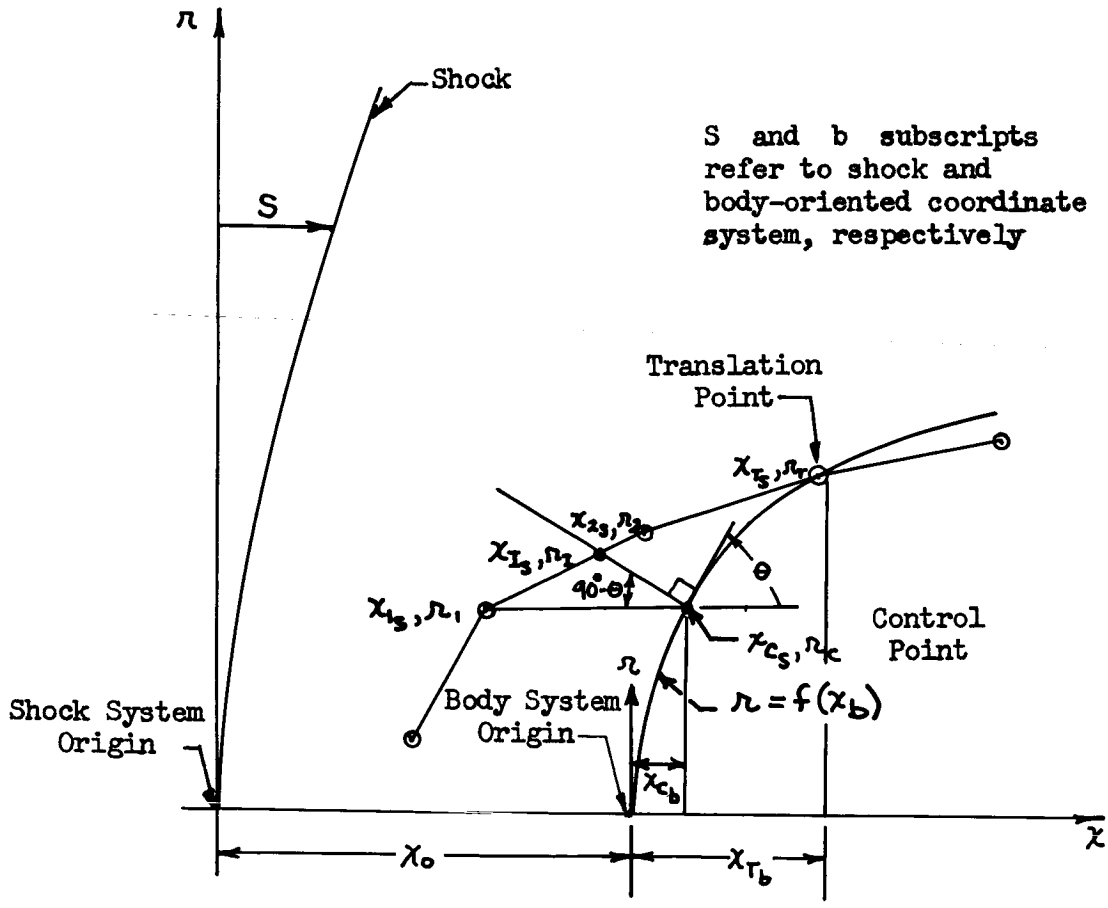

Figure 14. Location of Translation and Control Points

The control and translation points are initially given in terms of r's and θ's. The equations for the desired body are given in terms of a body oriented system. Then knowing the r_T and r_c coordinates, the x coordinates x_{c_b} and x_{T_b} can be calculated. x_{T_s} is the coordinate in the shock oriented system and is used in fixing the origin of the body oriented system. The quantity x_{T_s} is the x coordinate of the predicted body point at that r_T in the given plane.

The origin of the body oriented system is fixed at $x_o = (x_{T_s} - x_{T_b})$ for all planes, and the control points are given in the shock oriented system as

$$x_{c_s} = (x_{T_s} - x_{T_b}) + x_{c_b}$$

All the predicted body points are computed in terms of a shock oriented system so no conversion is necessary.

The error is the distance between (x_{c_s}, r_c) and (x_{I_s}, r_I) where the latter point represents the intersection of the normal and the predicted body line segment.

Given the body equation $r = f(x_b)$. A conversion to the shock oriented system can be made by the substitution

$$r = f(x_s - (x_{T_s} - x_{T_b})) = g(x_s)$$

Then $\left(\frac{dr}{dx_s}\right)_{x_{c_s}, r_c}$ = slope of curve = $\tan\theta$

and the slope of the normal is

$$-\mathrm{TAN}\,(90^\circ - \theta) = -\mathrm{CTN}\,\theta = -\frac{1}{\mathrm{TAN}\,\theta}$$

or $-\left(\frac{dx_s}{dr}\right)_{x_{c_s}, r_c}$.

The r intercept of the normal is at

$$r = r_c + \left(\frac{dx_s}{dr}\right)_{x_{c_s}, r_c} \cdot x_{c_s}$$

Then the equation of the normal becomes

$$r = -\left(\frac{dx_s}{dr}\right)_{x_{c_s}, r_c} \cdot x + \left(r_c + \left(\frac{dx_s}{dr}\right)_{x_{c_s}, r_c} \cdot x_{c_s}\right) \tag{123}$$

The equation of the predicted body line segment is similarly found to be

$$r = \left(\frac{r_2 - r_1}{x_{2_s} - x_{1_s}}\right) x + \left(r_1 - \left(\frac{r_2 - r_1}{x_{2_s} - x_{1_s}}\right) \cdot x_{1_s}\right) \tag{124}$$

When linear Equations (123) and (124) are solved simultaneously, the solution becomes

$$x_{I_s} = -\frac{\left(r_1 - \left(\frac{r_2 - r_1}{x_{2_s} - x_{1_s}}\right) x_{1_s}\right) - \left(r_c + \left(\frac{dx_s}{dr}\right)_{x_{c_s}, r_c} \cdot x_{c_s}\right)}{\left(\frac{r_2 - r_1}{x_{2_s} - x_{1_s}}\right) + \left(\frac{dx_s}{dr}\right)_{x_{c_s}, r_c}}$$

$$= \frac{\left(\frac{r_2 - r_1}{x_{2_s} - x_{1_s}}\right) x_{2_s} + \left(\frac{dx_s}{dr}\right)_{x_{c_s}, r_c} \cdot x_{c_s}}{\left(\frac{r_2 - r_1}{x_{2_s} - x_{1_s}}\right) + \left(\frac{dx_s}{dr}\right)_{x_{c_s}, r_c}} \tag{125}$$

and

$$r_I = -\left(\frac{dx_s}{dr}\right)_{x_{c_s}, r_c} \left(\frac{\left(\frac{r_2 - r_1}{x_{2_s} - x_{1_s}}\right) x_{1_s} + \left(\frac{dx_s}{dr}\right)_{x_{c_s}, r_c} \cdot x_{c_s}}{\left(\frac{r_2 - r_1}{x_{2_s} - x_{1_s}}\right) + \left(\frac{dx_s}{dr}\right)_{x_{c_s}, r_c}}\right) \tag{126}$$

$$+ \left(r_c + \left(\frac{dx_s}{dr}\right)_{x_{c_s}, r_c} \cdot x_{c_s}\right)$$

If $r_I > r_2$, then the equation of the next upper line segment is computed and the solution found again.

If $r_I < r_1$, then the equation of the next lower line segment is computed and the solution found again.

The solution must fall within the defined body points on that particular plane unless a special input selection is made. After finding the correct solution, the error is

$$\epsilon_i = \pm\sqrt{(x_{I_s} - x_{c_s})^2 - (r_I - r_c)^2} \tag{127}$$

The positive sign is given if $x_{I_s} > x_{c_s}$, negative if $x_{c_s} > x_{I_s}$. The body is always assumed to have a positive first derivative.

Desired Body Definition with Options

The procedure has just been described for computing errors between the predicted and desired body. The predicted body points are outputs from the integration procedures in the main program. The desired body points and shapes must be computed separately for the applicable body shape option. General cylindrical coordinate systems will be used in the following derivations. In all cases the x-axis lies on the axis of symmetry of the desired body. The desired body shape is basically entered into the program and computed in a system having its origin at the intersection of the x-axis with the body. For the special option of a hemispherically blunted general body, it has been found convenient to enter body shape parameters into the program referenced to the station of tangency of the hemisphere to the second body segment. A transformation of the origin to the x-axis intersection with the body is accomplished internally within the program.

General Body. The general body consists of up to four segments, each segment consisting of a power series of up to six terms. So, for each segment

$$r = \sum_{n=0}^{5} a_{n,i} (x_b - x_{b_i})^n \qquad i = 1,4 \tag{128}$$

The equations are written in terms of a body oriented system, Figure 15 . The point for fixing the body in the shock oriented system is given as r_T along with the appropriate segment and plane. The control and translation points are limited to r's equal to those of the grid coordinates used for the flow field solution.

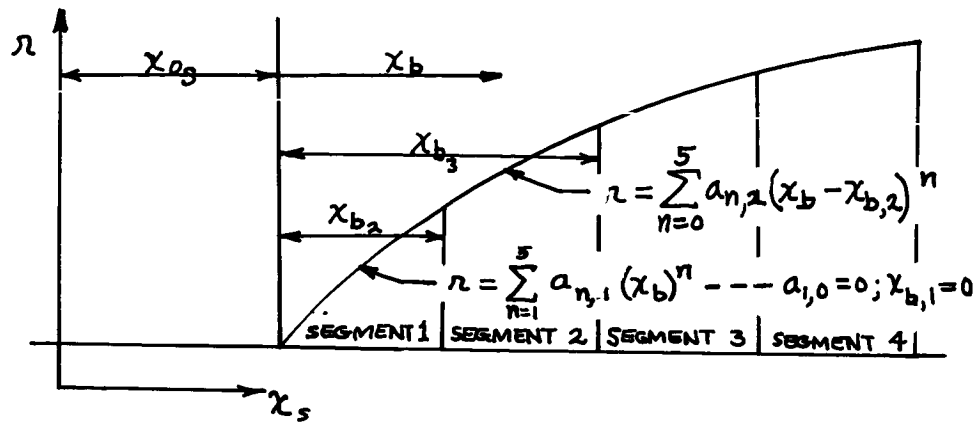

Figure 15 . Definition of General Body Shape

Each segment will start at $x_{b,i}$ in the body oriented system and continue until $x_{b,i+1}$. A segment begins at an $r_i = a_{o,i}$. The segments are tangent at their points of intersection.

If the translation point is given at $r = r_T$ in segment p then the equation

$$r_T = \sum_{n=0}^{5} a_{n,p} \left(x_{T_b} - x_{b,p}\right)^n$$

is solved for x_{T_b} by the Newton-Raphson iterative process. After completing an initial run with the program the body system origin is displaced from the shock system origin by an amount

$$x_{o_s} = \left(x_{T_s} - x_{T_b}\right)$$

where x_{T_s} is the x coordinate of the predicted body point at the r_T and θ_T values of the translation point.

A transformation of the general equation to the shock oriented system can then be made:

$$r = \sum_{n=0}^{5} a_{n,i} \left(x - x_{b,i} - (x_{T_s} - x_{T_b})\right)^n \qquad i = 1, 4$$

$$r = \sum_{n=0}^{5} a_{n,i} \left(x - x_{b,i} - x_{T_s} + x_{T_b}\right)^n \qquad i = 1, 4$$

Each control point x_{c_s} in segment q is determined iteratively from the equation

$$r_c = \sum_{n=0}^{5} a_{n,q} \left(x_{c_s} - x_{b,q} - x_{T_s} + x_{T_b}\right)^n$$

The derivative at a point on the desired body is required for the error calculation and is given by

$$\left(\frac{dx_s}{dr}\right)_i = \frac{1}{\left(\frac{dr}{dx_s}\right)_i} = \frac{1}{\sum_{n=1}^{5} n\, a_{n,i} \left(x - x_{b,q} - x_{T_s} + x_{T_b}\right)^{n-1}} \qquad i = 1, 4$$

or on the qth segment

$$\left(\frac{dx_s}{dr}\right)_{x_{c_s}, r_c} = \frac{1}{\sum_{n=1}^{5} n\, a_{n,q} \left(x_{c_s} - x_{b,q} - x_{T_s} + x_{T_b}\right)^{n-1}}$$

Then $(dx_s/dr)_{x_{c_s}, r_c}$, x_{c_s} and the appropriate x_{1_s}, x_{2_s}, r_1 and r_2 of the body determined by the shock are substituted in Equations 125, 126, and 127 to obtain the error.

General Body with Hemispherical Nose. The first segment of the general body may be fitted with a hemispherical nose as shown on Figure 16 , the radius being uniquely determined by the equation of the second segment under the assumption of continuous values and first derivatives between segments. Thus the only input will be

$$r = \sum_{n=0}^{5} a_{n,i} \left(\bar{x}_b - \bar{x}_{b,i}\right)^n \qquad i = 2,4 \qquad (129)$$

where now $\bar{x}_{b,i}$ is measured from the start of the second segment and therefore $\bar{x}_{b,2} = 0$. Again, all four segments need not be used but a minimum of two, including the hemisphere, are necessary for a solution.

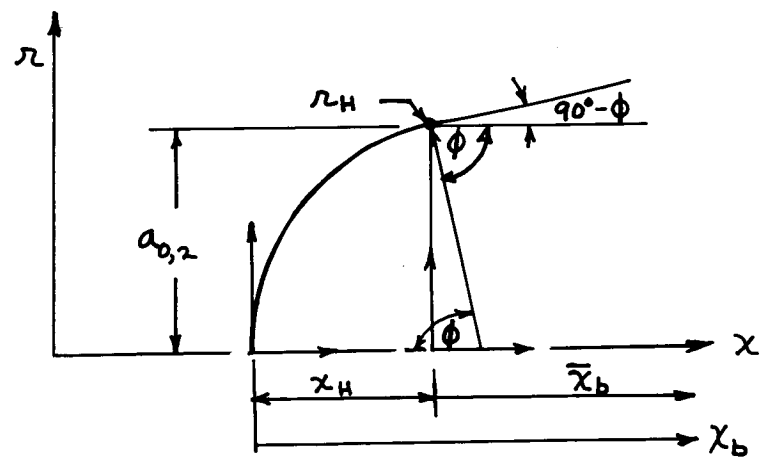

Figure 16 . General Body Shape with Hemispherical Nose

Assuming tangency of the hemisphere to the second segment,

$$\left(\frac{d}{d\bar{x}_b}\left(\sum_{n=0}^{5} a_{n,2}\,\bar{x}_b^{\,n}\right)\right)_{x=0} = \mathrm{TAN}\,(90° - \phi) = \mathrm{CTN}\,\phi = a_{1,2}$$

which is a constant. It is obvious that

$$\left(\sum_{n=0}^{5} a_{n,2}\,\bar{x}_b^{\,n}\right)_{\bar{x}_{b,2}=0} = r_H \sin\phi = a_{0,2}$$

Therefore:

$$r_H = \frac{a_{0,2}}{\sin\phi}$$

$$= a_{0,2}\sqrt{1 + \operatorname{ctn}^2\phi}$$

$$= a_{0,2}\sqrt{1 + a_{1,2}^2} \qquad (130)$$

and thus r_H is automatically determined by the second segment.

The equation of the hemisphere can be expressed as

$$x_b = -\sqrt{r_H^2 - r^2} + r_H$$

This places the hemisphere in a coordinate system with the origin at the intersection of the hemisphere and the x axis. This coordinate system is the one required by the program in determining the errors of the control points while matching the predicted body with the desired body at the translation point. Substitution of Equation (130) for r_H yields for the hemisphere

$$x_b = -\sqrt{a_{0,2}^2\left(1 + a_{1,2}^2\right) - r^2} + a_{0,2}\sqrt{1 + a_{1,2}^2} \qquad (131)$$

If the translation point falls on the hemisphere then,

$$x_{T_b} = -\sqrt{a_{0,2}^2\left(1 + a_{1,2}^2\right) - r_T^2} + a_{0,2}\sqrt{1 + a_{1,2}^2} \tag{132}$$

The equations of the other segments must also be put in the same reference system. This may be done by translating the segments a distance x_H which represents the distance between the origin and the start of the second segment. From geometry

$$x_H = r_H\left(1 - \cos\phi\right)$$

$$= r_H\left(1 - \mathrm{CTN}\,\phi\,\sin\phi\right)$$

$$= a_{0,2}\sqrt{1 + a_{1,2}^2} - a_{1,2}\,a_{0,2} \tag{133}$$

Where again

$$\bar{x}_b = x_b - x_H \tag{134}$$

If the translation point falls in the pth segment, $p > 1$, x_{T_b} must be solved iteratively from Equation (129) which can be rewritten using Equations (133) and (134) as follows:

$$r_T = \sum_{n=0}^{5} a_{n,2}\left(x_{T_b} - \bar{x}_{b,p} - x_H\right)^n \tag{135}$$

Now all the body fit equations may be transformed to the shock oriented system. Using the basic transformation equation relating shock and body oriented coordinate systems, as previously derived

$$x_s = x_b + \left(x_{T_s} - x_{T_b}\right) \tag{136}$$

it is simple to substitute for x_b from Equation (131) to find for the hemisphere,

$$x_s = -\sqrt{a_{0,2}^2\left(1 + a_{1,2}^2\right) - r^2} + a_{0,2}\sqrt{1 + a_{1,2}^2} + \left(x_{T_s} - x_{T_b}\right) \qquad i = 1$$

For all other segments Equations (133),(134) and (136) when substituted into Equation (129) yield

$$r = \sum_{n=0}^{5} a_{n,i}\left(x - \bar{x}_{b_i} - \left(a_{0,2}\sqrt{1 + a_{1,2}^2} - a_{1,2}\, a_{0,2}\right) - x_{T_s} + x_{T_b}\right)^n \qquad i = 2, 4$$

where x_{T_s} is the matching point of the predicted body.

Similarly, each control point x_{c_s} in segment 1 is determined from the equation

$$x_{c_s} = -\sqrt{a_{0,2}^2\left(1 + a_{1,2}^2\right) - r_c^2} + a_{0,2}\sqrt{1 + a_{1,2}^2} + \left(x_{T_s} - x_{T_b}\right)$$

and in segment q, $q > 1$, x_{c_s} must be solved for iteratively from

$$r_c = \sum_{n=0}^{5} a_{n,q}\left(x_{c_s} - \bar{x}_{b,q} - \left(a_{0,2}\sqrt{1 + a_{1,2}^2} - a_{1,2}\, a_{0,2}\right) - x_{T_s} + x_{T_b}\right)^n$$

In the first segment

$$\left(\frac{d\chi_s}{dr}\right)_{\chi_{c_s},\, r_c} = -\frac{r_c}{\sqrt{a_{0,2}^2\left(1+a_{1,2}^2\right)-r_c^2}} \tag{137}$$

and for the q th segment, $q>1$

$$\left(\frac{d\chi_s}{dr}\right)_{\chi_{c_s},\, r_c} = \frac{1}{\sum_{n=1}^{5} n\, a_{n,q}\left(\chi_{c_s}-\bar{\chi}_{b_q}-\left(a_{0,2}\sqrt{1+a_{1,2}^2}-a_{1,2}\,a_{0,2}\right)-\chi_{T_s}+\chi_{T_b}\right)^n} \tag{138}$$

where χ_{T_b} is computed from either Equations (132) or (135). Now in Equations (137) or (138) χ_{c_s} and the appropriate $\chi_{1_s}, \chi_{2_s}, r_1$ and r_2 may be used to obtain the error by substitution in Equations (125), (126), and (127).

Apollo. The Apollo shape, Figure 17, is automatically determined by option, and only the translation and control points need be specified. The shape is a spherical segment bounded by a toroidal shoulder. It is uniquely defined by R_{H_1}, R_{H_2} and $d/2$ which are 15.4 ft, 0.642 ft, and 6.42 ft.

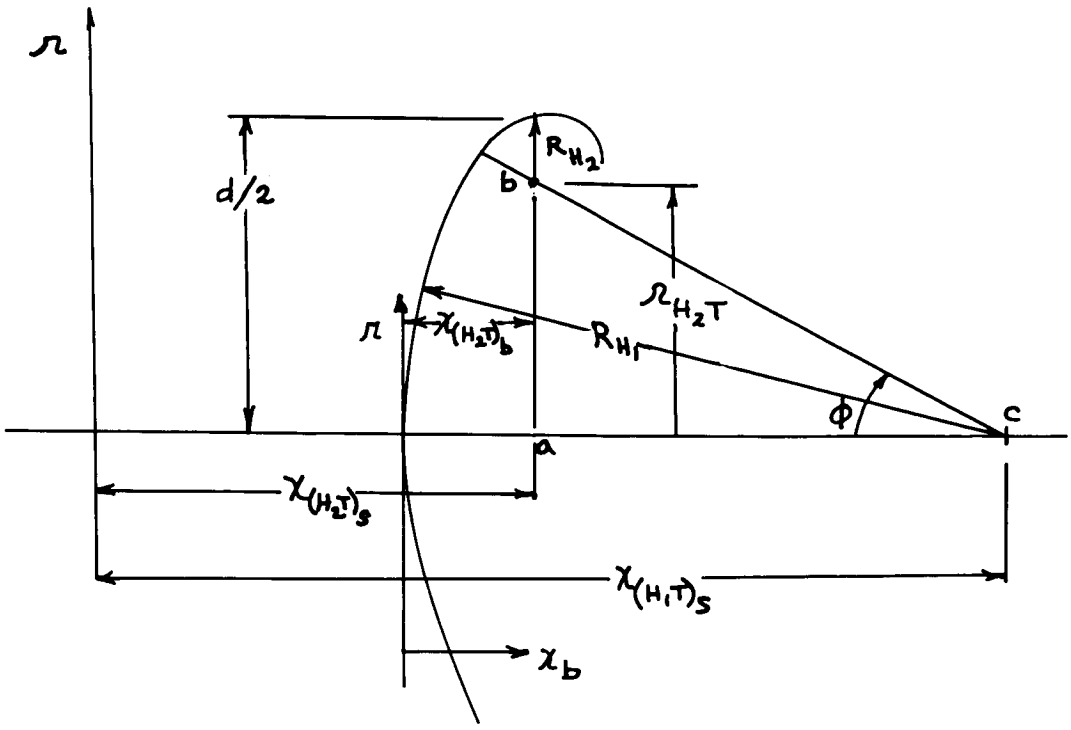

Figure 17. Apollo Command Module Shape

The two segments may each be represented in a body centered coordinate system by equations of the form,

$$x_b = -\sqrt{R_{H_1}^2 - r^2} + R_{H_1} \qquad \text{(for the spherical segment 1)} \qquad (139)$$

$$x_b = -\sqrt{R_{H_2}^2 - (r - r_{H_2T})^2} + x_{(H_2T)_b} \qquad \text{(for the toroidal shoulder, segment 2)} \qquad (140)$$

The quantities $x_{(H_2T)_b}$ and r_{H_2T} are functions of the geometry:

$$r_{H_2T} = \frac{d}{2} - R_{H_2} \tag{141}$$

$$x_{(H_2T)_b} = R_{H_1} - (R_{H_1} - R_{H_2}) \cos\phi$$

$$= R_{H_1} - (R_{H_1} - R_{H_2})\sqrt{1 - \sin^2\phi}$$

Where

$$\sin\phi = \frac{\frac{d}{2} - R_{H_2}}{R_{H_1} - R_{H_2}} \quad .$$

Therefore

$$x_{(H_2T)_b} = R_{H_1} - \sqrt{(R_{H_1} - R_{H_2})^2 - \left(\frac{d}{2} - R_{H_2}\right)^2} \quad . \tag{142}$$

Substituting (141) and (142) in (139) and (140), the final equations in a body system become

$$x_b = -\sqrt{R_{H_1}^2 - r^2} + R_{H_1}$$

$$x_b = -\sqrt{R_{H_2}^2 - \left(r - \frac{d}{2} + R_{H_2}\right)^2} + R_{H_1}$$

$$-\sqrt{(R_{H_1} - R_{H_2})^2 - \left(\frac{d}{2} - R_{H_2}\right)^2}$$

The translation distance x_{T_b} may now be found from

$$x_{T_b} = -\sqrt{R_{H_1}^2 - r_T^2} + R_{H_1} \tag{143}$$

or

$$x_{T_b} = -\sqrt{R_{H_2}^2 - \left(r_T - \frac{d}{2} + R_{H_2}\right)^2} + R_{H_1} \tag{144}$$

$$-\sqrt{\left(R_{H_1} - R_{H_2}\right)^2 - \left(\frac{d}{2} - R_{H_2}\right)^2}$$

depending upon whether the point lies in the first or second segment respectively.

The body equation may now be fixed in a shock oriented system by using the appropriate predicted body point:

$$x = -\sqrt{R_{H_1}^2 - r^2} + \left(R_{H_1} - x_{T_b} + x_{T_s}\right)$$

(for the spherical segment)

and

$$x = -\sqrt{R_{H_2}^2 - \left(r - \frac{d}{2} + R_{H_2}\right)^2} + \left(R_{H_1} - \sqrt{\left(R_{H_1} - R_{H_2}\right)^2 - \left(\frac{d}{2} - R_{H_2}\right)^2}\right.$$

$$\left. - x_{T_b} + x_{T_s}\right)$$

(for the toroidal segment)

or

$$x = -\sqrt{R_{H_1}^2 - r^2} + x_{(H_1T)_s} \tag{145}$$

(for the spherical segment)

and

$$x = -\sqrt{R_{H_2}^2 - \left(r - \frac{d}{2} + R_{H_2}\right)^2} + x_{(H_2T)_s} \tag{146}$$

(for the toroidal segment)

where

$$x_{(H_1T)_s} = \left(R_{H_1} - x_{T_b} + x_{T_s}\right)$$

and

$$x_{(H_2T)_s} = \left(R_{H_1} - \sqrt{(R_{H_1} - R_{H_2})^2 - \left(\frac{d}{2} - R_{H_2}\right)^2} - x_{T_b} - x_{T_s}\right)$$

where the appropriate value of x_{T_b} is substituted from Equation (143) or (144). Each of the control points is solved from

$$x_{c_s} = -\sqrt{R_{H_1}^2 - r_c^2} + x_{(H_1T)_s}$$

(for the spherical segment)

and

$$x_{c_s} = -\sqrt{R_{H_2}^2 - \left(r_c - \frac{d}{2} + R_{H_2}\right)^2} + x_{(H_2T)_s}$$

(for the toroidal segment)

On the spherical segment from Equation (145)

$$\left(\frac{dx_s}{dr}\right)_{x_{c_s}, r_c} = \frac{\sqrt{R_{H_1}^2 - r_c^2}}{r_c} . \tag{147}$$

Similarly on the toroidal segment from Equation (146)

$$\left(\frac{dx_s}{dr}\right)_{x_{c_s}, r_c} = \frac{\sqrt{R_{H_2}^2 - \left(r_c - \frac{d}{2} + R_{H_2}\right)^2}}{r_c - \frac{d}{2} + R_{H_2}} \tag{148}$$

Equations (147) and (148), x_{c_s} and the appropriate x_{1_s}, x_{2_s}, r_1 and r_2 can now be used to obtain the body error by substitution in Equations (125), (126), and (127).

Integration Procedure

The integration procedure used in the computer program is a fourth-order Runge-Kutta scheme modified to include the Gill correction. This procedure is described in detail in Reference 20 . It employs a fixed step-size or integration interval, entered as input to the program, throughout the entire solution. The only difference over the method presented in Reference 20 is the acceptance of data obtained with the corrector step at the intermediary plane. Normally, the Runge-Kutta procedure employs four steps to complete a cycle. The step size is automatically halved, and the first and second steps determine predicted and corrected conditions on the intermediary plane. The third and fourth steps pertain to the predictor and corrector steps for the second half of the entire interval. Thus, two marching planes of data are obtained by the program for a complete cycle of the Runge-Kutta procedure. In most solutions a slightly greater difference between predicted and corrected results has been noticed at the intermediary plane than at the end of the cycle, but the results are still considered sufficiently accurate and acceptable for the purpose of supplying detail on the behavior of the flow field properties.

In the early stages of program development a simple second order predictor integration scheme was tried but proved to be too inaccurate in its determination of the stream functions. The merit of a predictor only scheme of integration is obviously the shorter program operating time due to the elimination of the corrector cycle. An attempt was made to improve the accuracy of this scheme by effectively increasing the order. However, this would have required carrying data on an additional marching plane for use in the computations and the program storage space was too limited to do this. Thus, this scheme was abandoned in favor of the Runge-Kutta procedure.

Data Smoothing

The properties $p, \rho, u, \bar{v}, \bar{w}, \phi$ and ψ are smoothed individually at all grid points (i, j). A least square parabola is fitted successively to sets of five points with the center point value being adjusted to the value of the parabola. The data are smoothed first versus r, then versus θ. The following special considerations are observed,

1. Symmetry requirements with respect to $\theta = 0°$, 180° (the pitch plane) are observed by adding image points. The grid system and property definitions require treatment of the data as shown in Figure 18 . The antisymmetric behavior results from the cartesian form of the definitions of $\bar{w}$ and ψ .

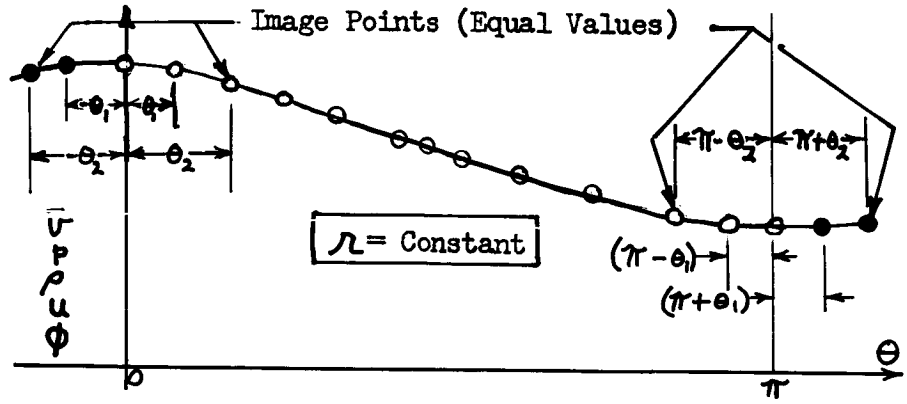

a. Symmetrical Properties

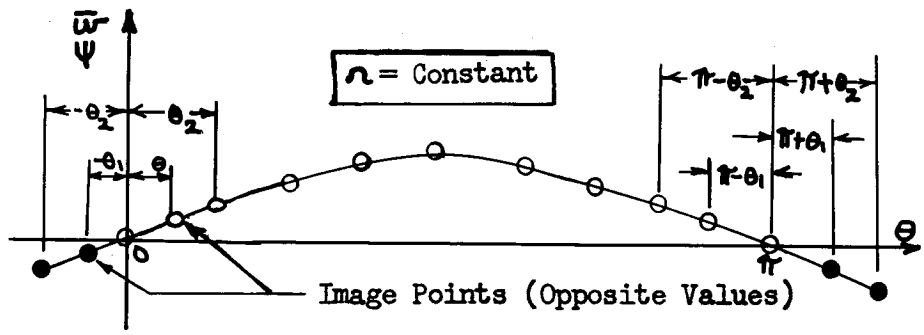

b. Antisymmetrical Properties

Figure 18. Symmetry Properties of Data About Pitch Plane

2. The variation of properties along a coordinate j = constant requires the transformations shown in Figure 19 in crossing the axis at $\Omega = 0$.

The symmetry about the pitch plane establishes the relationship between values on the lines **ob** and **oc**. The program computes values on the bent line **aoc** whereas a smooth analytic variation of the properties is found along the line **aob**. The data on **aoc** are transformed, as shown in Figure 19, to represent data on the line **aob**. The data are smoothed and then transformed back to the desired location on **aoc**.

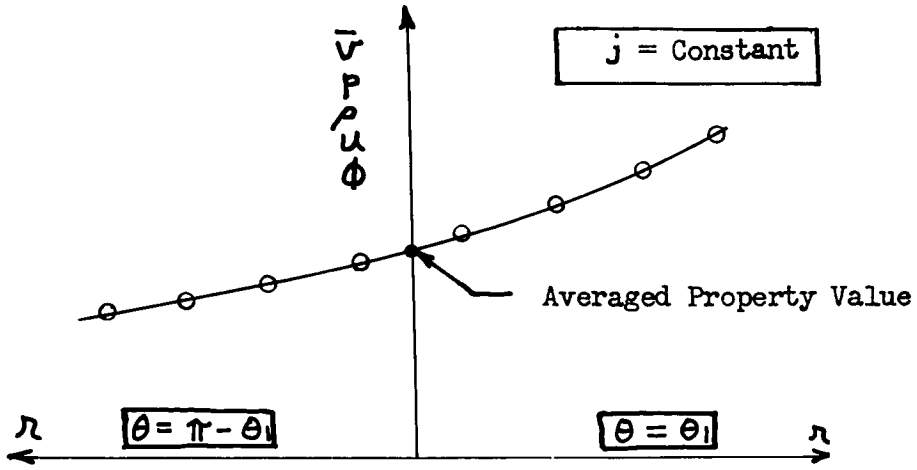

a. Properties Having Non-Zero Value at Axis

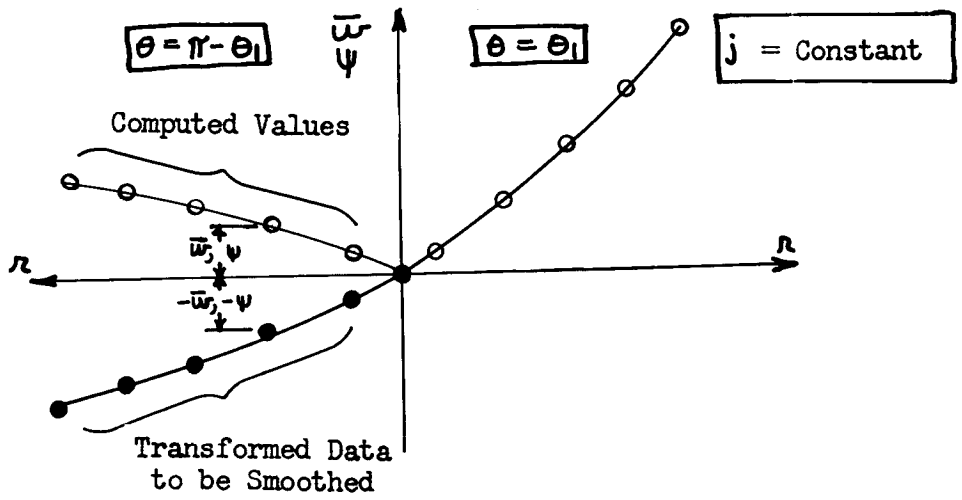

b. Properties Having Zero Value at Axis

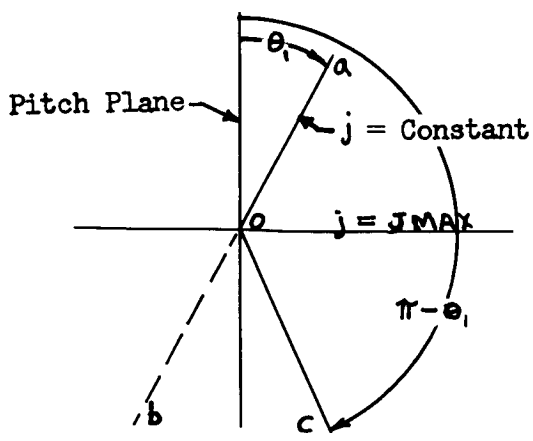

c. Definition of j Coordinate

Figure 19 . Treatment of Radial Distribution of Properties

3. A data point at the origin is always used if an adjacent data point is available. For the variables $\bar{w}$ and ψ the value is zero by definition. For $u, \bar{v}, p, \rho$ and ϕ an unknown constant value is evaluated after the first smoothing by extrapolating from five adjacent points (least square parabolic fit) and averaging the JMAX values obtained. On subsequent smoothings, since a point will now exist at the origin, an extrapolation is not necessary and the JMAX smoothed values are averaged.

4. If one or more successive data points are missing, the least square fit is not allowed to span the gap between the adjacent sets of data.

5. At the end of an array end point formulas are used. This means effectively that the last three points of the array are all moved to their corresponding values on the same least square parabola.

6. If fewer than five data points exist in a set, the points are left unaltered.

Thus not only are the data smoothed consistent with symmetry about the pitch plane, but the values of the θ-derivatives of the properties at the origin are zero as required.

The numerical procedure used in the program, while following the above principles, fits a parabola to five points using the following definition of variables. Consider that the property Y is to be smoothed versus the variable X. A simple translation is performed such that properties and X-values are plotted relative to the center point in a set of five as illustrated in Figure 20.

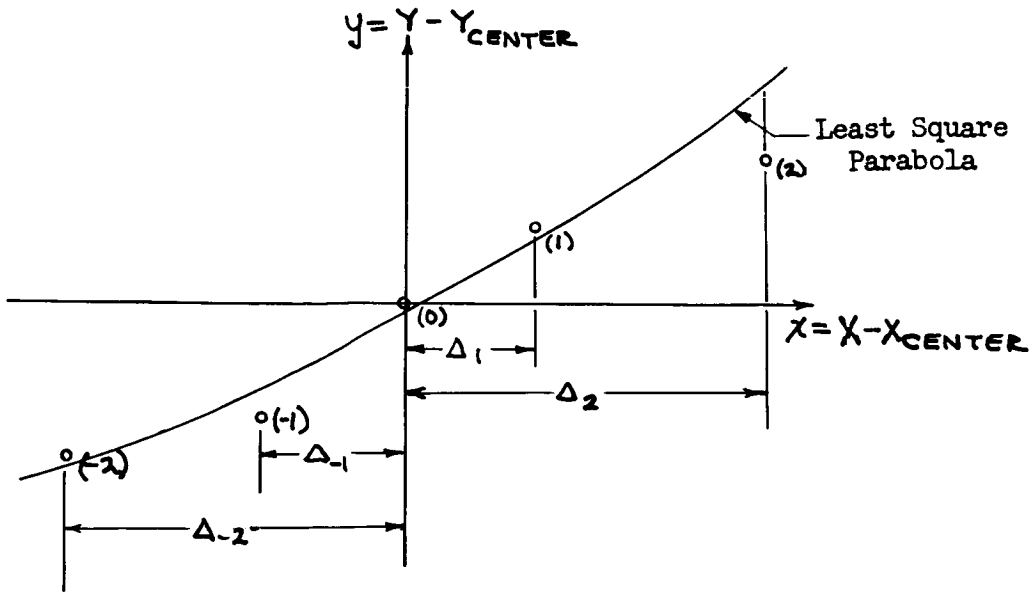

Figure 20 . Least Square Smoothing Parabola

The equation of the least square parabola is

$$y = a + bx + cx^2 \tag{149}$$

An arbitrary spacing of points is allowed. Following the approach given in Reference 21, the following three equations are used to compute the three coefficients of the parabola.

$$(a+b\Delta_{-2}+c\Delta_{-2}^2-y_{-2})+(a+b\Delta_{-1}+c\Delta_{-1}^2-y_{-1})+a+(a+b\Delta_1+c\Delta_1^2-y_1)$$
$$+(a+b\Delta_2+c\Delta_2^2-y_2)=0$$

$$\Delta_{-2}(a+b\Delta_{-2}+c\Delta_{-2}^2-y_{-2})+\Delta_{-1}(a+b\Delta_{-1}+c\Delta_{-1}^2-y_{-1})+\Delta_1(a+b\Delta_1+c\Delta_1^2-y_1)$$
$$+\Delta_2(a+b\Delta_2+c\Delta_2^2-y_2)=0$$

$$\Delta_{-2}^2(a+b\Delta_{-2}+c\Delta_{-2}^2-y_{-2})+\Delta_{-1}^2(a+b\Delta_{-1}+c\Delta_{-1}^2-y_{-1})+\Delta_1^2(a+b\Delta_1+c\Delta_1^2-y_1)$$
$$+\Delta_2^2(a+b\Delta_2+c\Delta_2^2-y_2)=0$$

or

$$5a+b(\Delta_{-1}+\Delta_{-2}+\Delta_1+\Delta_2)+c(\Delta_{-2}^2+\Delta_{-1}^2+\Delta_1^2+\Delta_2^2)$$
$$+(-y_{-2}-y_{-1}-y_1-y_2)=0$$

$$a(\Delta_{-2}+\Delta_{-1}+\Delta_1+\Delta_2)+b(\Delta_{-2}^2+\Delta_{-1}^2+\Delta_1^2+\Delta_2^2)+c(\Delta_{-2}^3+\Delta_{-1}^3+\Delta_1^3+\Delta_2^3)$$
$$+(-\Delta_{-2}y_{-2}-\Delta_{-1}y_{-1}-\Delta_1y_1-\Delta_2y_2)=0$$

$$a(\Delta_{-2}^2+\Delta_{-1}^2+\Delta_1^2+\Delta_2^2)+b(\Delta_{-2}^3+\Delta_{-1}^3+\Delta_1^3+\Delta_2^3)+c(\Delta_{-2}^4+\Delta_{-1}^4+\Delta_1^4+\Delta_2^4)$$
$$+(-\Delta_{-2}^2y_{-2}-\Delta_{-1}^2y_{-1}-\Delta_1^2y_1-\Delta_2^2y_2)=0$$

If we define

$$D \equiv \begin{vmatrix} 5 & L & M \\ L & M & N \\ M & N & P \end{vmatrix}$$

where

$$L \equiv \Delta_{-2} + \Delta_{-1} + \Delta_1 + \Delta_2$$
$$M \equiv \Delta_{-2}^2 + \Delta_{-1}^2 + \Delta_1^2 + \Delta_2^2$$
$$N \equiv \Delta_{-2}^3 + \Delta_{-1}^3 + \Delta_1^3 + \Delta_2^3$$
$$P \equiv \Delta_{-2}^4 + \Delta_{-1}^4 + \Delta_1^4 + \Delta_2^4$$

and if

$$R_1 \equiv y_{-2} + y_{-1} + y_1 + y_2$$
$$R_2 \equiv \Delta_{-2} y_{-2} + \Delta_{-1} y_{-1} + \Delta_1 y_1 + \Delta_2 y_2$$
$$R_3 \equiv \Delta_{-2}^2 y_{-2} + \Delta_{-1}^2 y_{-1} + \Delta_1^2 y_1 + \Delta_2^2 y_2$$

the solution is,

$$a = \frac{\begin{vmatrix} R_1 & L & M \\ R_2 & M & N \\ R_3 & N & P \end{vmatrix}}{D} \tag{150}$$

$$b = \frac{\begin{vmatrix} 5 & R_1 & M \\ L & R_2 & N \\ M & R_3 & P \end{vmatrix}}{D} \tag{151}$$

and

$$c = \frac{\begin{vmatrix} 5 & L & R_1 \\ L & M & R_2 \\ M & N & R_3 \end{vmatrix}}{D} \tag{152}$$

Where the center point formula is used, the corrected or smoothed y value is simply a. For end points the full equation is used to compute the smoothed value.

In the computer program the user may choose the following input parameters,

1. The k value defining the location of the marching plane at which smoothing is initiated.

2. Number of smoothings per plane.

The smoothing is automatically removed from operation when a body intersection has been obtained on the inner grid radius in the meridian plane JMAX.

It has been observed that for capsule body shapes the smoothing can reduce the data accuracy in the flow field near the shoulder. Since smoothing is needed only near the axis, it is desirable to use only a percentage of the indicated correction due to smoothing. This weighting factor is input as a function of radius only and may vary between zero and one. Its radial variation should be a faired curve having its maximum value of one on the x axis.

DATA OUTPUT PROGRAM

The flow field program integrates to determine the properties $u, \bar{v}, \bar{w}, p, \rho, \phi$ and ψ at grid points and at predicted body locations and stores these final results on tape for use by the separate Data Output Program. These data can also be printed out by the flow field program if desired. For practical applications the data output program presents the following properties and information,

a. Pressure, atmospheres
b. Density, lb/ft^3
c. Temperature, °R
d. Enthalpy, BTU/lb
e. Entropy, BTU/lb°R
f. Velocity, ft/sec (magnitude and direction)
g. Mach number
h. Perpendicular distance from the body surface to the shock wave
i. Stagnation point location
j. Streamline traces in the plane of symmetry. The user selects the streamlines by specifying the point at which these streamlines cross the shock. The stagnation streamline trace is always determined.
k. The projection on a plane normal to the body axis of symmetry, of the streamline traces along the body surface emanating from the stagnation point at specified angular intervals.

The Data Output Program computes and always presents the above information, with quantities a through h being determined on the body surface at points designated as stations. These stations lie along lines on the body surface emanating at specified angular intervals from the point of intersection of the surface and the axis of symmetry. The program user has the option of choosing the angular interval and the spacing of stations along

the body lines. The spacing is specified in terms of curvilinear distance measured along the surface for the Apollo shape; for the general body shape the spacing is specified in terms of the radius, r_s , measured from the axis of symmetry.

In addition to these data quantities a through g are also presented for the shock layer according to the following three options, any combination of which may be selected.

Option A

Data are presented for the region between the body and the shock along lines perpendicular to the body at each station. Along each of these lines a minimum number of five equally spaced data points including the body and shock points will be obtained. The user has the option of choosing the number of points up to a maximum of ten.

Option B

Quantities a through g are obtained at specified intervals along any or all of the streamline traces defined in j and k above.

Option C

For each station, data are obtained in a field bounded by the shock wave and the plane tangent to the body at the station. Points in this field are located by a cylindrical coordinate system (r', θ', x') with its origin at the station and the centerline of the cylinder (x' axis) normal to the body. The angular coordinate is measured from the plane containing the body data line and the axis of symmetry of the body.

The operation of the Data Output Program may be functionally represented by the following block diagram.

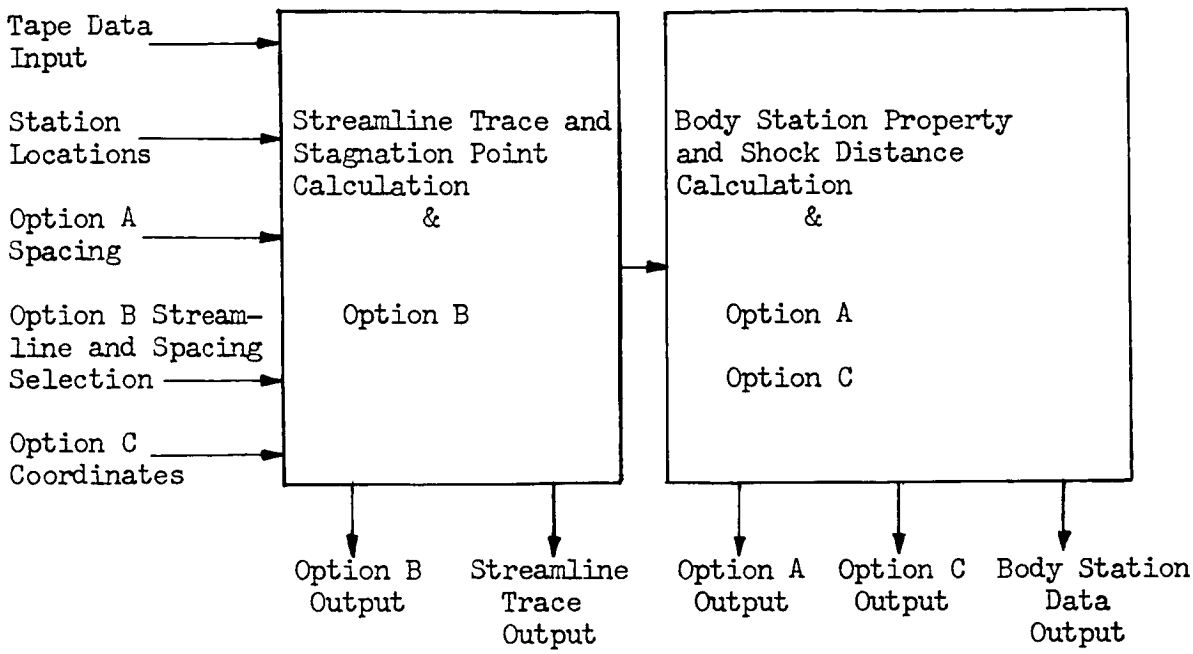

Figure 21. Block Diagram of Data Output Program

The calculation of the output data in Options A and C is closely related to the body station property and shock distance calculations, and they will be discussed together in the following text. Similarly, the calculation of the output data in Option B is closely related to the streamline trace calculation and they will, therefore, also be discussed together.

Body Station Property Calculation and Options A and C

The object of the body station property calculation and data Options A and C is to obtain properties in the flow field at various points in the shock layer other than the grid points (i, j, k). In Option A the properties are calculated at equally spaced points along a normal to the body at a given location or station, designated by r_s and θ_s. In Option C, the normal to the body becomes the x' axis of a localized cylindrical coordinate system, the origin being on the body, θ's being measured with respect to a meridian plane of the body passing through the x' axis, and r's being measured perpendicular to this x' axis. Thus, each data point associated with a given station can be designated by an x', r' and θ' after the r_s and θ_s of the station are known. It is seen that Option A is merely a simplified form of Option C with $r' = 0$ and the x' axis divided up equally between the body and the shock wave.

The coordinates of the stations for Apollo are input in terms of L_s, the geodesic from the body origin point to the station, rather than the r_s which is needed for interpolation between grid points. A relationship between

L and r can easily be found. The differential arc length dL along the body data line is related to its components in a cylindrical coordinate system as follows,

$$(dL)^2 = (dx)^2 + (dr)^2$$

or

$$L = \int_0^r \sqrt{1 + \left(\frac{dx}{dr}\right)^2}\, dr$$

The equation of any given translated circle of radius R is,

$$x = -\sqrt{R^2 - (r - r_T)^2} + x_T$$

where r_T and x_T represent the distances between the center of the circle and the r and x axes respectively.

Then;

$$\frac{dx}{dr} = \frac{r - r_T}{\sqrt{R^2 - (r - r_T)^2}}$$

and

$$L = \int_{r_T}^{r} \frac{R\, dr}{\sqrt{(R^2 - r_T^2) - r^2 + 2 r_T r}}$$

$$= R \sin^{-1}\left(\frac{r - r_T}{R}\right)$$

or

$$r_s = R \sin\left(\frac{L_s}{R}\right) + r_T$$

For segment 1 of Apollo, $r_T = 0$, $R = R_{H_1}$, (see Figure 17) and

$$r_S = R_{H_1} \sin\left(\frac{L_S}{R_{H_1}}\right)$$

For the second segment

$$r_T = \left(\frac{d}{2} - R_{H_2}\right)$$

The start of the second segment, the beginning of the shoulder, is at

$$r_{SH} = R_{H_1} \sin \phi = R_{H_1}\left(\frac{\frac{d}{2} - R_{H_2}}{R_{H_1} - R_{H_2}}\right)$$

Therefore at the start of the second segment, the beginning of the shoulder,

$$L_{SH} = R_{H_1} \sin^{-1}\left(\frac{\frac{d}{2} - R_{H_2}}{R_{H_1} - R_{H_2}}\right) = R_{H_1}\phi$$

In the second segment

$$L_S = R_{H_2} \sin^{-1}\left(\frac{r_S - r_T}{R_{H_2}}\right) - R_{H_2}\phi + L_{SH}$$

So, now solving for r_S and substituting for r_T, ϕ and L_{SH},

$$r_S = R_{H_2}\left[\sin\left(\frac{L_S + (R_{H_2} - R_{H_1}) \sin^{-1}\left(\frac{\frac{d}{2} - R_{H_2}}{R_{H_1} - R_{H_2}}\right)}{R_{H_2}}\right) - 1\right] + \frac{d}{2}$$

which is the expression for r_S in the second segment ($L_S > L_{SH}$).

After the complete flow field and body have been obtained, with or without shock convergence, the data output options may be used. It is necessary for the interpolations that the geometric relationship between the body and the shock coordinate systems be known. It is to be assumed that the final predicted body as determined by the shock wave, and the desired body as eventually determined by the input equations are sufficiently close so that the normals and localized coordinate systems may be oriented with respect to the desired body which is fixed in the shock coordinate system by the translation point, defined in Figure 14 . After the desired body is translated to its final position, and the body equations are expressed in the shock-oriented system. A normal to the body may be erected having the following equation, which is obtained from a generalization of Equation (123).

$$r = -\left(\frac{dx_s}{dr}\right)_s x_s + \left(r_s + \left(\frac{dx_s}{dr}\right)_s x_s\right)$$

or

$$r = a_n x_s + b_n \tag{153}$$

At this point in order to determine the absolute coordinates of the points of Option A, it is necessary to introduce interpolation constants C_r, C_θ, C_x which represent the fractional coordinates of a data point between the bounding i's, j's, or k's, shown in Figure 22 .

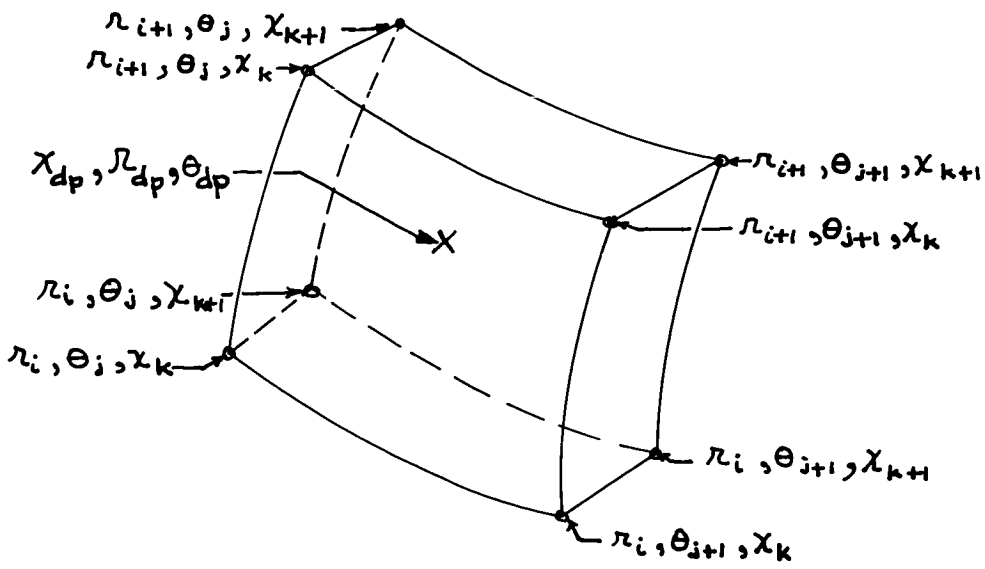

Figure 22 . Bounding Grid Points for Data Interpolation

For Option A the θ_{dp} of any data point is equal to the θ_s of the station. The θ_j's of the grid system are given in terms of $0° < \theta < 90°$ for the first quadrant and due to the way the j's are defined, $\theta_j = \pi - \theta_j$ in the second quadrant. Thus the θ_j's bounding the θ_s can be found and C_{θ_s} may now be defined as

$$C_{\theta_s} \equiv \frac{\theta_s - \theta_j}{\theta_{j+1} - \theta_j}$$

The absolute coordinates of the data points for Option C are not yet known and will be found later.

The shock surface is represented by a series of points, $S_{i,j}$, as computed by the main program. The shock surface as interpolated in a plane θ_s of Option A is given by

$$S_{i,\theta_s} = S_{i,j} + \left(\frac{\theta_s - \theta_j}{\theta_{j+1} - \theta_j}\right)\left(S_{i,j+1} - S_{i,j}\right)$$

$$= S_{i,j}\left(1 - C_{\theta_s}\right) + C_{\theta_s} S_{i,j+1}$$

where j and $j+1$ represent the j's bounding θ_s.

Joining the shock points by line segments, the equation of any segment at a given i and adjacent $i2$ is

$$r_{SH} = \frac{\left(r_{i2} - r_i\right) x}{S_{i2,\theta_s} - S_{i,\theta_s}} + \left[r_i - \left(\frac{r_{i2} - r_i}{S_{i2,\theta_s} - S_{i,\theta_s}}\right) S_{i,\theta_s}\right]$$

or

$$r_{SH} = a_{SH} x + b_{SH} \tag{154}$$

After searching for the correct segment which the normal intersects, the simultaneous solution of Equations (153) and (154) can be found yielding

$$x_i = \frac{b_{SH} - b_n}{a_n - a_{SH}}$$

$$r_i = a_{SH}\left(\frac{b_{SH} - b_n}{a_n - a_{SH}}\right) + b_{SH}$$

The distance between the body and the shock wave along the normal becomes

$$\sqrt{(x_i - x_s)^2 + (r_i - r_s)^2}$$

If θ_n = angle between the normal and x_s axis, then

$$\text{TAN } \theta_n = a_n$$

$$\text{SIN } \theta_n = \frac{a_n}{\sqrt{1 + a_n^2}}$$

$$\cos \theta_n = \frac{1}{\sqrt{1 + a_n^2}}$$

Now, the coordinates of each of the m data points can be found:

$$r_{dp} = r_s - \left(\sqrt{(x_i - x_s)^2 + (r_i - r_s)^2}\right)\left(\frac{a_n}{\sqrt{1 + a_n^2}}\right)\left(\frac{p-1}{m-1}\right) \qquad (155a)$$

$$p = 1, m$$

and

$$x_{dp} = \frac{r_{DATA} - b_n}{a_n} = x_s - \left(\sqrt{(x_i - x_s)^2 + (r_i - r_s)^2}\right)\left(\frac{1}{\sqrt{1 + a_n^2}}\right)\left(\frac{p-1}{m-1}\right) \qquad (155b)$$

$$p = 1, m$$

For Option C each of the points must now be put into the absolute coordinate system. Let r', x', θ' be the coordinates in the localized system and r, x and θ be the coordinates in the absolute shock oriented system. The transformation can be made by finding the vector $\vec{R}$ in cartesian coordinates. $\vec{R}$, shown in Figure 23, is a vector from the origin of the absolute system origin to the given data point. $\vec{R}$ is made up of three components,

$$\vec{R} = \vec{r}_1 + \vec{r}_2 + \vec{r}_3$$

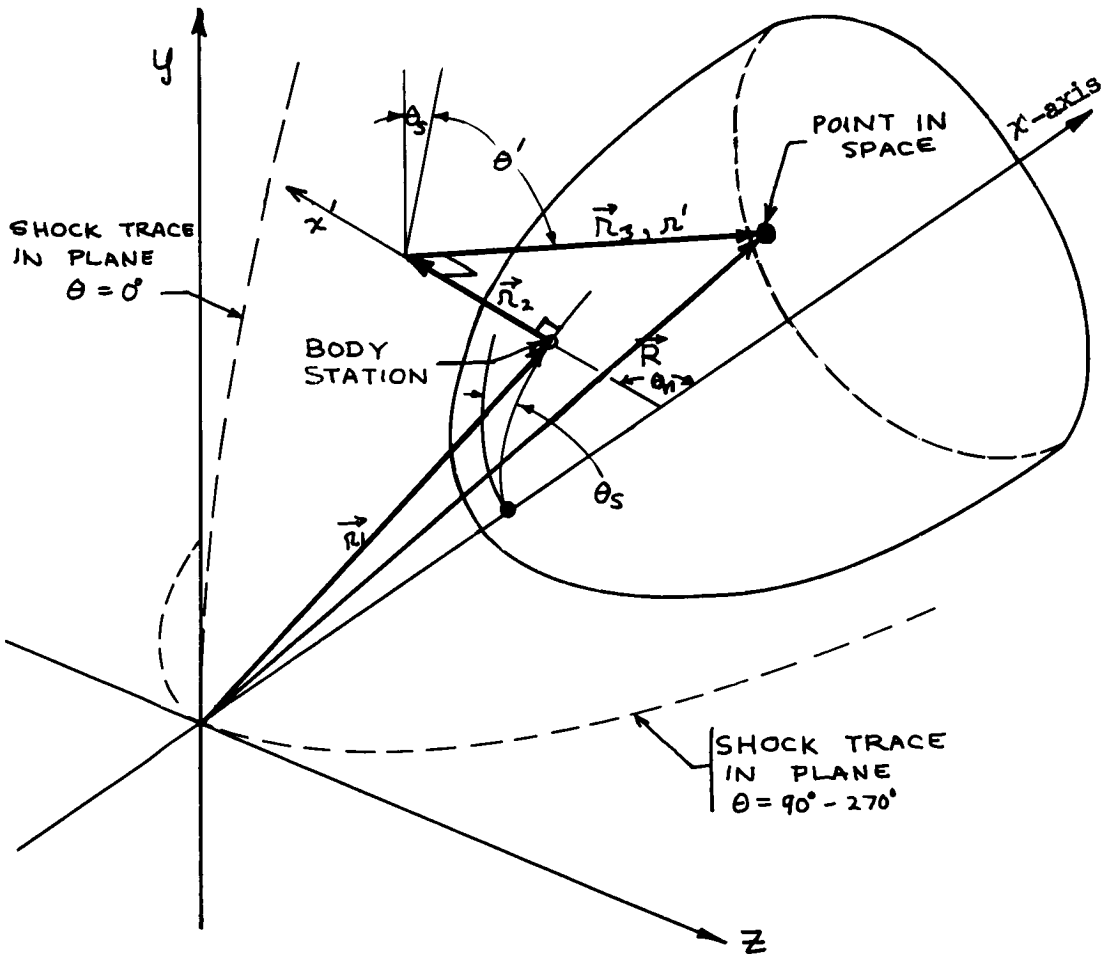

Figure 23. Relative Coordinate System

where

$\vec{r}_1$ = vector from the shock origin to the point on the body (x_s, r_s) from which the normal is erected. This vector lies in a plane inclined at an angle θ_s with respect to the pitch plane.

$\vec{r}_2$ = vector from the tip of $\vec{r}_1$ to the point at which r' is erected. This vector is coincident with the x' axis, lies in a plane inclined at an angle θ_s with respect to the pitch plane, and is inclined at an angle θ_n to the x axis as measured in the θ_s plane.

$\vec{r}_3$ = r' which is perpendicular to the x' axis, inclined at an angle θ' as measured in a plane perpendicular to x' from the original θ_s inclined plane which contains the x' axis. $\vec{r}_1$, $\vec{r}_2$ and $\vec{r}_3$ are described graphically in Figure 24.

Now, finding the components of each of these vectors, if $\vec{i}$, $\vec{j}$ and $\vec{k}$ represent unit vectors in the absolute cartesian system,

$$\vec{R} = \left[x_s \vec{i} + r_s \cos\theta_s \vec{j} + r_s \sin\theta_s \vec{k} \right]$$
$$+ \left[-\frac{x'}{\sqrt{1+a_n^2}} \vec{i} - \frac{a_n \cos\theta_s x'}{\sqrt{1+a_n^2}} \vec{j} - \frac{a_n \sin\theta_s x'}{\sqrt{1+a_n^2}} \vec{k} \right]$$
$$+ \left[-\frac{a_n r' \cos\theta'}{\sqrt{1+a_n^2}} \vec{i} + \left(\frac{r' \cos\theta_s \cos\theta'}{\sqrt{1+a_n^2}} - r' \sin\theta_s \sin\theta' \right) \vec{j} \right.$$
$$\left. + \left(r' \cos\theta_s \sin\theta' + \frac{r' \sin\theta_s \cos\theta'}{\sqrt{1+a_n^2}} \right) \vec{k} \right]$$

$$= R_x \vec{i} + R_y \vec{j} + R_z \vec{k}$$

$$= \left[x_s - \frac{x'}{\sqrt{1+a_n^2}} - \frac{a_n r' \cos\theta'}{\sqrt{1+a_n^2}} \right] \vec{i}$$
$$+ \left[r_s \cos\theta_s - \frac{a_n \cos\theta_s x'}{\sqrt{1+a_n^2}} + \frac{r' \cos\theta_s \cos\theta'}{\sqrt{1+a_n^2}} - r' \sin\theta_s \sin\theta' \right] \vec{j}$$
$$+ \left[r_s \sin\theta_s - \frac{a_n \sin\theta_s x'}{\sqrt{1+a_n^2}} + r' \cos\theta_s \sin\theta' + \frac{r' \sin\theta_s \cos\theta'}{\sqrt{1+a_n^2}} \right] \vec{k}$$

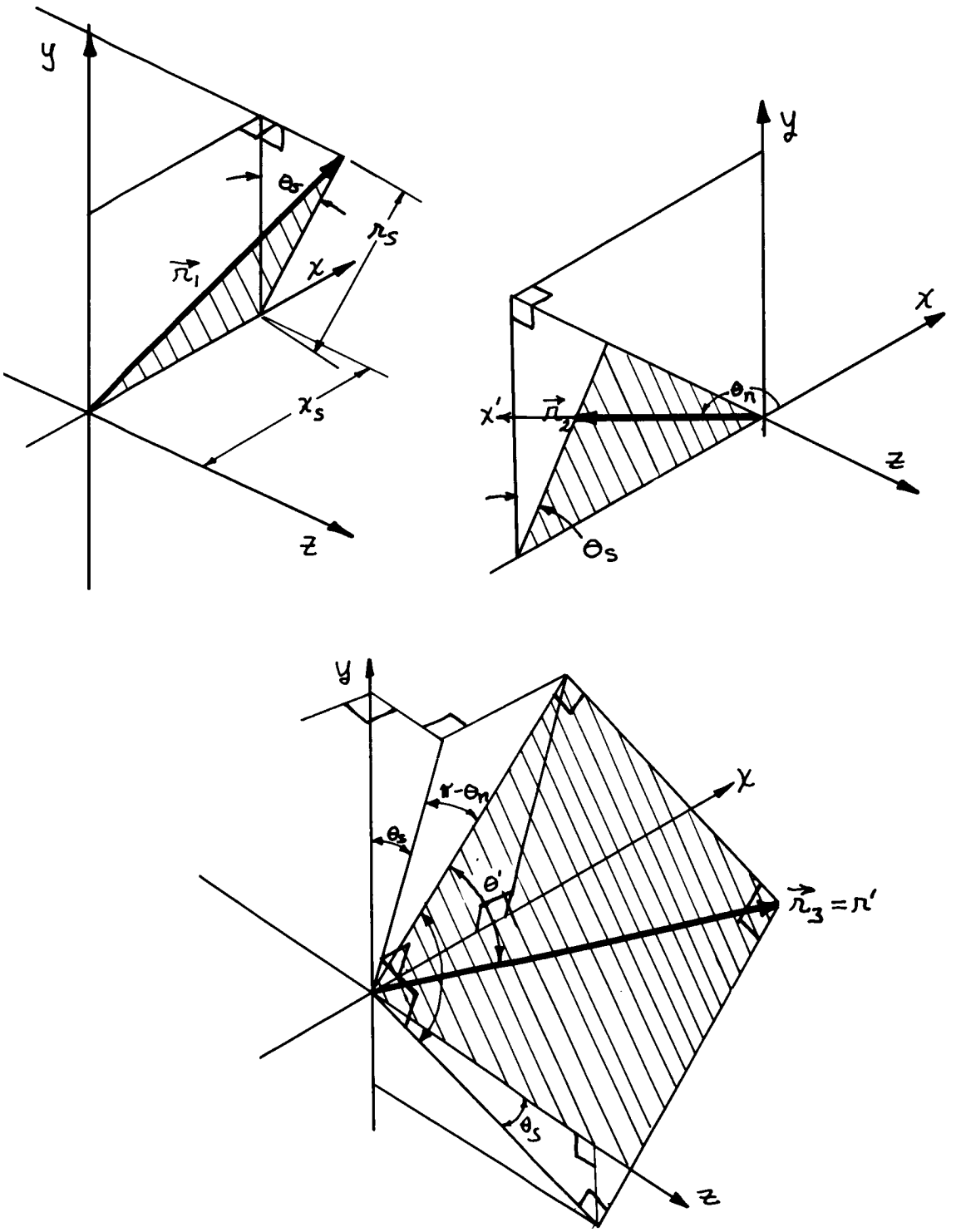

Figure 24 . Vector Relationships in Coordinate Transformation

Now, converting back into the cylindrical coordinates of the shock system,

$$x_{DATA} = R_x$$

$$= x_s - \frac{x'}{\sqrt{1+a_n^2}} - \frac{a_n r' \cos\theta'}{\sqrt{1+a_n^2}} \tag{156}$$

$$r_{DATA} = \sqrt{R_y^2 + R_z^2}$$

$$= \left[\left(r_s \cos\theta_s - \frac{a_n \cos\theta_s x'}{\sqrt{1+a_n^2}} + \frac{r' \cos\theta_s \cos\theta'}{\sqrt{1+a_n^2}} - r' \sin\theta_s \sin\theta'\right)^2 + \left(r_s \sin\theta_s - \frac{a_n \sin\theta_s x'}{\sqrt{1+a_n^2}} + r' \cos\theta_s \sin\theta' + \frac{r' \sin\theta_s \cos\theta'}{\sqrt{1+a_n^2}}\right)^2\right]^{1/2} \tag{157}$$

and

$$\theta_{DATA} = \tan^{-1}\left(\frac{R_y}{R_z}\right)$$

$$= \tan^{-1}\left[\left(r_s \cos\theta_s - \frac{a_n \cos\theta_s x'}{\sqrt{1+a_n^2}} + \frac{r' \cos\theta_s \cos\theta'}{\sqrt{1+a_n^2}} - r' \sin\theta_s \sin\theta'\right) \Big/ \left(r_s \sin\theta_s - \frac{a_n \sin\theta_s x'}{\sqrt{1+a_n^2}} + r' \cos\theta_s \sin\theta' + \frac{r' \sin\theta_s \cos\theta'}{\sqrt{1+a_n^2}}\right)\right] \tag{158}$$

These equations for Option C data points reduce to those of Option A, Equations (155), if $r' = 0$ and χ' is appropriately defined.

At this point since the absolute coordinates of all the data points for Options A and C are known, the $C_{\theta_{dp}}$'s for Option C and the $C_{r_{dp}}$'s and $C_{\chi_{dp}}$'s for Options A and C may now be found. Knowing the θ_{dp}'s, the θ_j's and θ_{j+1}'s bounding the θ_{dp}'s can be found and

$$C_{\theta_{dp}} = \frac{\theta_{dp} - \theta_j}{\theta_{j+1} - \theta_j} \tag{159a}$$

for the data points of Option C. Similarly, the bounding r_i's for all the data points can be found and

$$C_{r_{dp}} = \frac{r_{dp} - r_i}{r_{i+1} - r_i} \tag{159b}$$

The bounding k's of a data point, shown in Figure 25, are not so easily found since the χ value of a k is also a function of r and θ.

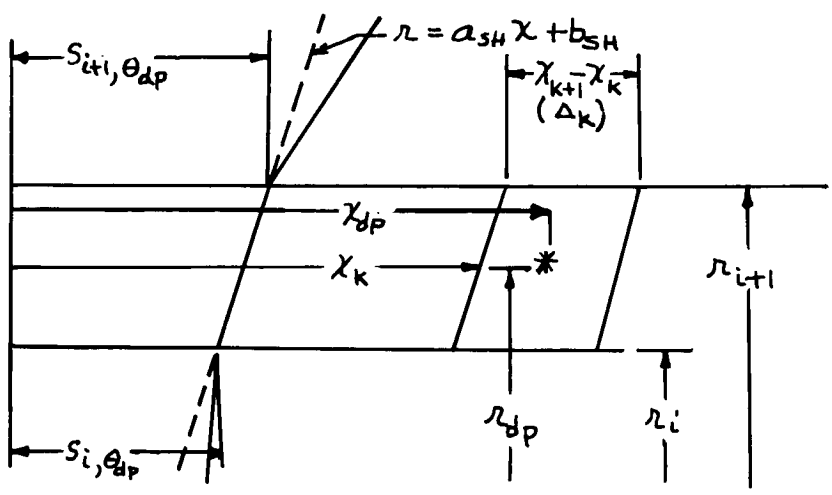

Figure 25. Bounding k's and C_χ

For each data point of Option C, as in Equation

The equation of a k plane, which is parallel to the $S_{i,\theta_{dp}}$ surface, is

$$r = a_{SH}\,x + \left[r_i - a_{SH}\left(S_{i,\theta_{dp}} + \sum_{0}^{k-1} \Delta_i\right)\right] \tag{160}$$

where

a_{SH} is defined by Equation (154)

Δ_i = integration step size, the distance between k and $k+1$ planes, $\Delta_0 = 0$.

If i is the i of the smallest bounding r_i of the data point then letting $r = r_{dp}$ in Equation (160), tests can be made for the bounding k's by testing against

$$x_k = \frac{r_{dp} - \left[r_i - a_{SH}\left(S_{i,\theta_{dp}} + \sum_{0}^{k-1} \Delta_i\right)\right]}{a_{SH}}$$

or, after substituting for a_{SH} from Equation (154) and reducing

$$x_k = S_{i,\theta_{dp}}\left(1 - c_{r_{dp}}\right) + c_{r_{dp}}\left(S_{i+1,\theta_{dp}}\right) + \sum_{0}^{k-1} \Delta_i \tag{161}$$

Once the bounding k's are found, such that

$$x_k < x_{dp} < x_{k+1}$$

then

$$c_{x_{dp}} = \frac{x_{dp} - x_k}{x_{k+1} - x_k}$$

$$= \frac{x_{dp} - \left[S_{i,\theta_{dp}}\left(1 - c_{r_{dp}}\right) + c_{r_{dp}} S_{i+1,\theta_{dp}} + \sum_{0}^{k-1} \Delta_i\right.}{\Delta_k} \tag{162}$$

Now there is enough information available to interpolate for the properties at the various data points. With each data point there is associated a $C_{x_{dp}}$, $C_{r_{dp}}$, $C_{\theta_{dp}}$ and eight bounding grid points at which all the flow properties are known. However, it has been found that after the body is reached flow gradients become extremely nonlinear which would indicate that any linear interpolation involving a grid point within the body is likely to be highly inaccurate. The properties at each body point found on a given i and j are computed by the main program. In order to maintain consistency with the main data output logic each bounding grid point shown in Figure 26 lying within the body will use properties found by linearly extrapolating from the properties at the body point at that i, j and the grid point at the first k outside the body at that i and j. This should allow any subsequent interpolations and previous computations to remain unaltered and is consistent with the assumption of linearity in the x, θ and r directions.

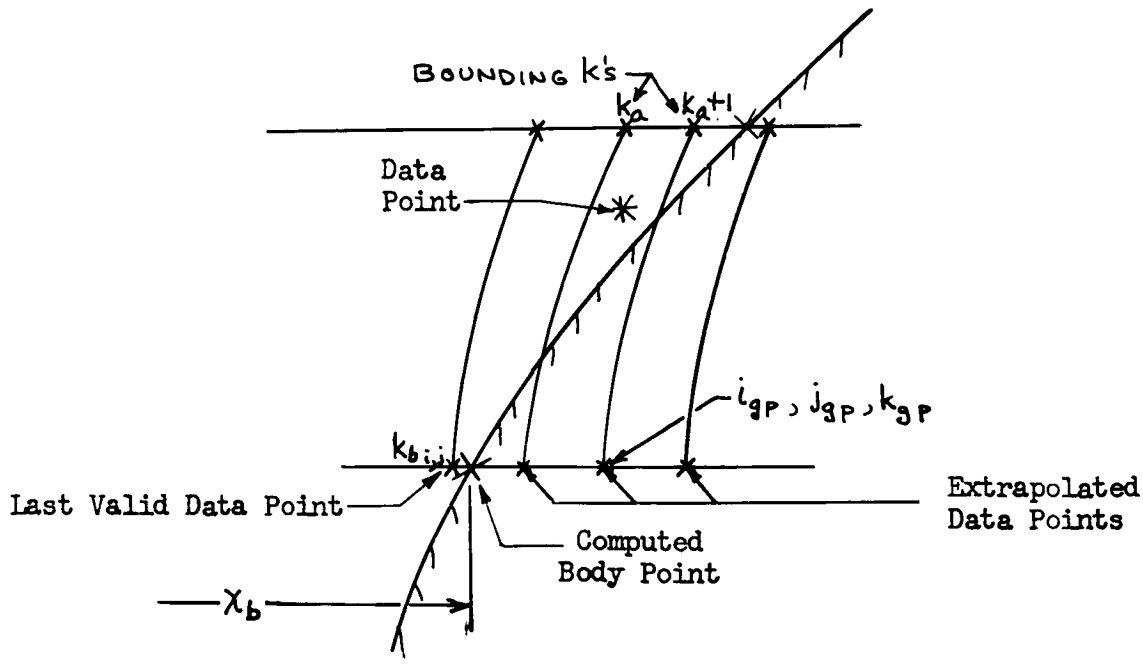

Figure 26. Bounding Grid Point Within Body

The bounding i's, j's and k's of the data point are known as well as the k preceding the body point at any i and j where a body point exists. Let these k's be denoted by k_a, k_a+1 and $k_{b_{i,j}}$ respectively. If for any bounding grid point of a data point $k_a > k_{b_{i,j}}$ for the k_ath plane bounding grid points or $(k_a+1) > k_{b_{i,j}}$ for the (k_a+1)th plane bounding grid points (assuming a body point does exist at the i, j in question), then the properties at that grid point must be replaced by extrapolation. Let the k of the bounding grid point in question be designated k_{gp} whether $k_{gp} = k_a$ or k_a+1. Then, letting i_{gp} and j_{gp} be the i and j of the grid point, finding x_{k_b} at i_{gp} j_{gp} from Equation (161), and assuming Q to represent a general property,

$$Q_{i_{gp},j_{gp},k_{gp}} = Q_{i_{gp},j_{gp},k_b} + \left[\frac{Q_{b_{i_{gp},j_{gp}}} - Q_{i_{gp},j_{gp},k_b}}{\chi_{b_{i_{gp},j_{gp}}} - \chi_{k_b}}\right] \cdot \left(k_{gp} - k_b\right) \sum_{i=k_b}^{(k_{gp}-1)} \Delta_i \tag{163}$$

where

$Q_{i_{gp},j_{gp},k_{gp}}$ represents the extrapolated property which replaces the property currently at i_{gp}, j_{gp} and k_{gp}.

$Q_{b_{i_{gp},j_{gp}}}$ ..... is the body property at that i_{gp} and j_{gp} (assuming a body point is defined at that i_{gp} and j_{gp}).

$\chi_{b_{i_{gp},j_{gp}}}$ ..... is the χ coordinate in the shock system of the body point (computed in the main program)

Δ_i ..... is the integration step size used to reach the $(i+1)$st plane from the ith plane.

There are times when the body point is computed at a given i_{gp} and j_{gp} by extrapolating across a number of k planes. When this occurs the properties at the intermediate grid points are determined by linearly interpolating between those at the body point and the last computed grid point. Equation (163) accomplishes this if k_b is defined to be the k of the last computed grid point, and k_{gp} and $Q_{i_{gp},j_{gp},k_{gp}}$ refer to an intermediate point.

Assume i, j, k represent the lowest i, j and k of the bounding grid points of a given data point. Then if Q represents a given property, interpolation in the θ direction gives

$$Q_{i,\theta_{dp},k} = Q_{i,j,k}\left(1 - C_{\theta_{dp}}\right) + C_{\theta_{dp}} Q_{i,j+1,k} \tag{164a}$$

$$Q_{i+1,\theta_{dp},k} = Q_{i+1,j,k}\left(1 - C_{\theta_{dp}}\right) + C_{\theta_{dp}} Q_{i+1,j+1,k} \tag{164b}$$

$$Q_{i,\theta_{dp},k+1} = Q_{i,j,k+1}\left(1 - C_{\theta_{dp}}\right) + C_{\theta_{dp}} Q_{i,j+1,k+1} \tag{164c}$$

$$Q_{i+1,\theta_{dp},k+1} = Q_{i+1,j,k+1}\left(1 - C_{\theta_{dp}}\right) + C_{\theta_{dp}} Q_{i+1,j+1,k+1} \tag{164d}$$

where for Option A the above calculations are valid for each data point in a given station since $\theta_{dp} = \theta_s$ and $C_{\theta_{dp}} = C_{\theta_s}$.

Now interpolating in the χ direction and substituting the values calculated by Equations (164)

$$Q_{i,\theta_{dp},\chi_{dp}} = Q_{i,\theta_{dp},k}\left(1 - C_{\chi_{dp}}\right) + C_{\chi_{dp}} Q_{i,\theta_{dp},k+1} \tag{165a}$$

$$Q_{i+1,\theta_{dp},\chi_{dp}} = Q_{i+1,\theta_{dp},k}\left(1 - C_{\chi_{dp}}\right) + C_{\chi_{dp}} Q_{i+1,\theta_{dp},k+1} \tag{165b}$$

and finally, interpolating in the r direction and using the results of Equations (165),

$$Q_{r_{dp},\theta_{dp},\chi_{dp}} = Q_{i,\theta_{dp},\chi_{dp}}\left(1 - C_{r_{dp}}\right) + C_{r_{dp}} Q_{i+1,\theta_{dp},\chi_{dp}} \tag{166}$$

which represents the interpolated property at the data point.

Streamline Trace Calculation and Option B

The mandatory data calculated by this procedure includes the stagnation point location, streamline traces in the pitch plane and streamline traces along the body surface emanating from the stagnation point. The stagnation streamline trace will always be computed. When the option is selected the various thermodynamic properties are computed along these traces.

In the pitch plane $\psi = 0$ but the streamlines are labeled by finite values of ϕ.

The r's at which various streamlines cross the shock wave in the pitch plane will be input data, r_{in}. The ϕ at that point on the shock is found by linear interpolation using the $\phi_{i,j,k}$'s which are computed by the main program. In the pitch plane $j=1$, $\phi = \phi(i,k)$ and if r_i and r_{i+1} are the r's bounding a given r_{in};

$$\phi_{TRACE} = \phi_{i,1} + \frac{(r_{in} - r_i)(\phi_{i+1,1} - \phi_{i,1})}{(r_{i+1} - r_i)} \tag{167}$$

Once the value of ϕ to be traced is known, a search for this ϕ must be made in the box shown in Figure 27 (bounded by r_i's and k planes) which the streamline has just entered.

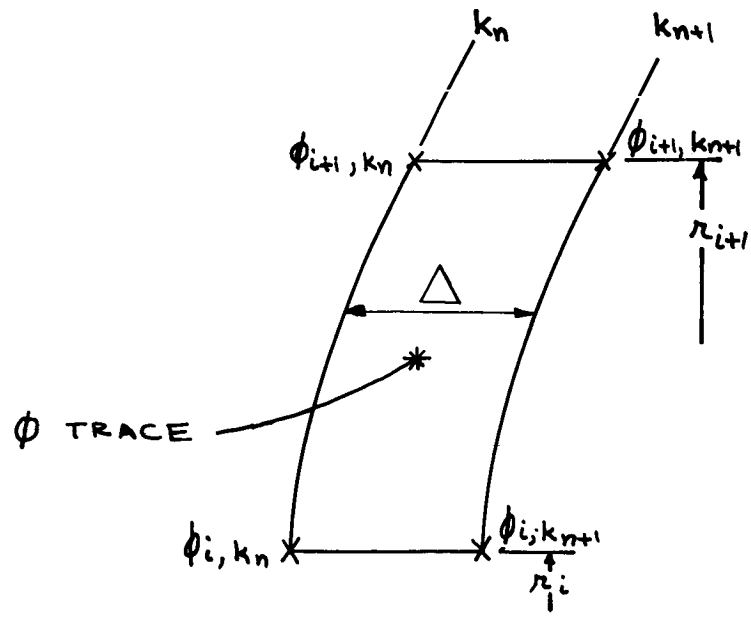

Figure 27. Bounding Grid Points for Streamlines in Pitch Plane

This search is made by testing whether

$$\left| \frac{\phi_{TRACE} - \phi_{i+1,k_n}}{\phi_{i+1,k_{n+1}} - \phi_{i+1,k_n}} \right| < 1 \tag{168}$$

or

$$\left| \frac{\phi_{TRACE} - \phi_{i,k_n}}{\phi_{i,k_{n+1}} - \phi_{i,k_n}} \right| < 1 \tag{169}$$

or

$$\left| \frac{\phi_{TRACE} - \phi_{i,k_{n+1}}}{\phi_{i+1,k_{n+1}} - \phi_{i,k_{n+1}}} \right| < 1 \tag{170}$$

which would indicate whether the desired value of ϕ_{TRACE} is to be found between the corresponding values of i's or k's. If the streamline enters between the i's or k's indicated above, then of course the tests must only

be made on the remaining two sides. No test is ever made for the fourth side (between r_i and r_{i+1} on the k_n plane), because it is assumed that a streamline will never travel towards the shock wave.

If either (168) or (169) are satisfied, then

$$x_{TRACE} = x_{k_n} + \left(\phi_{TRACE} - \phi_{i+1,k_n}\right)\left(\frac{\Delta}{(\phi_{i+1,k_{n+1}} - \phi_{i+1,k_n})}\right)$$

$$r_{TRACE} = r_{i+1}$$

or

$$x_{TRACE} = x_{k_n} + \left(\phi_{TRACE} - \phi_{i,k_n}\right)\left(\frac{\Delta}{\phi_{i,k_{n+1}} - \phi_{i,k_n}}\right)$$

$$r_{TRACE} = r_i$$

respectively. If (170) is true, then:

$$r_{TRACE} = r_i + \left(\phi_{TRACE} - \phi_{i,k_{n+1}}\right)\left(\frac{r_{i+1} - r_i}{\phi_{i+1,k_{n+1}} - \phi_{i,k_{n+1}}}\right) \quad (171)$$

For the stagnation streamline $\phi_{TRACE} = \phi_{STAG}$. The x_k coordinate is found by Equation (161). Thus the r and x are known. For interpolation the constants C_r and C_x, with $C_\theta = 0$, are calculated from Equations (159) and (162) and used in Equation (172) below where Q is a property:

$$Q_{k_r} = Q_{i,k}\left(1 - C_r\right) + C_r Q_{i+1,k} \quad (172a)$$

or

$$Q_{i_x} = Q_{i,k_n}\left(1 - C_x\right) + C_x Q_{i,k_{n+1}} \quad (172b)$$

The properties are now interpolated for at intersections of the streamlines and r_i's and k planes but may be output **at fixed input** intervals of arc-length or more correctly, segment length.

Given the x's and r's of the streamline trace the distance

$$d_1 = \sqrt{(x_2 - x_1)^2 + (r_2 - r_1)^2}$$

can be compared to the desired distance between output, s, shown in Figure 28. If $s > d_1$ the next d must be computed and so on until,

$$s - \sum_1^n d_i \leq d_{n+1}$$

and then

$$Q(s) = Q_{n+1}\, r_{n+1} + \frac{s - \sum_1^n d_i}{d_{n+1}} \left[Q_{n+2}\, r_{n+2} - Q_{n+1}\, r_{n+1} \right]$$

for each property.

If $s \leq d_1$,

$$Q(s) = Q_1\, r_1 + \frac{s}{d_1} \left(Q_2\, r_2 - Q_1\, r_1 \right)$$

This process can be continued, letting x_1 and r_1 be the x and r where the quantities were last output on the streamline yielding

$$r_1 = r_{n+1} + \frac{\left(s - \sum_1^n d_i\right)}{d_{n+1}} \left(r_{n+2} - r_{n+1} \right)$$

$$x_1 = x_{n+1} + \frac{\left(s - \sum_1^n d_i\right)}{d_{n+1}} \left(x_{n+2} - x_{n+1} \right)$$

where if $d_{n+1} = d_1$, $n = 0$; then $\sum_1^0 d_i \equiv 0$.

The streamline is traced and properties interpolated (if desired) by moving along k planes in this manner until bounding values of ϕ can no longer be found within the defined flow field.

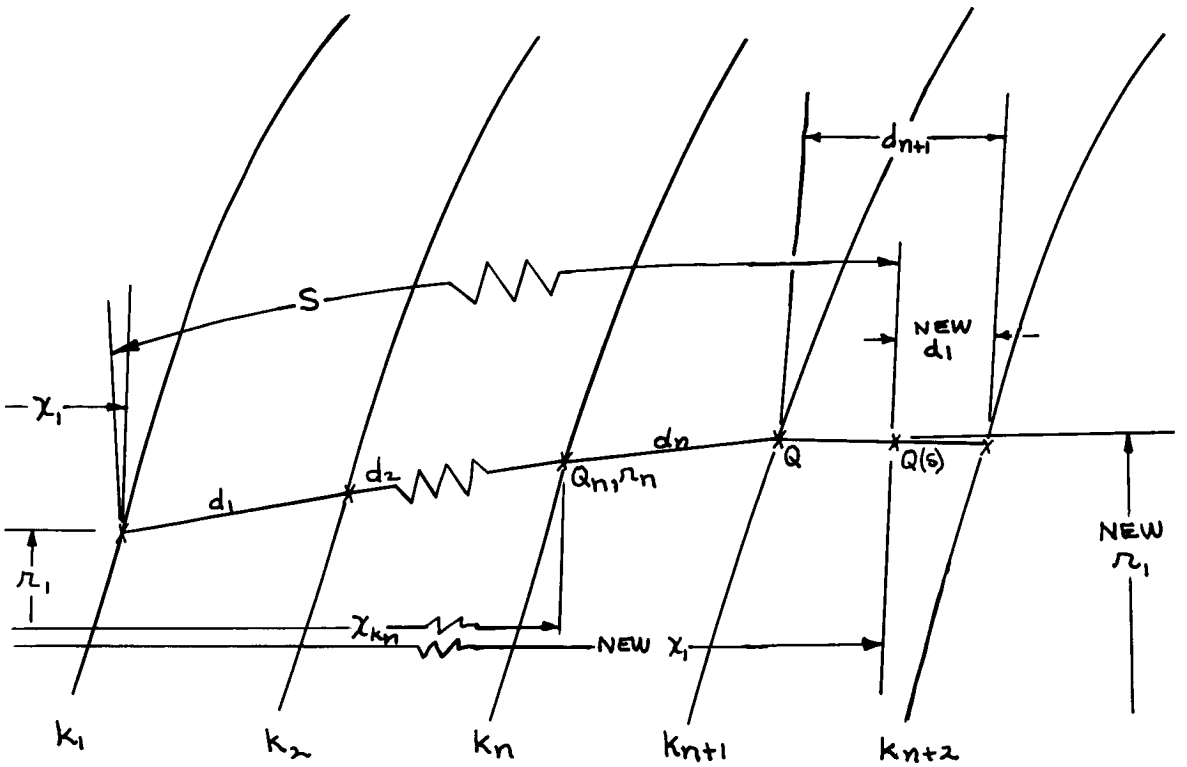

Figure 28. Output at Specified Intervals

The stagnation point location on the body cannot be found from ϕ and ψ since $\phi = \phi_{STAG}$ = constant and $\psi = 0$ everywhere on the body surface. The test for stagnation point is made by finding that point where $\bar{v} = 0$. The bounding r_i's, those at which $\bar{v}$ changes sign, are found by determining where on the pitch plane of the body

$$\left| \bar{v}_{i+1} + \bar{v}_i \right| < \left(\left| \bar{v}_{i+1} \right| + \left| \bar{v}_i \right| \right) \tag{173}$$

Once these bounding r_i's are found, linear interpolation for $\bar{v} = 0$ can be accomplished to compute the r at the stagnation point as defined below:

$$r_{STAG} = r_i - \bar{v}_i \left(\frac{r_{i+1} - r_i}{\bar{v}_{i+1} - v_i} \right) \tag{174}$$

The value of ϕ at the stagnation point, ϕ_{stag}, is also computed by a linear interpolation. ϕ_{stag} is then used to trace the stagnation streamline in the pitch plane.

Traces of streamlines originating at the stagnation point and emanating at various angles with respect to the pitch plane may now be found as shown in Figure 29. In order to facilitate the analysis the streamline traces are not found on the actual body surface but instead on a projection of the body surface on a plane perpendicular to the X axis. A series of concentric circles is to be used for the interpolation of the streamline path based on the criteria that along a given streamline the direction of the velocity vector is always tangent to the path.

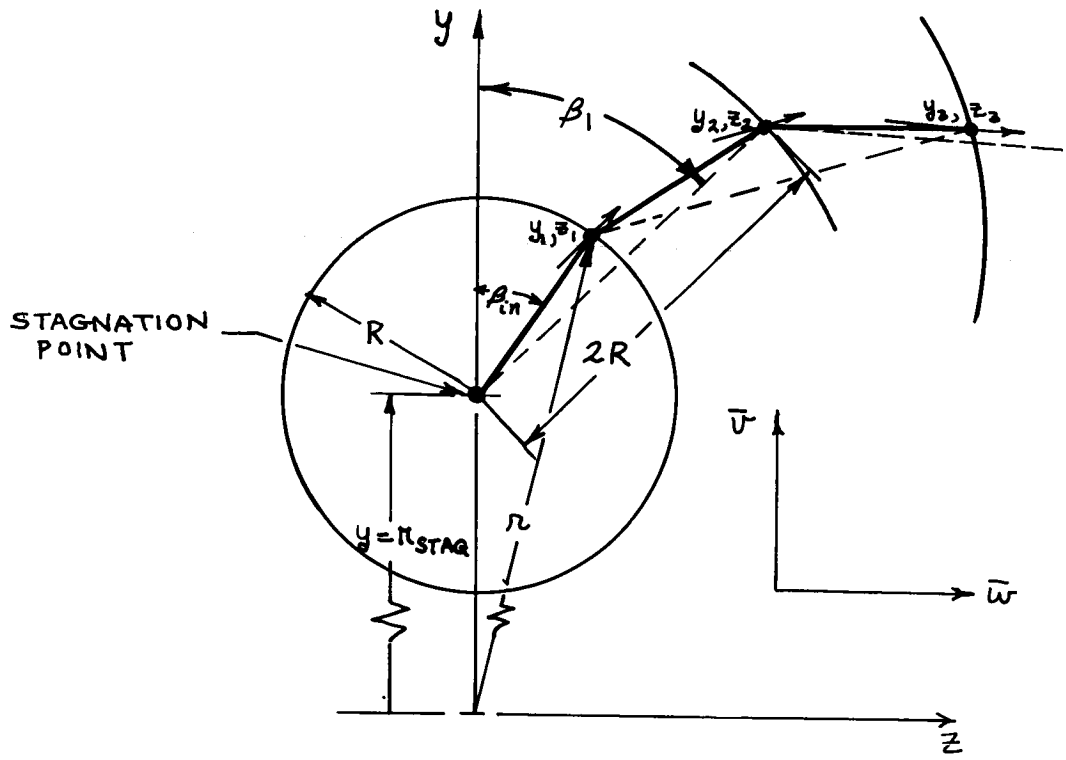

Figure 29. Streamline Trace on a Body Axis Projection

It is convenient to work in a cartesian system, origin at the body axis, and axes perpendicular to the body axis and lying in the pitch and yaw planes (Figure 29).

Some input data designates that a streamline trace will be made on a streamline emanating at an angle β_{in} from the stagnation point. This streamline segment can be represented by the linear equation

$$y = z \, CTN \, \beta_{in} + r_{STAG} \tag{175}$$

Assuming the integration interval to be R, the first point on the trace is at the location,

$$y_1 = R \cos\beta_{in} + r_{STAG}$$
$$z_1 = R \sin\beta_{in}$$

The coordinates of the flow field grid points surrounding this intersection point can now be found by first computing the r and θ of the point in the absolute coordinate system. Knowing y_1, z_1,

$$r = \sqrt{y_1^2 + z_1^2} \tag{176a}$$

$$\theta = \tan^{-1} \frac{z_1}{y_1} \tag{176b}$$

If Option B is elected all the flow field properties must be found at y_1, z_1. Otherwise only $\bar{v}$ and $\bar{w}$ need be found to determine the flow direction at y_1, z_1. The i's and j's of each of the grid points surrounding y_1, z_1 and interpolation constants C_r and C_θ can be determined as outlined previously. Since the properties on the body at each i and j are known, two-dimensional interpolation can be accomplished. If Q is a property, then

$$Q_{i,\theta} = Q_{i,j}\left(1 - C_{\theta_n}\right) + C_{\theta_n} Q_{i,j+1} \tag{177a}$$

$$Q_{i+1,\theta} = Q_{i+1,j}\left(1 - C_{\theta_n}\right) + C_{\theta_n} Q_{i+1,j+1} \tag{177b}$$

and

$$Q_{r,\theta} = Q_{i,\theta}\left(1 - C_{r_n}\right) + C_{r_n} Q_{i+1,\theta} \tag{177c}$$

where i, $i+1$ and j, $j+1$ are the bounding i's and j's respectively. Once the properties have been interpolated for, the second point of the trace must be determined. This is found by going back to $z = 0$, $y = r_{STAG}$, and extending a ray a distance $2R$. The slope of this next segment ($\mathrm{CTN}\,\beta$) is found by using the velocity direction at y_1, z_1 to extend the segment from $z = 0$, $y = r_{STAG}$. The quantities $\bar{v}_1$ and $\bar{w}_1$ were interpolated for through Equations (176) and (177). This new β can now be computed from

$$\beta_1 = \tan^{-1} \frac{\bar{w}_1}{\bar{v}_1} \tag{178}$$

The second point at y_2, z_2 can now be given as

$$y_2 = 2R \cos\beta_1 + r_{STAG}$$
$$z_2 = 2R \sin\beta_1$$

The third point trace is now found by using the velocity direction at y_2, z_2 to extend a line segment from y_1, z_1 a distance $2R$ to y_3, z_3. The new β can now be found from

$$\beta_2 = \tan^{-1} \frac{\bar{w}_2}{\bar{v}_2} \tag{179}$$

The new point is at

$$y_3 = y_1 + 2R \cos\beta_2$$
$$z_3 = z_1 + 2R \sin\beta_2$$

These equations may be generalized to the problem of computing the trace to the nth ring at $y_n, z_n, n \geq 3$.

$$y_n = y_{n-2} + 2R \cos\beta_{n-1}$$
$$z_n = z_{n-2} + 2R \sin\beta_{n-1}$$

defining

$$\beta_{n-1} = \tan^{-1} \frac{\bar{w}_{n-1}}{\bar{v}_{n-1}} \tag{180}$$

Now the properties can be interpolated for at y_n, z_n if so desired.

The new β to extend a segment from the $(n-1)_{ST}$ to $(n+1)_{ST}$ point can be found by Equation (180) after n is increased by one, and this process continues until the streamline goes beyond the defined body points.

After the trace is completed, it is obvious that the distance between points is usually not R. The quantities are, however, output at intervals of R by a method similar to that used in the pitch plane traces.

Computation of Additional Flow Property Data

When the program interpolates or extrapolates for the thermodynamic properties at a given data point, the results consist of values of $u, \bar{v}, \bar{w}$ (ft/sec), p (atmospheres), ρ (lb_m/ft^3), and in some cases for Option B, ϕ, $(lb_m/sec)^{1/2}$, and ψ $(lb_m/sec)^{1/2}$. In addition, for the mandatory output and for Option B it is desired that the thermodynamic properties of temperature T (°R), enthalpy, h (BTU/lb_m), entropy S (BTU/lb_m-°R), total velocity, U (ft/sec), and local Mach number, M be computed. The method of calculation of these quantities depends on whether the flow field is assumed to be composed of a real or perfect gas, except for the total velocity which is always given by

$$U = \sqrt{u^2 + \bar{v}^2 + \bar{w}^2}$$

Real Gas

The properties of a real gas are a function of p and ρ. Gas tables for air which are read into the program allow the following to be obtained directly:

Compressibility Factor .... $z(p, \rho)$

$$\frac{(\text{Enthalpy})\rho}{p} \quad \ldots\ldots \quad h(p,\rho)\frac{\rho}{p}$$

$$\frac{(\text{Entropy})}{R_{SPECIFIC}} \quad \ldots\ldots\ldots \quad s(p,\rho)/R_{SPECIFIC}$$

Defining

$$J = 778.3 \ \frac{ft\text{-}lb}{BTU}$$

$$A = 2116.8 \ \frac{lb_f}{ATM\text{-}ft^2}$$

Then

$$h\left(\frac{BTU}{lb_m}\right) = \left(\frac{h\rho}{p}\right)_{\substack{STATE\\PROGRAM}} \times \frac{p\,(ATM)}{\rho\left(\frac{lb_m}{ft^3}\right)} \times \frac{A}{J}\left(\frac{BTU}{ATM\text{-}ft^3}\right)$$

$$s\left(\frac{BTU}{lb_m\text{-}°R}\right) = \left(\frac{s}{R_{SP.}}\right)_{\substack{STATE\\PROGRAM}} \times R_{SP.}\left(\frac{BTU}{lb_m\text{-}°R}\right)$$

For a real gas

$$R_{SP.}\left(\frac{BTU}{lb_m\text{-}^\circ R}\right) = \frac{1.98588\left(\frac{BTU}{lb\text{-}mole-^\circ R}\right) Z}{28.966\ lb_m/lb\text{-}mole}$$

$$= 0.0685590\ Z\ \left(\frac{BTU}{lb_m\text{-}^\circ R}\right)$$

Now the equation of state allows temperature to be calculated

$$T(^\circ R) = \frac{P\ (ATM)}{\rho\left(\frac{lb_m}{ft^3}\right) R_{SP.}\left(\frac{BTU}{lb_m\text{-}^\circ R}\right)} \times \frac{A}{J}\left(\frac{BTU}{ATM\text{-}ft^3}\right) \qquad (181)$$

Local Mach number

$$M = \frac{U}{a}$$

where a is the local speed of sound. For real equilibrium air, the Mach number may be expressed as

$$M = \frac{U}{\sqrt{\frac{Jg\rho\,(\partial h/\partial \rho)_p}{1-\rho(J/A)(\partial h/\partial p)_\rho}}} \qquad (182)$$

where g = 32.174 ft/sec^2

p = pressure in atmospheres

Perfect Gas

For a perfect gas ($Z = 1$)

$$R_{SP.} = \frac{1.98588}{(MOL.\ WT.)}\left(\frac{BTU}{lb_m\text{-}^\circ R}\right) = 0.0685590\left(\frac{BTU}{lb_m\text{-}^\circ R}\right) \text{ for air.}$$

and from the equation of state

$$T\left({}^{\circ}R\right) = \frac{p\ (ATM)}{\rho\left(\frac{lbm}{ft^3}\right) R_{SP}\left(\frac{BTU}{lb_m\,{}^{\circ}R}\right)} \times \frac{A}{J}\left(\frac{BTU}{ATM\text{-}ft^3}\right)$$

and

$$h = C_p T$$

$$= \left(\frac{C_p}{R_{SP}}\right)\frac{p}{\rho}$$

$$= \frac{\gamma}{\gamma-1}\,\frac{p(ATM)}{\rho\left(\frac{lbm}{ft^3}\right)} \times \frac{A}{J}\left(\frac{BTU}{ATM\text{-}ft^3}\right) \qquad (183)$$

Also

$$\int ds = \int \frac{dh - (1/\rho)dp}{T} = \int \frac{dh}{T} - \int R_{SP}\, dp$$

Substituting for h from Equation (183)

$$\int ds = \int \frac{\gamma}{\gamma-1}\,\frac{d\left(\frac{p}{\rho}\right)}{T} - \int R_{SP.}\,\frac{dp}{p}$$

$$\int ds = \frac{\gamma}{\gamma-1} R_{SP.}\left[\int \frac{dp}{p} - \int \frac{d\rho}{\rho}\right] - R_{SP.}\int \frac{dp}{p}$$

$$\int_{s_\infty}^{s_i} ds = \frac{R_{SP}}{\gamma-1}\left[-\gamma\int_{\rho_\infty}^{\rho_i}\frac{d\rho}{\rho} + \int_{p_\infty}^{p_i}\frac{dp}{p}\right.$$

Defining $s_\infty \equiv 0$, and integrating

$$s_i = \frac{R_{sp.}}{\gamma - 1}\left[\gamma \ln \frac{\rho_\infty}{\rho_i} + \ln \frac{p_i}{p_\infty}\right] \qquad \left(\frac{BTU}{lb_m - {}^\circ R}\right) \tag{184}$$

For a perfect gas, from Equation (183)

$$\left(\frac{\partial h}{\partial \rho}\right)_p = \frac{-\gamma}{\gamma - 1}\,\frac{p}{\rho^2}\,\frac{A}{J}$$

$$\left(\frac{\partial h}{\partial p}\right)_\rho = \frac{\gamma}{(\gamma - 1)\rho}\,\frac{A}{J}$$

So, substituting into Equation (182) the expression for local Mach number reduces to the well known expression

$$M = \frac{U}{\sqrt{g\,\gamma\,R_{sp.}\,T\,J}}$$

SHOCK SHAPE PREDICTION

CURVE FITTING PROCEDURES

Equation (85) with a symmetric and $\cos\theta$ term may be fitted to a graphical representation of the shock by merely observing the pitch plane (where $\theta = 0°$, 180°) and picking various points on the shock wave, inserting the appropriate values for the S_i and r_i of the point, and then solving the resulting linear simultaneous algebraic equations for the coefficients. These equations are of the form

$$S_i = \sum_{p=0}^{p}\left(\sum_{n=1}^{n} a_{2n,2p}\, r_i^{2n}\right) \pm \sum_{m=1}^{m}\left(\sum_{n=1}^{n} a_{2n-1,2m-1}\, r_i^{2n-1}\right)$$

$i = 1$, NUMBER OF COEFFICIENTS

$+$ FOR $\theta = 0°$ AND $-$ FOR $\theta = 180°$

where the $a_{2n,2p}$, $a_{2n-1,2m-1}$ are the coefficients and are unknowns.

This method is not applicable with Equation (86) due to its implicit form, and has the additional restriction that for any more than two $\cos g\theta$, $(g = 0, \infty)$, terms the θ variation of the shock wave is not uniquely defined because all the contributions are being lumped together.

A superior method which does not suffer from the above limitations determines the contribution to the S distance from each $\cos g\theta$ term.

At a given r_i, each group of terms can be rewritten as follows for Equation (85)

$$\sum_{p=0}^{p}\left(\sum_{n=1}^{n_p} a_{2n_p,2p}\, r_i^{2n}\right)\cos 2p\theta = \sum_{p=0}^{p} C_{(2p)i}\cos 2p\theta \qquad (185a)$$

$$\sum_{m=1}^{m}\left(\sum_{n=1}^{n_m} a_{2n_m-1,2m-1}\, r_i^{2n-1}\right)\cos((2m-1)\theta) = \sum_{m=1}^{m} C_{(2m-1)i}\cos((2m-1)\theta) \qquad (185b)$$

and similarly for Equation (86)

$$S_{0i} = C_{0i}$$

$$\sum_{p=1}^{P}\left(\sum_{n=1}^{n_p} a_{2n,2p}\, r_i^{2n}\right)\cos 2p\theta = \sum_{p=1}^{P} C_{(2p)_i}\cos 2p\theta \quad (186a)$$

$$\sum_{m=1}^{m}\left(\sum_{n=1}^{n_s} a_{2n-1,2m-1}\, r_i^{2n-1}\right)\cos\left((2m-1)\theta\right) = \sum_{m=1}^{m} C_{(2m-1)_i}\cos\left((2m-1)\theta\right) \quad (186b)$$

Since $2p$ and $(2m-1)$ are even and odd values, respectively, of g, a series of equations of the following form will result,

$$S_{i,j} = \sum_{g=0}^{g} C_{g_i}\cos g\theta_j$$

$$i = \text{CONSTANT}\ ;\ j = 1, g+1$$

where θ_j represents planes where a graphical representation is available.

$S_{i,j}$ = the S measurement at that r_i and θ_j.

$\sum_{g=0}^{g} C_{g_i}$ = the $g+1$ unknowns which represent the contribution of each term at that r_i.

It is seen that for a unique determination of $(g+1)$ constants, $(g+1)$ planes are needed. For each r_i a set of equations can be set up, and a plot of C_g versus r can be made with the C_g's defined by Equations (185) and (186). Then each curve can be fitted individually by conventional methods which are illustrated in the following example, along with the application of the previous theory.

Example

Assume that it is desired to use Equation(87) in the form

$$S = S_0 + \left(a_{1,1}\, r + a_{3,1}\, r^3\right) \cos\theta + \left(a_{2,2}\, r^2 + a_{4,2}\, r^4 + a_{6,2}\, r^6\right) \cos 2\theta$$

where

$$r^2 = a_{1,0}\, S_0 + a_{2,0}\, S_0^2 + a_{3,0}\, S_0^3$$

Now $g = 2$ so $g+1 = 3$ separate planes are needed. Let it be assumed that the $\theta = 0°$, 90°, 180° representations are available. Now let $i = 1$, $r_i = r_1 =$ some constant. Then at r_1

$$C_0 = S_0$$

$$C_1 = a_{1,1}\, r_1 + a_{3,1}\, r_1^3$$

$$C_2 = a_{2,2}\, r_1^2 + a_{4,2}\, r_1^4 + a_{6,2}\, r_1^6$$

and the equation reduces to the form

$$S = C_0 + C_1 \cos\theta + C_2 \cos 2\theta \qquad \text{FOR } r = r_1$$

Now, as shown in Figure 30

at $\theta = 0°$ $$S = S_1 = C_0 + C_1 + C_2 \tag{187}$$

at $\theta = 180°$ $$S_2 = C_0 - C_1 + C_2 \tag{188}$$

at $\theta = 90^\circ$ $$S_3 = C_0 - C_2 \tag{189}$$

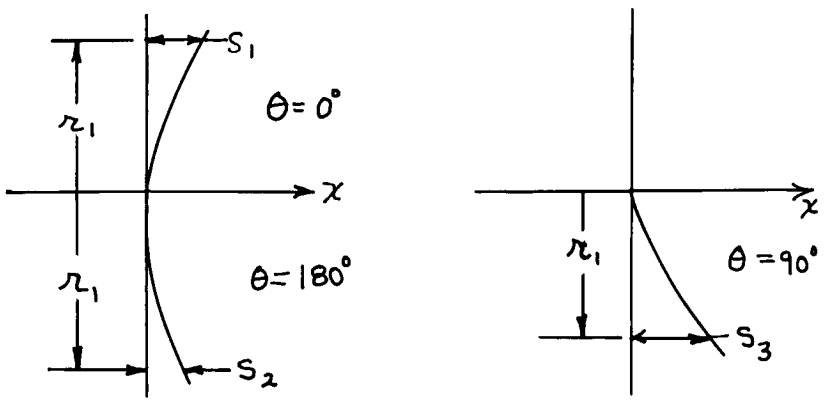

Figure 30. Definition of S_1, S_2, and S_3

Solving Equations (187), (188), and (189) simultaneously for

$$C_0 = \frac{1}{2}\left(\frac{S_1 + S_2}{2} + S_3\right)_{r=r_1}$$

$$C_1 = \left(\frac{S_1 - S_2}{2}\right)_{r=r_1}$$

$$C_2 = \frac{1}{2}\left(\frac{S_1 + S_2}{2} - S_3\right)_{r=r_1}$$

This gives one point on the C_g versus r plot. The entire process is repeated for a set of r values until the complete plots shown in Figure 31 can be made.

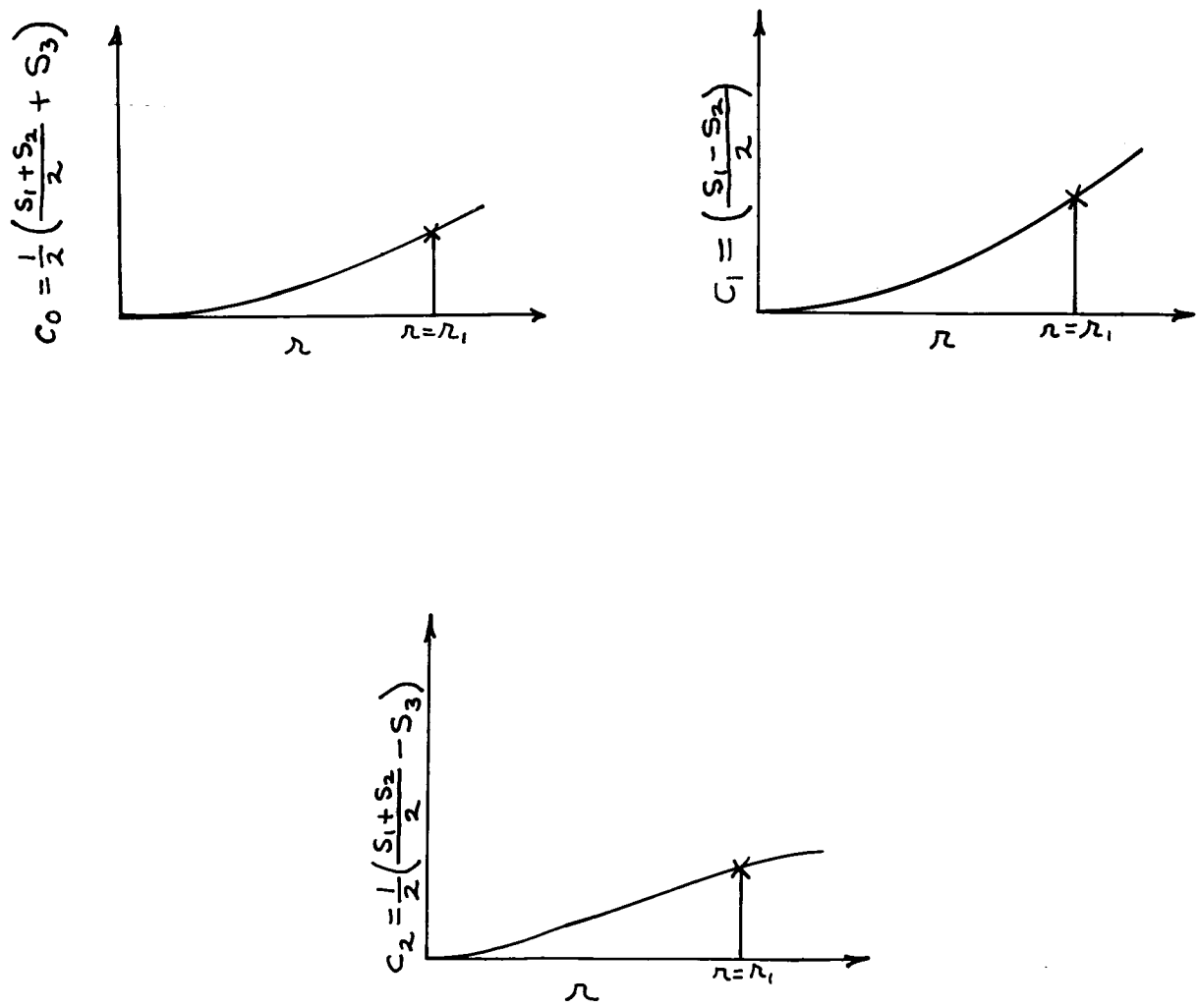

Figure 31. Typical Radial Distribution of Parameters C_0, C_1 and C_2

Now each of these curves can be independently fitted by the equations

$$r^2 = a_{1,0}\, c_0 + a_{2,0}\, c_0^2 + a_{3,0}\, c_0^3$$

$$c_1 = a_{1,1}\, r + a_{3,1}\, r^3$$

$$c_2 = a_{2,2}\, r^2 + a_{4,2}\, r^4 + a_{6,2}\, r^6$$

respectively.

This may be easily done after determining which points on the curve are to be used. These points must be equal in number to the number of coefficients to be determined and should be selected to result in the best overall fit of the computed curve. If the points are selected as the r_i's just used to define the curve, then an equation of the following form results,

$$r_i^2 = \frac{a_{1,0}}{2}\left(\frac{S_1+S_2}{2}+S_3\right)_i + \frac{a_{2,0}}{4}\left(\frac{S_1+S_2}{2}+S_3\right)_i^2 + \frac{a_{3,0}}{8}\left(\frac{S_1+S_2}{2}+S_3\right)_i^3$$

where three appropriate i's are chosen and the resultant linear equations solved for $a_{1,0}$, $a_{2,0}$, $a_{3,0}$.

For Curve 2

$$\left(\frac{S_1-S_2}{2}\right)_i = a_{1,1}\, r_i + a_{3,1}\, r_i^3$$

where two i's are chosen and the equations are solved for $a_{1,1}$ and a_3.

For Curve 3

$$\frac{1}{2}\left(\frac{S_1+S_2}{2}-S_3\right)_i = a_{2,2}\, r_i^2 + a_{4,2}\, r_i^4 + a_{6,2}\, r_i^6$$

where three i's are chosen and the equations are solved for $a_{1,2}$, $a_{4,2}$, and $a_{6,2}$.

This general analysis can be applied to any number of coefficients or groups of coefficients and is completely analytic, the only requirement being that the appropriate number of planes are available for determining the S_i's.

Shock Shape for Apollo, α = 22 Degrees

The shock shape for the Apollo Command Module may be predicted by using the Kaattari method, detailed in Reference 13, or by scaling an experimentally determined shock. Both methods have been applied to the case defined by the following flight conditions,

Angle-of-Attack	= 22 degrees
Velocity	= 22,754 feet per second
Altitude	= 150,480 feet

The scaled shock was found by using the procedure recommended in Reference 22, in which the local standoff distance is scaled in proportion to the predicted standoff distance on the longitudinal axis. This scaling thus in general is not linear with shock density ratio. The two resulting shock shapes are shown in Figure 32. In the checkout of this case, the results of which are presented in the next section, the hand improvement of the shock shape started from the scaled shock. The details of the procedure for methodically improving the shock shape are also explained in the following section.

SHOCK PREDICTION FOR TEST CASES

Shock Prediction for Sphere, α = -40 Degrees

A zero angle-of-attack flow field was computed for a sphere at $M = 10$ for a perfect gas of $\gamma = 1.4$ using a thoroughly checked out inverse method program obtained from the NASA/Ames Research Center. Since the S&ID inverse program integrates along the body axis of symmetry, an angle-of-attack case was obtained by a coordinate rotation as shown in Figure 33.

This case was run as the basic check for the angle-of-attack formulation, since the shock is very accurately known. All that is required is to define the shock analytically. Although the zero angle-of-attack shock is analytic and known, the analytic coordinate rotation proved cumbersome and would have required special programming. A graphical solution was made using the principles of descriptive geometry. For this case the shock shape can be found in all θ planes. The planes $\theta = 0°, 90°, 180°$ were used to define a shock fit equation of the form given in Equation (87). The analytic fit was found to be about as accurate as the shock could be constructed graphically. This shock also fit the graphical shock in the $\theta = 45° - 225°$ plane with a high accuracy. The resulting shock fit equation, scaled to a shock radius on the wind direction axis of 1.0, is

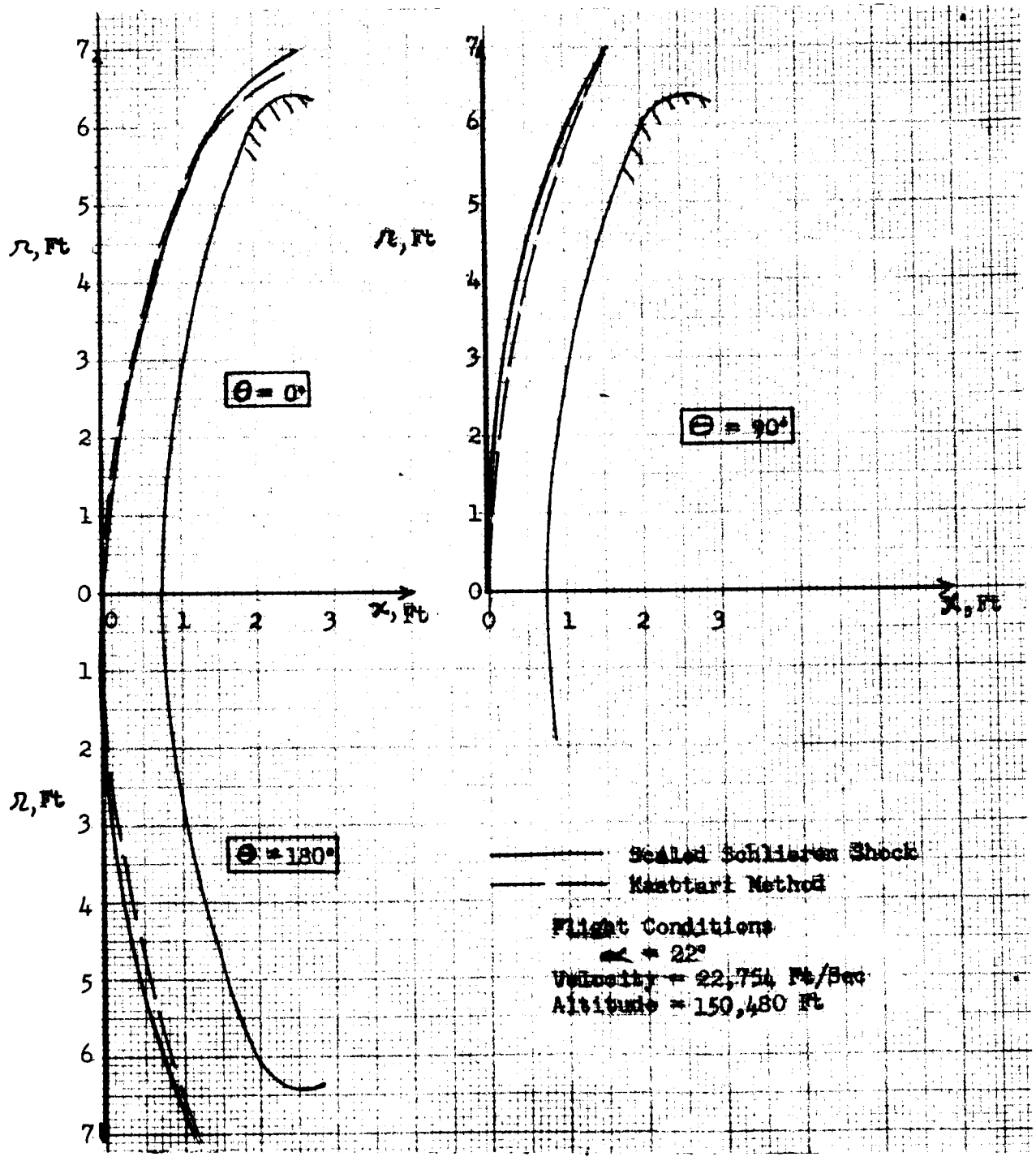

Figure 32. Preliminary Apollo Command Module Shock Shape

$$S = C_0 + C_1 \cos\theta + C_2 \cos 2\theta$$

$$S = S_0 - \left(0.146\,r - 0.0381\,r^3 + 0.295\,r^5\right)\cos\theta$$

$$- \left(0.0217\,r^2 + 0.0835\,r^4 - 0.1500\,r^6\right)\cos 2\theta$$

S_0 is called the symmetric term

where

$$r^2 = 2.365\,S_0 - 1.200\,S_0^2$$

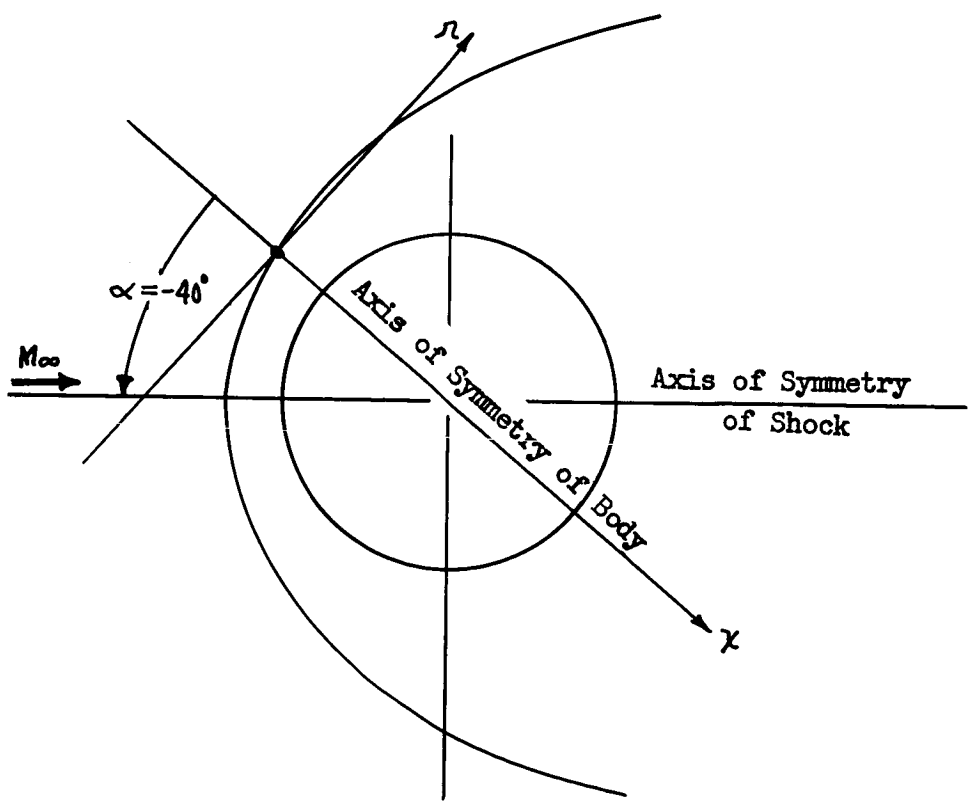

Figure 33. Coordinate Transformation for Sphere Flow Field at Angle-of-Attack

This shock is presented in Figure 34. The shock shape is shown in five θ -planes. Also plotted are the zero angle-of-attack shock and two special analytic functions, C_0 and $C_0 + C_2$.

It is of interest to note the following physical features of this shock:

1. The values of the symmetric and $\cos\theta$ terms are both an order of magnitude larger than the values of the $\cos 2\theta$ term.

2. The shock shape in the $\theta = 90°$ plane, the zero angle-of-attack shock, and the shock shape defined by the symmetric terms only all differ from each other by roughly the magnitude of the $\cos 2\theta$ terms.

3. The use of the zero angle-of-attack shock as a first approximation to the symmetric term is in error by as much as approximately 15 percent of the local stand-off distance.

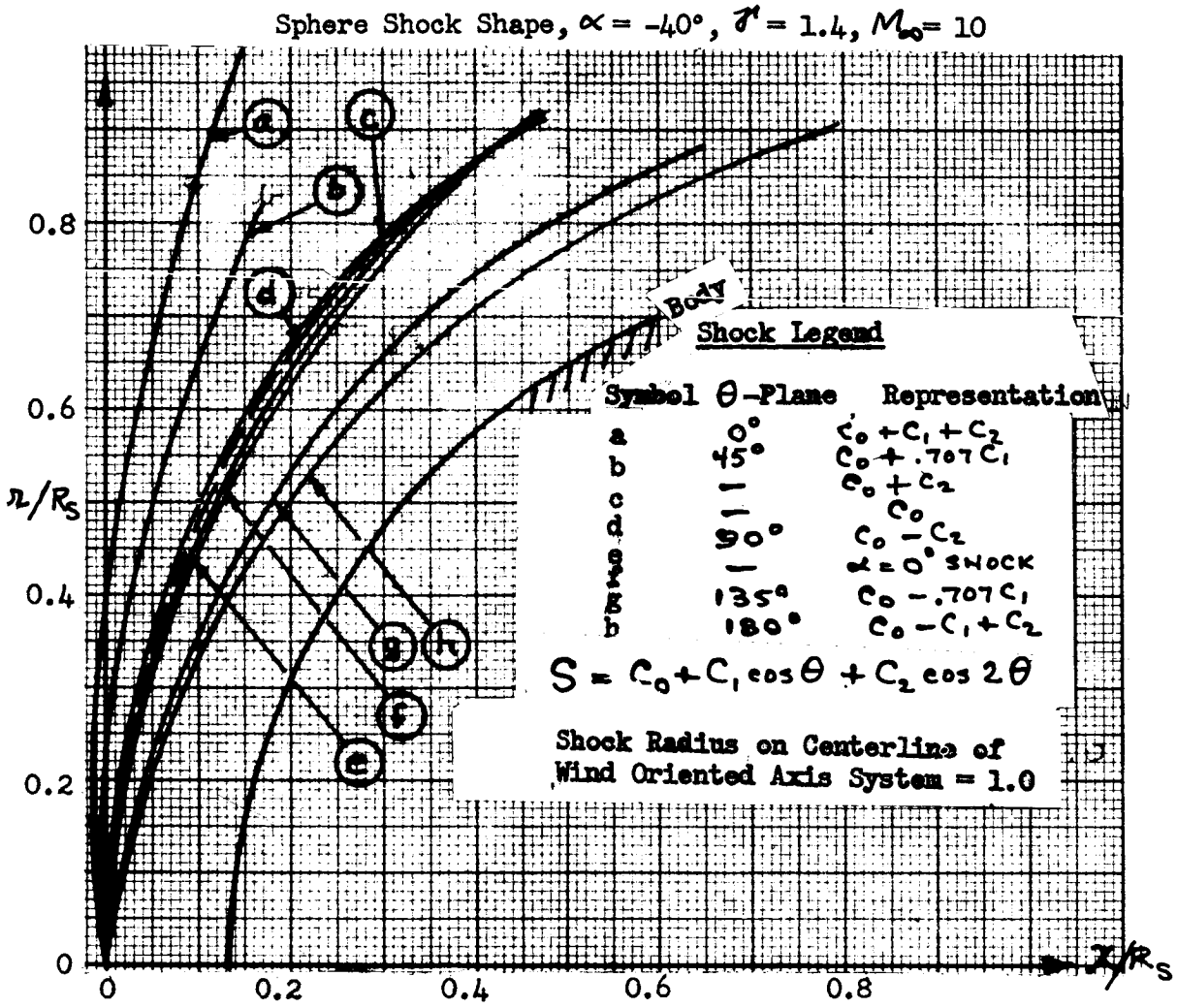

Radial Variation of C_0, C_1, and C_2

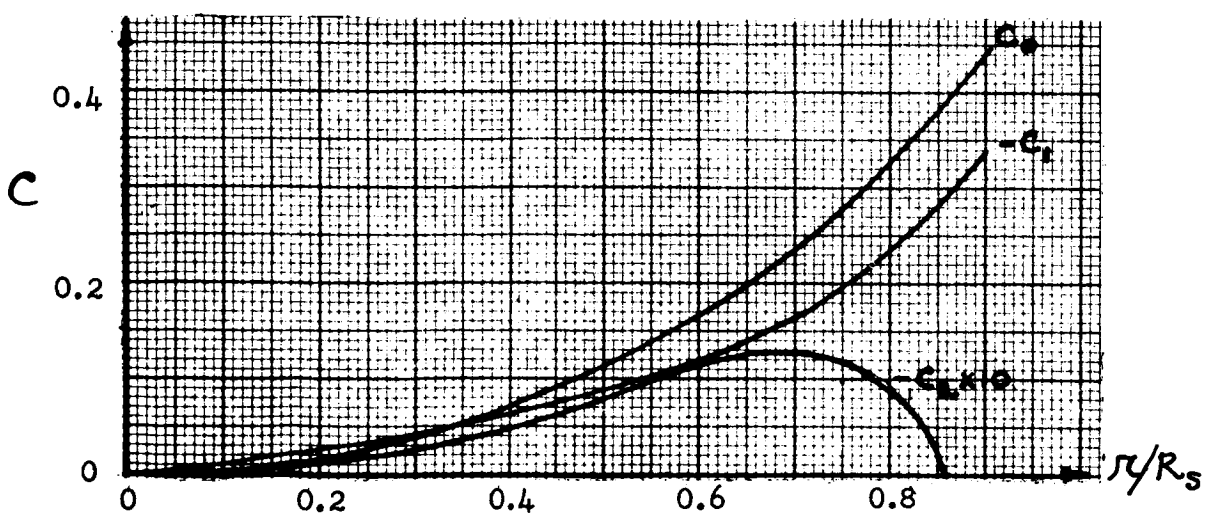

Figure 34. Analytic Sphere Shock Shape

RESULTS FOR TEST CASES

SPHERE FLOW FIELD, α = 40 DEGREES

As stated previously, the sphere is an excellent case to use in developing a three-dimensional flow field computer program, since the results obtained can readily be compared to $\alpha = 0°$ results by proper coordinate transformations. The results obtained for the sphere at $\alpha = 40°$ are presented in Figures 35, 36, and 37. Figure 35 presents the complete pitch plane and front view of the sphere flow field including the sonic lines and a set of typical streamlines. The upper sonic line was easily obtained and thoroughly substantiates the NASA/Ames results of Reference 4. The lower sonic line in the pitch plane was more difficult to obtain because of the greater marching distance and the fact that there is a continual reduction in the number of grid points remaining with which to form lateral derivatives as the body is approached. As a result, the accuracy of the calculations becomes less in this region. However, a portion of the lower sonic line in the flow field was obtained and the agreement as to location checks with the position of the upper sonic line. The stagnation point obtained with the program lies on the flow axis as it should, adding further substantiation to the S&ID results.

The body locations obtained by the program are presented in Figures 35 and 36 for three meridian planes, $\theta = 0°/180°$, $45°/225°$, and $90°/270°$. The shock shapes for each of these planes are also included. The body, circular arc of 0.76 ft radius obtained from the Ames result, is shown for comparison. The Ames shock standoff distance of 0.103 ft was used to properly orient the circular arc.

Figure 37 presents the body pressure distributions in each of the three meridian planes. Again, results taken from the Ames $\alpha = 0°$ case have been transformed by coordinate rotation and presented as substantiation of the S&ID program results. The sonic pressure is also shown for reference. The approximate radial positions of the sonic points in the pressure distribution plot for the pitch plane appear to agree with the results shown in Figure 35. Good agreement is also obtained with the Ames data for the stagnation pressure.

APOLLO FLOW FIELD, α = 22 DEGREES

An equilibrium real air flow field over the Apollo Command Module was computed for the following flight condition,

α = 22 Degrees
Velocity = 22,754 Feet/Second
Altitude = 150,480 Feet

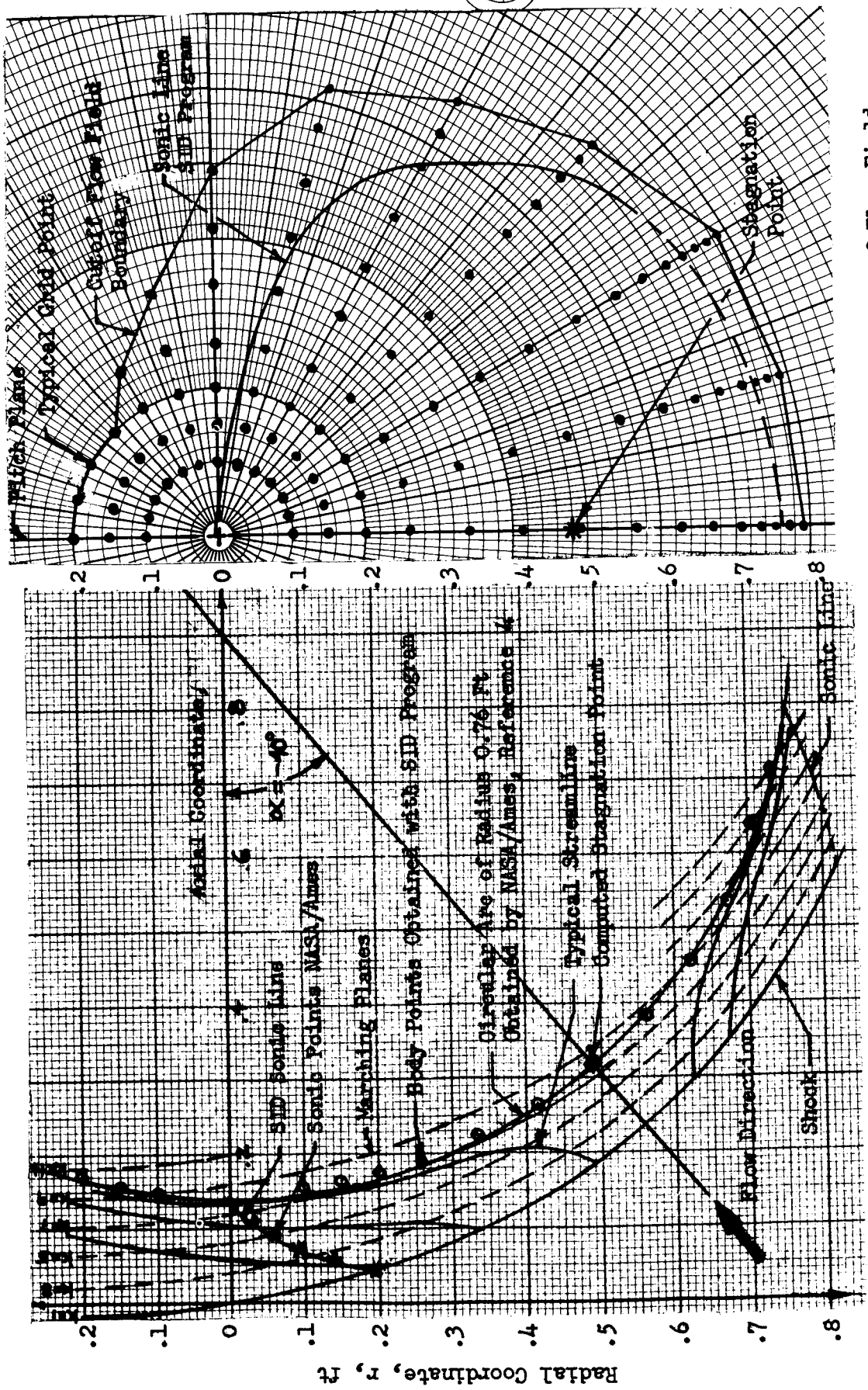

a. Pitch Plane Flow Field

b. Frontal View of Flow Field

Figure 35. Pitch Plane and Frontal View of Flow Field for Sphere at 40° Angle-of-Attack, ($\gamma = 1.4$)

Note: Numbers in Parentheses Refer to "i" Subscript on Grid Points

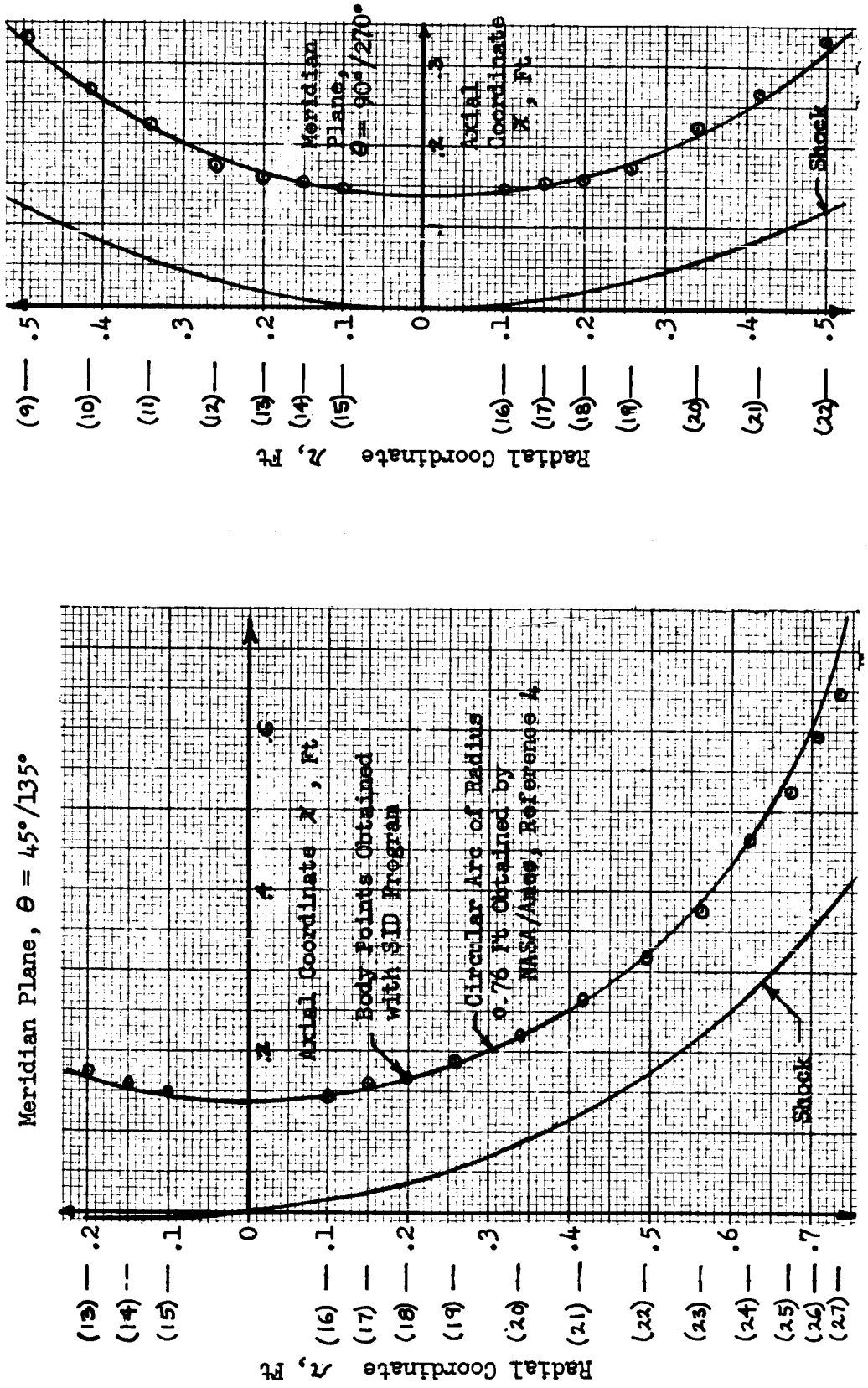

Figure 36. Flow Field in Planes θ = 45/225° and θ = 90°/270°, Sphere at 40° Angle-of-Attack (γ = 1.4)

Note: (1) Open Symbols Denote SID Results.
Closed Symbols Represent NASA/Ames Results, Reference 4.
(2) Numbers in Parentheses Refer to "i" Subscript on Grid Points.

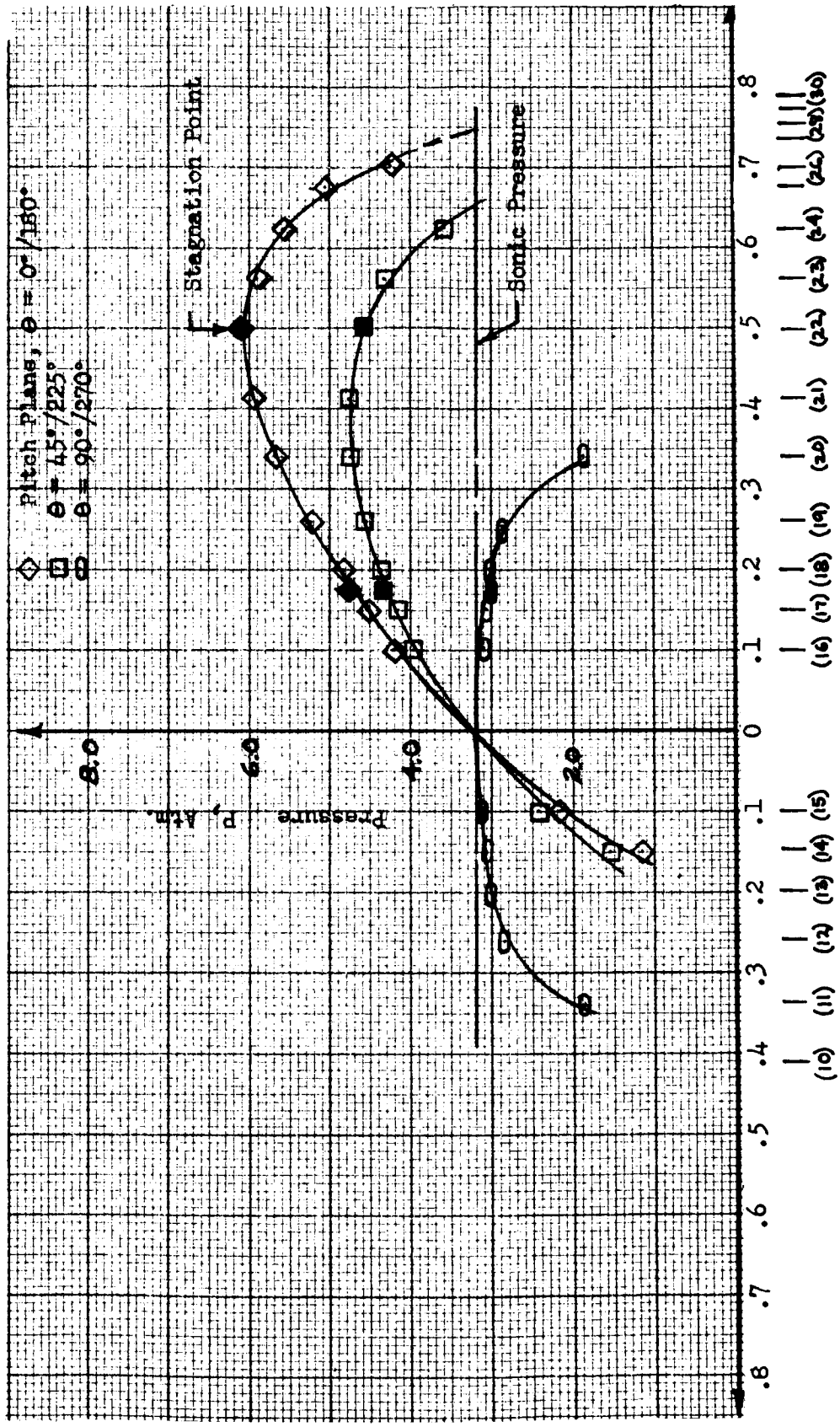

Figure 37. Pressure Distributions, Sphere at 40° Angle-of-Attack (γ = 1.4)

As previously described, a scaled schlieren shock shape was found and was used for the initial shock estimate in the pitch plane. The shock shape in the 90° meridian plane was estimated by Kaattari's methods. Since this case also served in program checkout, it proved simpler to correct the shock shape by hand as the program checkout proceeded for this difficult angle-of-attack case rather than use the iterative convergence procedure. For example, the problem of integration instability caused by too large an integration interval was encountered and studied during the course of shock shape improvement. A much better understanding was also obtained of the best values for Qtest and Mtest. These considerations could only be evaluated on single program runs. As the effort continued it became apparent that, at least for high speed real gas flows, a reasonably rapid hand perturbation procedure could be used to converge to the desired body shape.

The grid point locations are shown on Figure 41 where each original point in the cutoff grid is shown with a body surface velocity vector. The θ spacing is a uniform 15°. Points are closer together near the outer radii to ensure accuracy in the stagnation region as well as the shoulder flow where high property gradients occur. The choice of the radial spacing proved a problem. For any greater point spacing than that shown, the accuracy of the stagnation region was degraded rapidly. The close radial spacing required resulted in an integration step size of 0.0175 ft to maintain a stable integration near the shoulder. Since the program uses a fixed step size, a total of about 55 integration (k) planes were needed to define the entire flow field. Single run time was about 90 minutes for the real gas runs. The grid cutoff limits were selected to avoid unnecessary calculations in the high supersonic flow regions, particularly in the θ =180° plane.

The initial shock was fitted by the standard shock equation using the explicit form of the symmetric term. Both symmetric, $\cos\theta$, and $\cos 2\theta$ terms were used. If one represents the shock shape as a function of r in a given meridian plane by S subscripted as defined in Figure 34.

$$S_1 = C_0 + C_1 + C_2$$

$$S_2 = C_0 - C_2$$

$$S_3 = C_0 - C_1 + C_2$$

where

C_0, C_1, and C_2 are the functions of r that are the coefficients of the $\cos(0)\theta$, $\cos\theta$, and $\cos 2\theta$ terms respectively. Solving for C_0, C_1, and C_2 in terms of the predicted shock shape coordinates one obtains,

$$C_0 = \frac{S_1}{4} + \frac{S_3}{2} + \frac{S_2}{4}$$

$$C_1 = \frac{S_1}{2} - \frac{S_2}{2}$$

$$C_2 = \frac{S_1}{4} - \frac{S_3}{2} + \frac{S_2}{4}$$

These equations were used to compute C_0, C_1, and C_2 which were in turn fitted by polynomials to obtain the initial coefficients for the analytic shock fit. Analytic corrections to the shock were made by first finding corrections required in the individual planes $\theta = 0°$, $90°$, and $180°$ and then using the following equations to obtain the corrected values of C_0, C_1, and C_2.

$$\Delta C_0 = \frac{\Delta S_1}{4} + \frac{\Delta S_3}{2} + \frac{\Delta S_2}{4}$$

$$\Delta C_1 = \frac{\Delta S_1}{2} - \frac{\Delta S_2}{2}$$

$$\Delta C_2 = \frac{\Delta S_1}{4} - \frac{\Delta S_3}{2} + \frac{\Delta S_2}{4}$$

This approach works best if shock shape perturbations result in only local body shape perturbations, a situation which is approached as the free stream Mach number and shock density ratio both approach infinity. The Apollo flight condition was such that this method worked well.

The use of a small integration step size allowed the Q_{test} to be selected at the rather low value of 0.1. The M_{test} was selected at 0.6, a value which seemed to work well on several cases investigated. Smoothing started on plane $k = 15$ and was terminated by the normal test. Two smoothings per plane were used. The weighting factors are shown in Table 3.

The hand correction of the shock started logically with the lowest order terms in r. The local shock standoff distance was corrected by a percentage of the predicted body error on the same normal. To move the predicted body the shock was moved in the same direction. 25% of the body error was applied at the shock. The correction was expressed as a polynomial in r for ease in correcting S_1, S_2, or S_3. The correction can either be positive (the shock moves toward the body) in which case no problem occurs, or negative,

in which case a problem may exist. The objective is to avoid an unrealistic irregular shock, especially one with a reversal of curvature. The correction was fitted by the equation

$$\Delta S_{SHOCK} = \frac{\Delta S_{BODY}}{4} \, r^{\beta}$$

If the correction was in the negative direction it was first verified analytically that the shock did not exhibit an inflection point. Early runs on this case utilized the perfect gas option built into the program. A value of γ was chosen that duplicated the real gas normal shock density ratio. Only after obtaining a fairly good body prediction were real gas runs made. This procedure proved that the use of a perfect gas simulation of a real gas flow could save machine time. When the change to a real gas calculation was made, the predicted body shape did not change radically.

The flow field results are shown in Figures 38, 39, and 40. The pressure distribution is compared with Newtonian in Figure 40. The data variations all appear reasonable and consistent. The input data to the program is summarized below in Tables 2 and 3.

Table 2

Apollo Analytic Shock Shape Coefficients

Terms in Polynomial	(Symmetric Term)	(Coefficient of θ)	(Coefficient of 2θ)
r	0	.032	0
r^2	.03021	0	0
r^3	-2.5×10^{-4}	5×10^{-4}	-2.5×10^{-4}
r^4	3.88×10^{-5}	5×10^{-5}	5.125×10^{-5}
r^8	8×10^{-9}	-1.6×10^{-9}	8.0×10^{-9}
r^{10}	1.28×10^{-10}	0	-1.28×10^{-10}
r^{12}	9.063×10^{-12}	7.25×10^{-12}	-1.813×10^{-12}
r^{16}	2.56×10^{-15}	5.125×10^{-15}	2.56×10^{-15}

Table 3

Smoothing Weighting Factors

r	1	2	2.9	3.7	4.33	4.75	5	5.25
F	1	1	.95	.8	.2	.1	.05	0
r	5.5	5.67	5.83	6	6.16	6.33	6.5	
F	0	0	0	0	0	0	0	

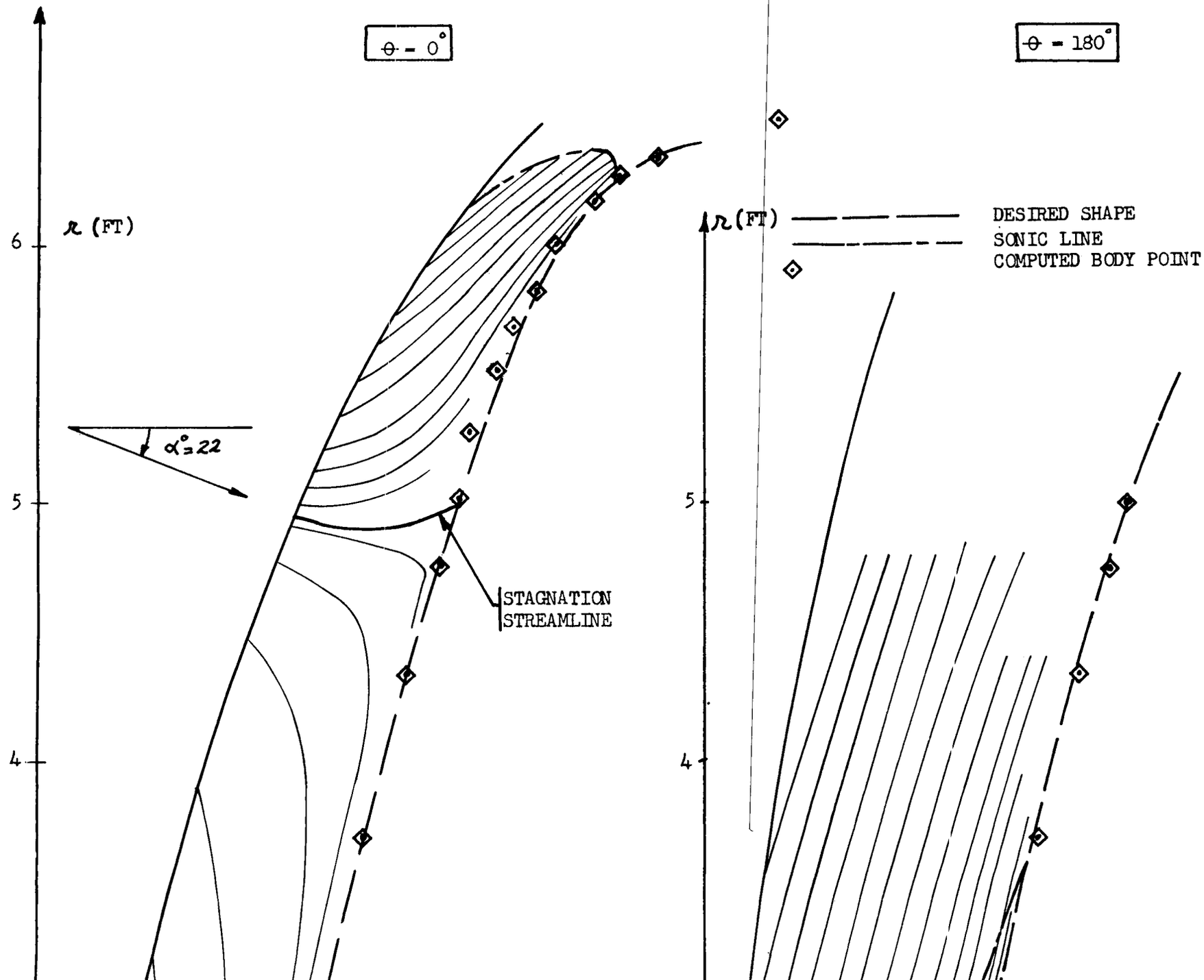
θ = 0°
θ = 180°
r (FT)
6
5
4
α° = 22
STAGNATION STREAMLINE
DESIRED SHAPE
SONIC LINE
COMPUTED BODY POINT

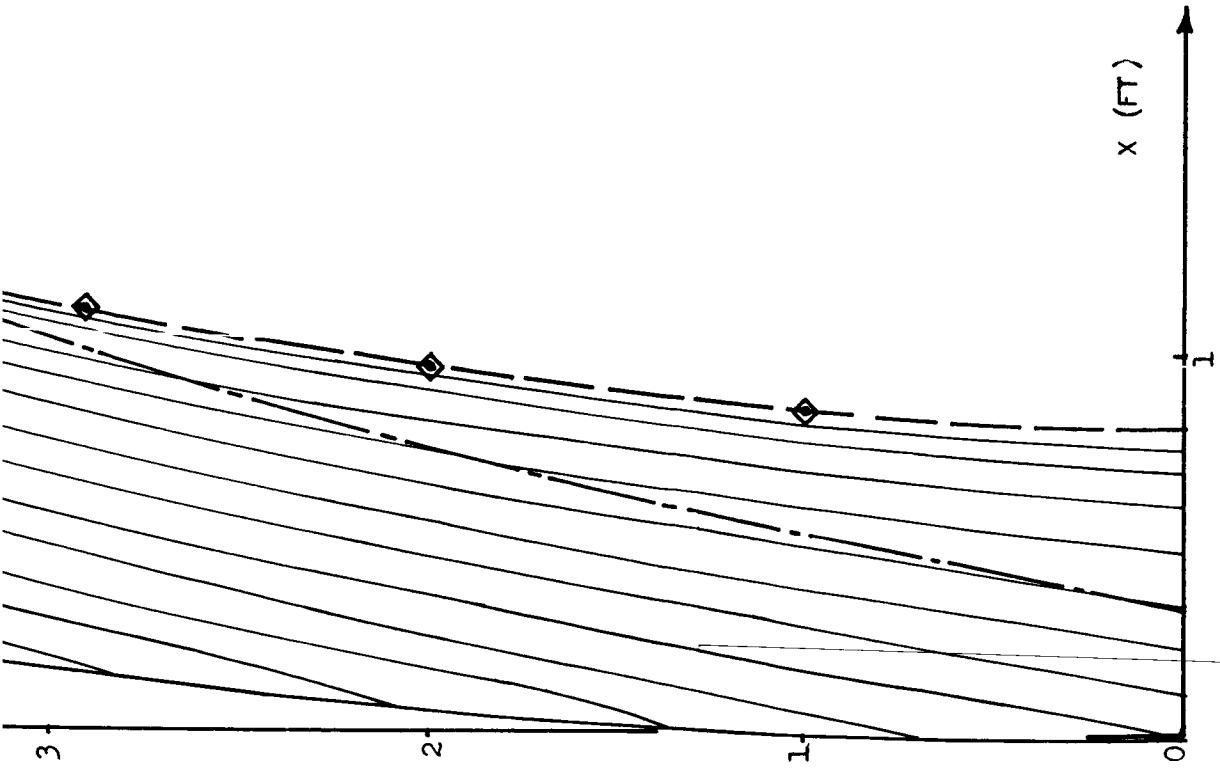

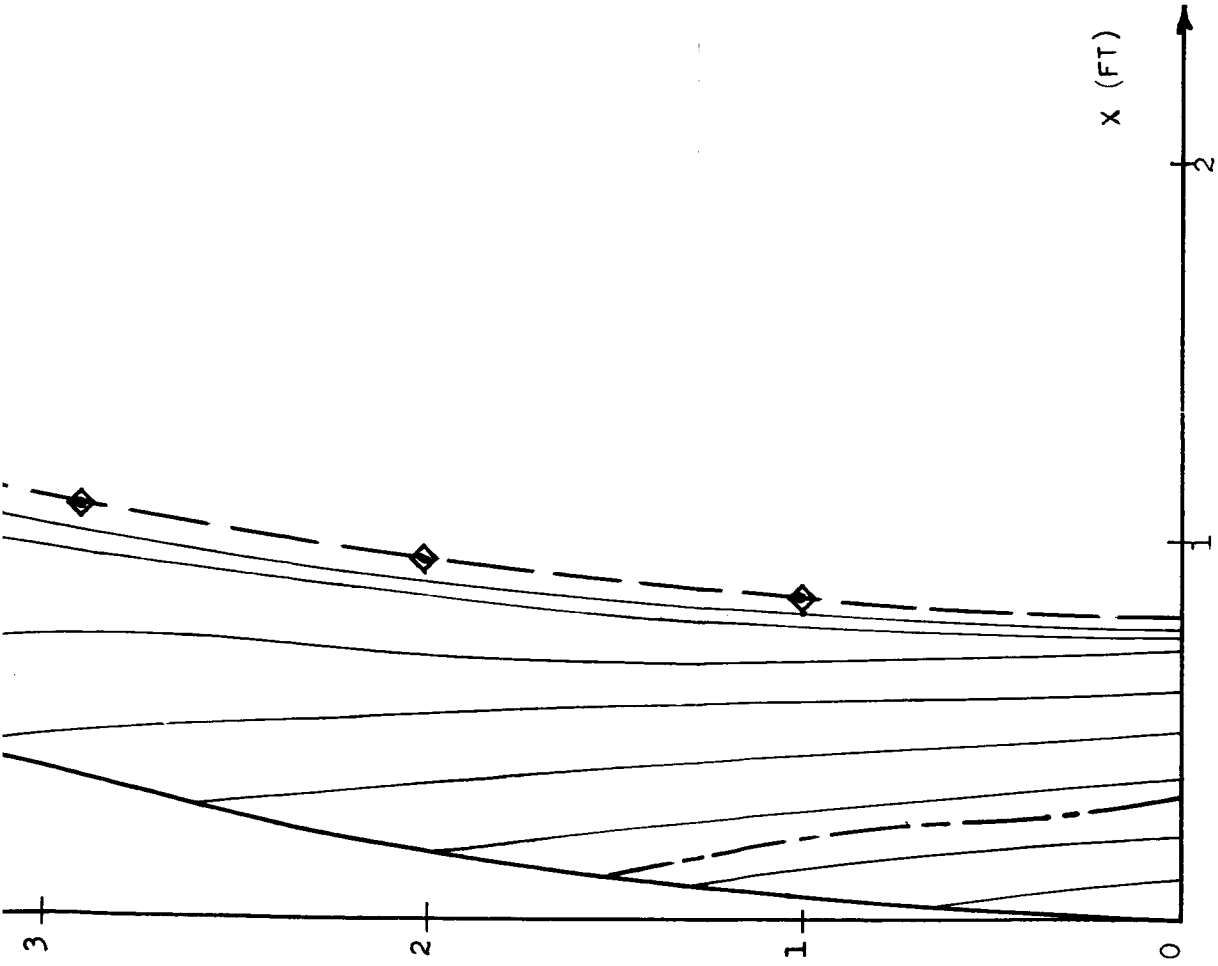

FIGURE 38. FLOW FIELD AROUND APOLLO COMMAND MODULE, $\theta = 0°, 180°$

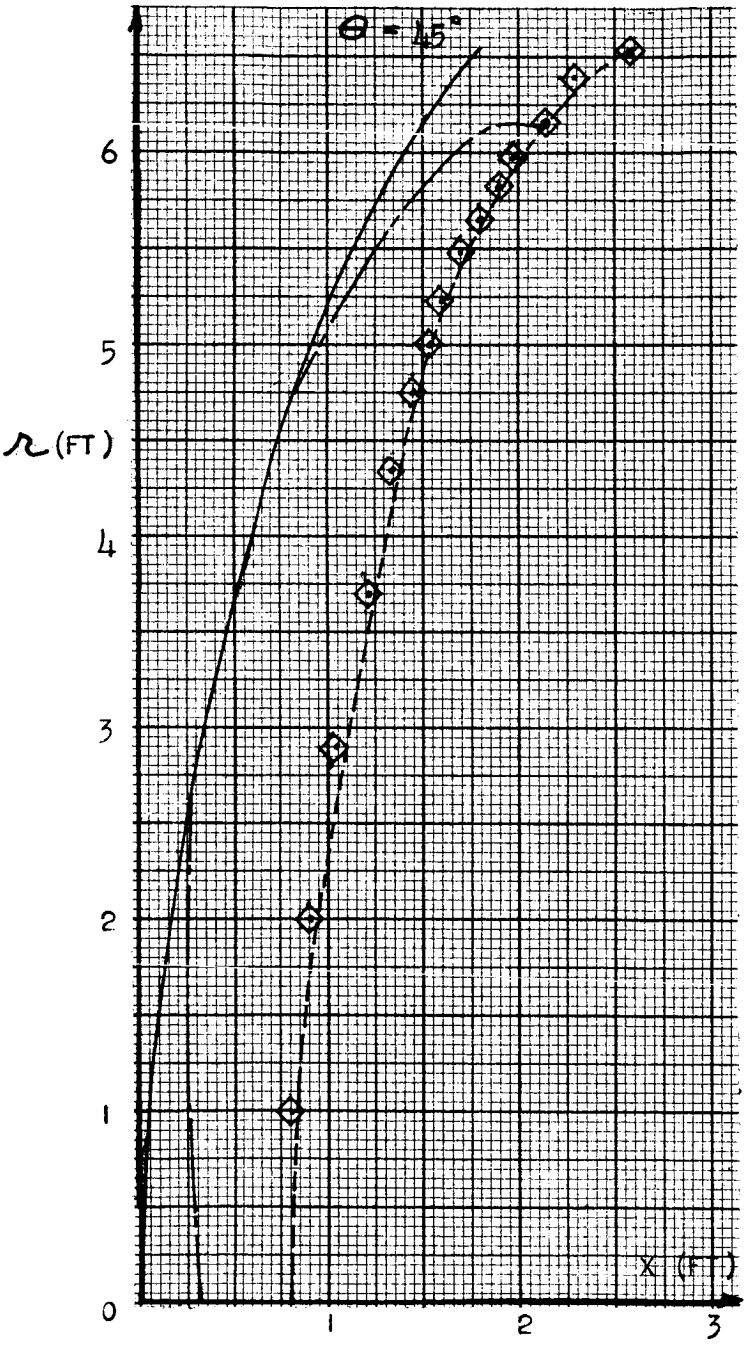
θ = 45°
r (FT)
X (FT)
0
1
2
3
4
5
6
1
2
3

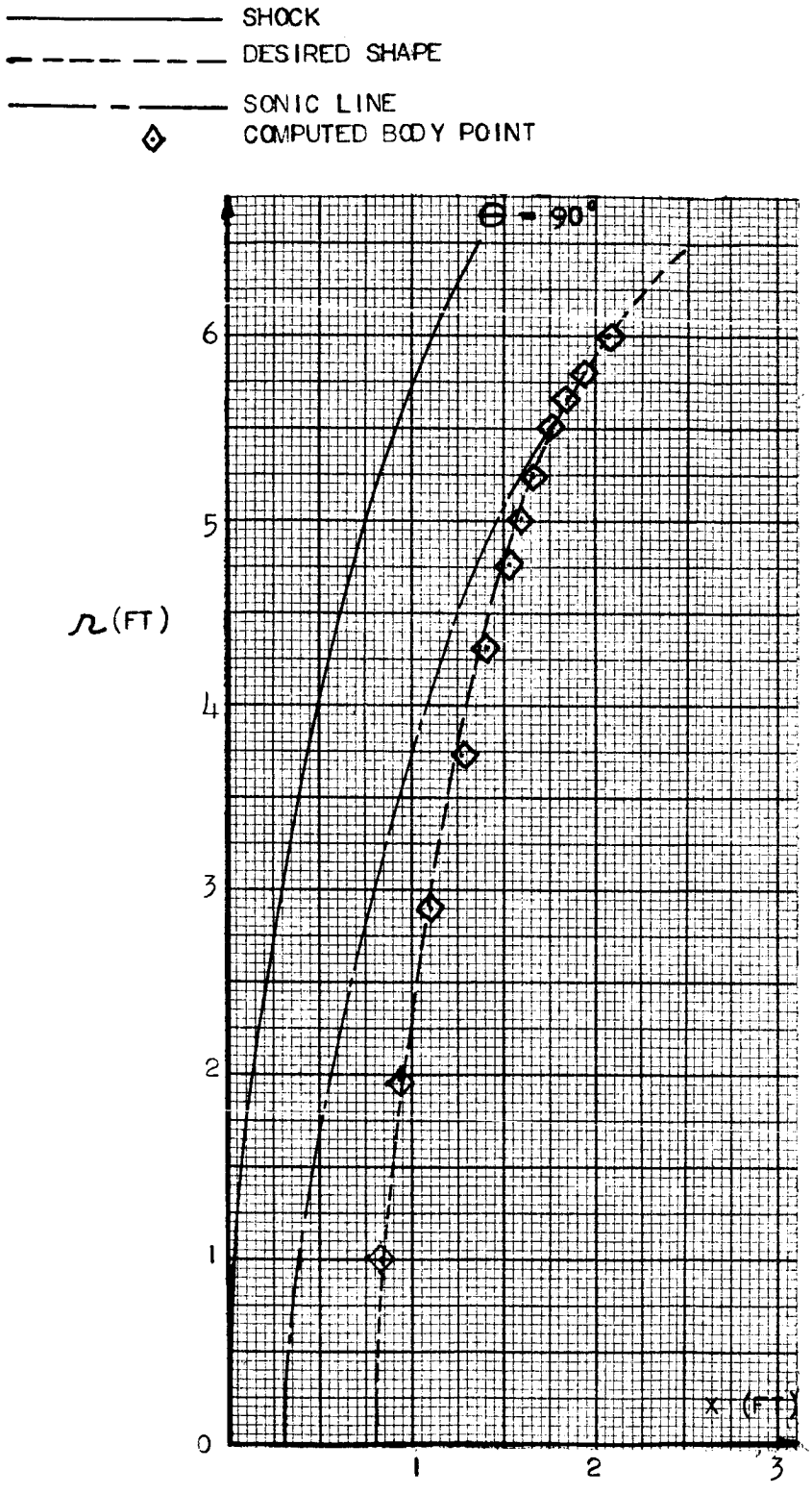
SHOCK
DESIRED SHAPE
SONIC LINE
COMPUTED BODY POINT
θ = 90°
r (FT)
x (FT)
0
1
2
3
4
5
6
1
2
3

2

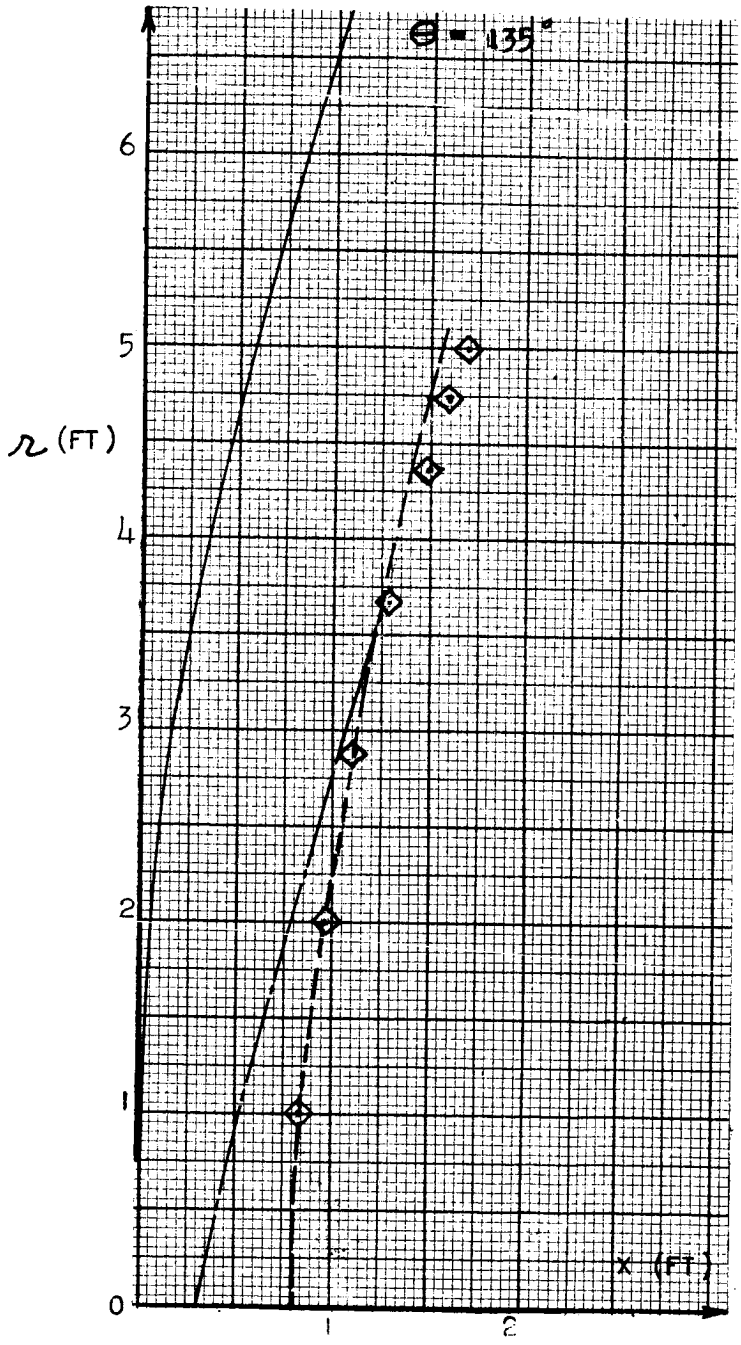

FIGURE 39. FLOW FIELD AROUND APOLLO COMMAND MODULE
$\theta = 45°, 90°, 135°$

3

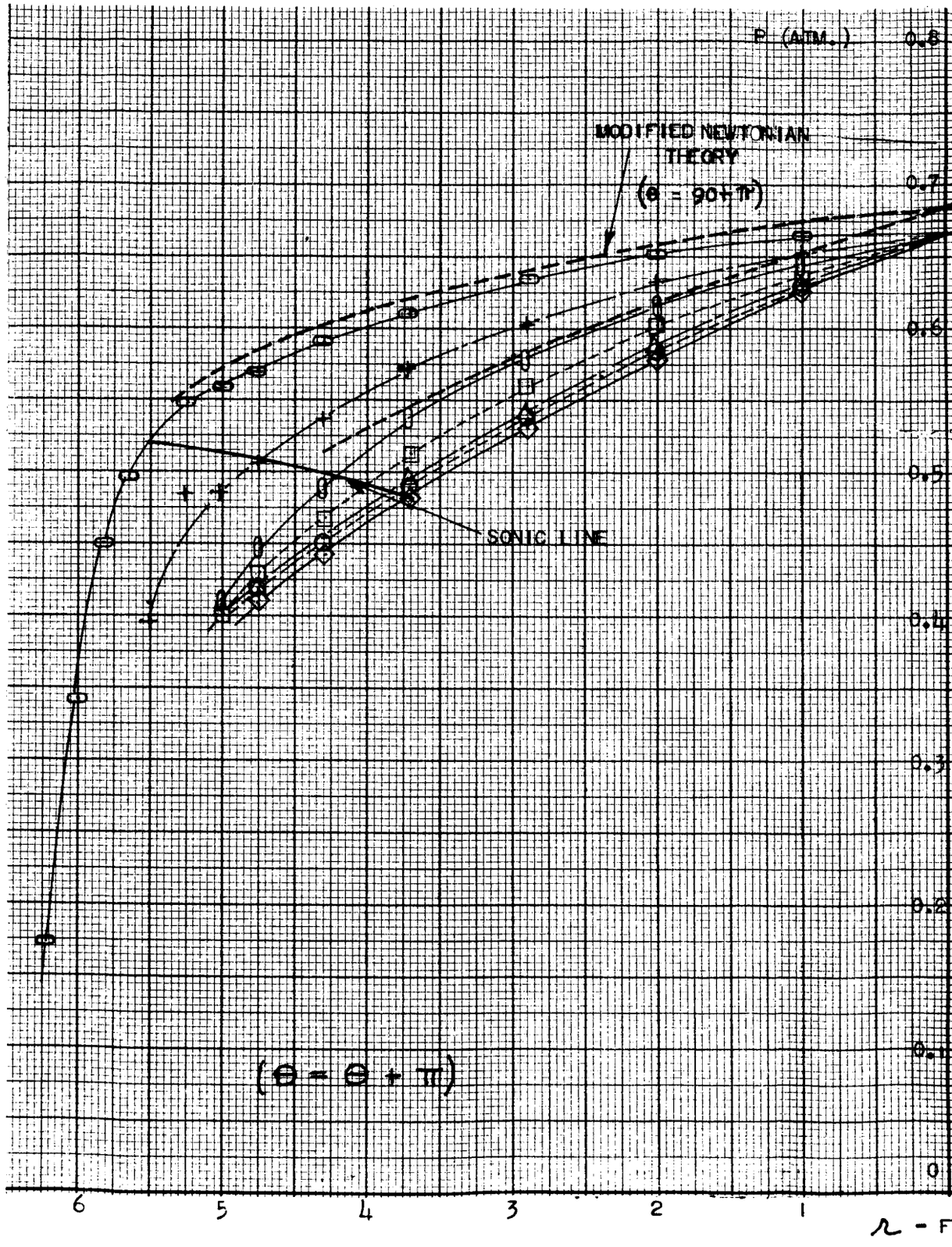
P (ATM.)
MODIFIED NEWTONIAN THEORY
(θ = 90+π)
SONIC LINE
(θ = θ + π)
0.8
0.7
0.6
0.5
0.4
0.3
0.2
0
6
5
4
3
2
1
r - F

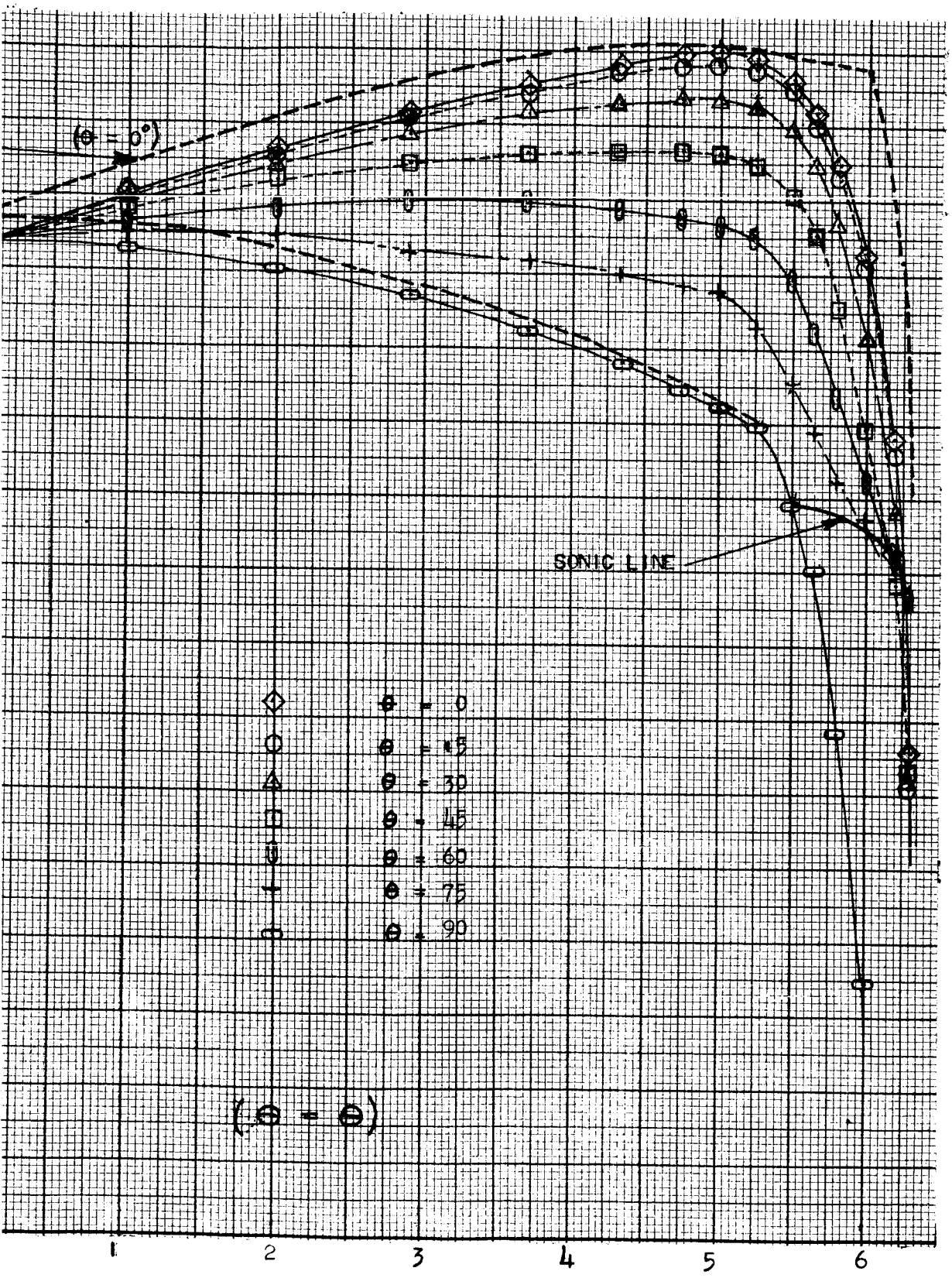

FIGURE 40. BODY PRESSURE DISTRIBUTION, APOLLO COMMAND MODULE

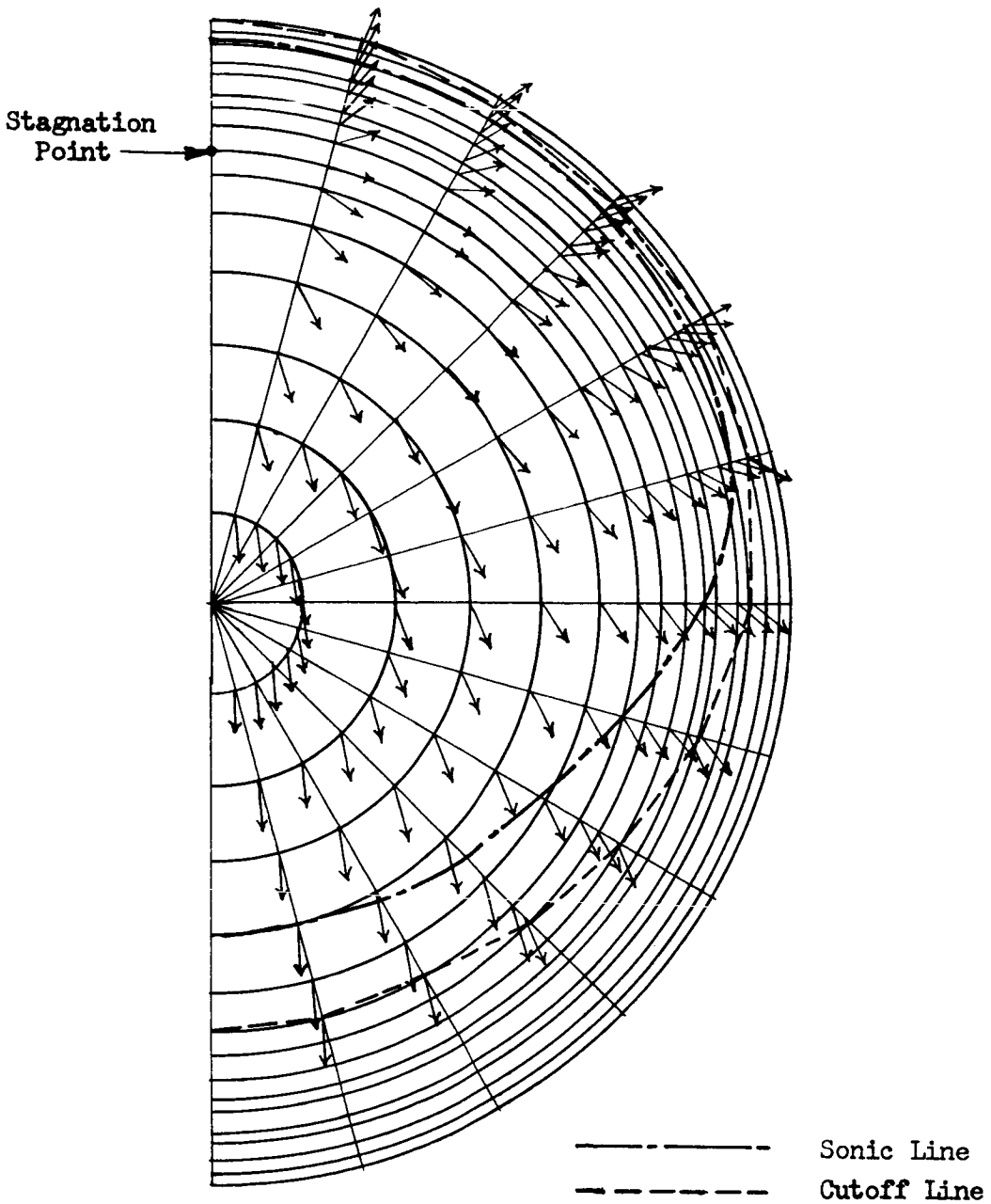

Figure 41. Body Surface Streamline Pattern, Apollo Command Module

BEHAVIOR OF ITERATIVE CONVERGENCE TECHNIQUE

The iterative convergence technique for improving the shock shape and predicted body shape has been tested on several sample cases. Functional checks were performed on a perfect gas zero angle-of-attack sphere flow. Both a one- and two-coefficient approximation of the shock were used and results indicated an improved shock was obtained by the automatic procedure.

An early test of the procedure was made for a perfect gas, $\gamma = 1.4$, flow over the Apollo shape at $\alpha = 0°$. The implicit shock shape was used; and it was found that for this three-coefficient shock fit the shoulder region did not improve on the first iteration, although the large face radius was improved. Subsequent iterations were not attempted, because although slow convergence was possible it did not appear satisfactorily rapid. The cause of the poor performance was traced to the inherent behavior of perturbed shocks of the implicit fit. It was concluded that the explicit fit would have less cross-coupling effects between different coefficients. This explanation was borne out on an iterative run on a real gas Apollo flow field for $\alpha = 0°$. One iteration was run in which a two coefficient (explicit shock fit) was initially perturbed very slightly from the correct shape which was found by hand perturbation. The shock and body shapes resulting from the automatic iteration were improved in comparison with the initial shapes.

NOMENCLATURE

a	speed of sound; shock coefficient defined in Equation (83); body coefficient defined in Equation (129)
c	coefficients defined in Equation (185)
d	maximum diameter of Apollo
f	non-radial flow factor
g	$x-S$; shock equation parameter defined by Equation (83)
h	specific enthalpy
$h_p = (\partial h/\partial p)_\rho$	
$h_\rho = (\partial h/\partial \rho)_p$	
i	grid coordinate defining value of r
$\vec{i}'$	unit vector along x'-axis
$\vec{i}_r$	unit vector along direction of increasing r
$\vec{i}_x$	unit vector along x-axis
$\vec{i}_\theta$	unit vector along direction of increasing θ
j	grid coordinate defining θ
K, k	$\cos\alpha + S_r \cos\theta \sin\alpha - \frac{S_\theta}{r} \sin\theta \sin\alpha$; integration plane index
L	surface arc length
M	Mach number
m	shock equation parameter defined by Equation (85)
N	$\sqrt{1 + S_r^2 + \left(\frac{S_\theta}{r}\right)^2}$; any positive integer
n	shock equation parameter defined in Equation (83) ; distance normal to body surface
$\vec{n}$	unit vector normal to shock surface

p	pressure; shock equation parameter defined in Equation (85)
Q	$ru - rvS_r - wS_\theta$
R	gas constant per unit mass of undissociated air; distance from body axis to point on surface; radius of curvature
r	a body-oriented cylindrical coordinate (see Figure 2); streamline radius (see Figure 12)
S	function describing shock,(Equation 10)
s	specific entropy
T	temperature
U	total velocity
u	velocity in the x-direction
v	velocity in the r-direction
$\bar{v}$	transformed velocity defined by Equation(27)
w	velocity in the θ-direction
$\bar{w}$	transformed velocity defined by Equation(28)
X	shear coordinate; distance measured from the shock surface in the x-direction
x, y, z	body-oriented Cartesian coordinates (see Figure 2)
x', y', z'	free-stream-oriented Cartesian coordinates (see Figure 2)
Z	compressibility factor
α	angle-of-attack
β	angular location of streamline (see Figure 12)
γ	specific heat ratio
Δ	distance between data points (see Figure 27); shock standoff distance
ϵ	density ratio access shock, error defined in Equation (127)
θ	a body-oriented cylindrical coordinate (see Figure 2); slope defined by Figure 14.

ρ density

ϕ a stream function defined by Equation (77)

ψ a stream function defined by Equation (78)

SUBSCRIPTS

b	measured in body-oriented system as defined by Equation (128)
c	corrected shock coefficient; coordinate of free stream stagnation streamline; control point
e	equilibrium
g	shock coefficient identification index defined in Equation (83)
I	refers to intersection of body normal and predicted body line segment
i, j	number of independent variables
H_1	hemisphere radius
H_2	shoulder radius
m	shock coefficient identification index defined in Equation (85)
n	normal to shock; shock coefficient identification index defined in Equation (85) ; exponent in general body fit equation
o	reference condition; intersection of shock with x-axis; origin of body-oriented system
p	shock coefficient identification index defined in Equation (85); number of shock coefficients; body segment of translation point
q	body segments of control points
r	partial derivative with respect to r
S	behind shock; measured in shock-oriented system as defined by Equation (153)
t	tangential to the shock, translational point
X	partial derivative with respect to X
x	partial derivative with respect to x or x-component
y	partial derivative with respect to y or y-component
z	partial derivative with respect to z or z-component

θ	partial derivative with respect to θ
∞	free stream
$\rightarrow$	vector quantity
0 (ZERO)	denotes shock equation form defined by Equation
1, 2, 3	number of independent variables, θ plane
*	sonic condition

REFERENCES

1. Theoretical Prediction of the Equilibrium Real Gas Inviscid Flow Field About Blunt Bodies, Phase II, Formal Written Report. Research and Advanced Development Division, AVCO Corporation (June 1963) (Contract NAS9-858).

2. Belotserkovskii, O. M. "Flow With a Detached Shock Wave About a Symmetrical Profile," PMM, Vol. 22, No. 2 (1958), pp. 206-219.

3. Fuller, F. B. Numerical Solutions for Supersonic Flow of an Ideal Gas Around Blunt Two-Dimensional Bodies. NASA Technical Note D-791 (July 1961).

4. Lomax, H. and Inouye, M. Numerical Analysis of Flow Properties About Blunt Bodies Moving at Supersonic Speeds in an Equilibrium Gas. NASA Technical Report TR-R-204 (July 1964).

5. Garabedian, P. A. and Lieberstein, H. M. "On the Numerical Calculations of Detached Bow Shock Waves in Hypersonic Flow," J. Aero. Sci., Vol. 25, No. 2 (February 1958), pp. 109-118.

6. Maslen, S. H. and Moeckel, W. E. "Inviscid Hypersonic Flow Past Blunt Bodies," J. Aero. Sci., Vol. 24, No. 9 (September 1957), pp. 683-693.

7. Gravalos, F. G.; Edelfelt, I. H.; and Emmons, H. W. The Supersonic Flow About a Blunt Body of Revolution for Gases at Chemical Equilibrium. TIS R58SD245, General Electric Missile and Space Vehicle Department (June 1958).

8. Uchida, S. and Yasuhara, M. "The Rotational Field Behind a Curved Shock Wave Calculated by the Method of Flux Analysis," J. Aero. Sci., Vol. 23 (1956), pp. 830-845.

9. Bohachevsky, I. O.; Rubin, E. L.; and Mates, R. E. A Direct Method for Computation of Nonequilibrium Flows With Detached Shock Waves. AIAA Paper No. 65-24, presented at the Institute of Aerospace Sciences 2nd Aerospace Sciences Meeting, New York, N. Y. (January 25-27, 1965).

10. Computer Program Operating Manual, Study of Flow Fields About Axisymmetric Blunt Bodies at Large Angle-of-Attack. NAA S&ID, SID 65-1355 (October 1965) (Contract NAS9-3159).

11. Kaattari, G. E. Predicted Shock Envelopes About Two Types of Vehicles at Large Angles-of-Attack. NASA Technical Note D-860 (April 1961).

12. Kaattari, G. E. Predicted Gas Properties in the Shock Layer Ahead of Capsule-Type Vehicles at Angles-of-Attack. NASA Technical Note D-1423 (October 1962).

13. Kaattari, G. E. Shock Envelopes of Blunt Bodies at Large Angle-of-Attack. NASA Technical Note D-1980 (December 1963).

14. Hayes, W. D. and Probstein, R. F. Hypersonic Flow Theory. New York: Academic Press (1959).

15. Hilsenrath, J. and Beckett, C. Tables of Thermodynamic Properties of Argon-Free Air to 15,000°K. Arnold Engineering Development Center Report AEDC-TN-56-12 (September 1956).

16. Benedict, W. S. and Hilsenrath, J. Tables of Compressibility and Density of Air with Auxiliary Tables. National Bureau of Standards Report 1192 (Reprinted May 1952).

17. Hilsenrath, J., et al. Tables of Thermal Properties of Gases. National Bureau of Standards Circular 564 (November 1955).

18. Handbook of Supersonic Aerodynamics, Vol. 5. NAVORD Report 1488, Bureau of Ordnance, U. S. Navy (August 1953).

19. Grabau, M. A Method of Forming Continuous Empirical Equations for the Thermodynamic Properties of Air From Ambient Temperatures to 15,000°K, with Applications. AEDC-TN-59-102, Arnold Engineering Development Center (August 1959).

20. Ralston, A. and Wilf, H. S. Mathematical Methods for Digital Computers. New York: John Wiley and Sons, Inc. (1962).

21. Scarborough, J. B. Numerical Mathematical Analysis. Baltimore: The John Hopkins Press (1962).

22. Katzen, E. D. and Kaattari, G. E. Flow About Blunt Bodies Including Effects of High Angles-of-Attack, Nonequilibrium Flow, and Vapor Injection. Paper presented at AIAA Entry Technology Conference, Hampton, Virginia (October 12-14, 1964).

23. Hildebrand, F. B. Advanced Calculus for Applications. Englewood Cliffs, New Jersey: Prentice-Hall, Inc. (1963).

APPENDIX A

TRANSFORMATION OF CONSERVATION EQUATIONS IN VECTOR NOTATION INTO A CYLINDRICAL ORTHOGONAL COORDINATE SYSTEM

For any orthogonal coordinates (but not necessarily cartesian), i.e. $\vec{x}\,(x_1, x_2, x_3)$ $\vec{f}\,(f_1, f_2, f_3)$ the divergence of a vector function is, from Reference 23 ,

$$\nabla \cdot \vec{f} = \frac{1}{h_1 h_2 h_3}\left[\frac{\partial(h_2 h_3 f_1)}{\partial x_1} + \frac{\partial(h_3 h_1 f_2)}{\partial x_2} + \frac{\partial(h_1 h_2 f_3)}{\partial x_3}\right] \tag{190}$$

where h_1, h_2, and h_3 are obtained from

$$(ds)^2 = (h_1 dx_1)^2 + (h_2 dx_2)^2 + (h_3 dx_3)^2$$

ds being an elementary length in such a coordinate system. For cylindrical coordinates,

$$(ds)^2 = (dx_1)^2 + (dr)^2 + (r\,d\theta)^2$$

So that

$$h_1 = 1 \quad , \quad h_2 = 1 \quad , \quad h_3 = r$$

And Equation (190) becomes

$$\nabla \cdot \vec{f} = \frac{1}{r}\left[\frac{\partial(r f_1)}{\partial x} + \frac{\partial(r f_2)}{\partial r} + \frac{\partial(f_3)}{\partial \theta}\right]$$

or

$$\nabla \cdot \vec{f} = \frac{\partial f_1}{\partial x} + \frac{1}{r}\frac{\partial(r f_2)}{\partial r} + \frac{1}{r}\frac{\partial f_3}{\partial \theta} \tag{191}$$

The application of Equation (191) to the continuity equation, Equation (1) , in which $f_1 = \rho u$, $f_2 = \rho v$, and $f_3 = \rho w$ is straightforward and results in the expression

$$\nabla \cdot \rho \vec{U} = 0 = \frac{\partial(\rho u)}{\partial x} + \frac{1}{r}\frac{\partial(r\rho v)}{\partial r} + \frac{1}{r}\frac{\partial(\rho w)}{\partial \theta} \tag{192}$$

as previously given in Equation (5) .

The momentum equation, Equation (2) , can also be written as,

$$(\vec{U} \cdot \nabla)\vec{U} = -\frac{1}{\rho}\nabla p \tag{193}$$

The gradient of a scalar function is given in Reference 23 as

$$\nabla f = \frac{1}{h_1}\vec{x}_1 \frac{\partial f}{\partial x_1} + \frac{1}{h_2}\vec{x}_2 \frac{\partial f}{\partial x_2} + \frac{1}{h_3}\vec{x}_3 \frac{\partial f}{\partial x_3} \tag{194}$$

So that in cylindrical coordinates

$$\nabla f = \vec{x}\frac{\partial f}{\partial x} + \vec{r}\frac{\partial f}{\partial r} + \frac{1}{r}\vec{\theta}\frac{\partial f}{\partial \theta} \tag{195}$$

the right hand side of Equation (193) is thus,

$$-\frac{1}{\rho}\nabla p = -\frac{1}{\rho}\left[\vec{x}\frac{\partial p}{\partial x} + \vec{r}\frac{\partial p}{\partial r} + \vec{\theta}\frac{1}{r}\frac{\partial p}{\partial \theta}\right] \tag{196}$$

To evaluate the left hand side of Equation (193) we note that

$$\vec{U} = \vec{x}u + \vec{r}v + \vec{\theta}w \tag{197}$$

Forming the scalar product $\vec{U}\cdot\nabla$ using the gradient operator defined by Equation (195), we obtain,

$$(\vec{U}\cdot\nabla) = u\frac{\partial}{\partial x} + v\frac{\partial}{\partial r} + \frac{1}{r}w\frac{\partial}{\partial \theta}$$

and thus,

$$(\vec{U}\cdot\nabla)\vec{U} = \left(u\frac{\partial}{\partial x} + v\frac{\partial}{\partial r} + \frac{w}{r}\frac{\partial}{\partial \theta}\right)\left(\vec{x}u + \vec{r}v + \vec{\theta}w\right)$$

The right hand side can be expanded and simplified to yield the following components,

$$(\vec{U}\cdot\nabla)\vec{U} = \vec{x}\left(u\frac{\partial u}{\partial x} + v\frac{\partial u}{\partial r} + \frac{w}{r}\frac{\partial u}{\partial \theta}\right) \tag{198}$$

$$+ \vec{r}\left(u\frac{\partial v}{\partial x} + v\frac{\partial v}{\partial r} + \frac{w}{r}\frac{\partial v}{\partial \theta} - \frac{w^2}{r}\right)$$

$$+ \vec{\theta}\left(u\frac{\partial w}{\partial x} + v\frac{\partial w}{\partial r} + \frac{w}{r}\frac{\partial w}{\partial \theta} + \frac{vw}{r}\right)$$

The final form of the momentum equations are obtained by writing the three equivalent scalar equations, using Equations (196) and (198).

$$u\frac{\partial u}{\partial x} + v\frac{\partial u}{\partial r} + \frac{w}{r}\frac{\partial u}{\partial \theta} = -\frac{1}{\rho}\frac{\partial p}{\partial x} \tag{199a}$$

$$u\frac{\partial v}{\partial x} + v\frac{\partial v}{\partial r} + \frac{w}{r}\frac{\partial v}{\partial \theta} - \frac{w^2}{r} = -\frac{1}{\rho}\frac{\partial p}{\partial r} \tag{199b}$$

$$u\frac{\partial w}{\partial x} + v\frac{\partial w}{\partial r} + \frac{w}{r}\frac{\partial w}{\partial \theta} + \frac{vw}{r} = -\frac{1}{\rho r}\frac{\partial p}{\partial \theta} \tag{199c}$$

The evaluation in cylindrical coordinates of the term $\vec{U} \cdot \vec{U}$ in the energy equation, Equation (3), comes directly from Equation (197). Thus,

$$\vec{U} \cdot \vec{U} = u^2 + v^2 + w^2$$

and so the energy equation becomes,

$$h + \frac{1}{2}\left(u^2 + v^2 + w^2\right) = h_\infty + \frac{1}{2} U_\infty^2 \qquad (200)$$

APPENDIX B

VALIDITY OF THE INFLUENCE COEFFICIENT METHOD

In Reference 4 it has been found that a shock equation of the form

$$\frac{S}{R_s} = \frac{0.5\left(\frac{r}{R_s}\right)^2 + A_{5_s}\left(\frac{r}{R_s}\right)^4}{1 + \frac{2A_{5_s}}{\sqrt{M_\infty^2 - 1}}\left(\frac{r}{R_s}\right)^3} \tag{201}$$

where

$A_{5_s} = A_{5_s}(\gamma_\infty, M_\infty)$ = shock wave parameter

R_s = radius of the shock wave at the centerline

will produce spherical or elliptical nosed, axisymmetric bodies in a perfect gas to a high degree of accuracy. This equation can be considered to be a reduced form of

$$\frac{S}{R_s} = \frac{0.5\left(\frac{r}{R_s}\right)^2 + A_{5_s}\left(\frac{r}{R_s}\right)^4 + A_{7_s}\left(\frac{r}{R_s}\right)^6}{1 + \frac{2A_{5_s}}{\sqrt{M_\infty^2 - 1}}\left(\frac{r}{R_s}\right)^3} \tag{202}$$

with $A_{7_s} = 0$.

An equation of similar form in a body-oriented coordinate system can be used to represent the body obtained,

$$\frac{x_b}{R_s} = 0.5\left(\frac{r}{R_b}\right)^2 + A_{5_b}\left(\frac{r}{R_b}\right)^4 + A_{7_b}\left(\frac{r}{R_b}\right)^6 \tag{203}$$

The various coefficients can now all be related by the Taylor Series expansion;

$$\delta \epsilon_i = \sum_{n=1}^{3} \frac{1}{n!} \left(\sum_{j=1}^{3} \left(\frac{\partial}{\partial a_j} \delta a_j \right) \right)^n \epsilon_i \qquad i = 1, 3$$

where now

$$R_s = a_1 \qquad R_b = \epsilon_1 \tag{204a}$$

$$A_{5_s} = a_2 \qquad A_{5_b} = \epsilon_2 \tag{204b}$$

$$A_{7_s} = a_3 \qquad A_{7_b} = \epsilon_3 \tag{204c}$$

It is of interest to determine the magnitude of the coefficients of the Taylor Series for $n > 1$ since the terms using these coefficients have been neglected in the iterative convergence technique used in this computer program. The second order terms have been computed using the results of Reference 4 ($A_{7_s} = 0$) in conjunction with new results obtained using the computer program of Reference 10 for $A_{7_s} \neq 0$.

Equation (203) can easily be fitted to an elliptical body if the ratio of the major to minor axis is known, defining $\sqrt{B_b} = b/a$. Knowing the equation of an ellipse;

$$\frac{(x_b - a)^2}{a^2} + \frac{r}{b^2} = 1$$

or

$$x_b = a - a\left(1 - \frac{r^2}{b^2}\right)^{1/2}$$

Using the binomial expansion;

$$x_b = a - a\left\{1 - \frac{r^2}{2b^2} - \frac{1}{8}\frac{r^4}{b^4} - \frac{1}{16}\frac{r^6}{b^6} + \cdots\right\}$$

and considering only the first three terms

$$x_b = \frac{a r^2}{2 b^2} + \frac{a r^4}{8 b^4} + \frac{a r^6}{16 b^6}$$

to within 4.5% and knowing $B_b = b^2/a^2$, $R_b = b^2/a$ for an ellipse, then

$$\frac{x_b}{R_b} = \frac{1}{2}\left(\frac{r}{R_b}\right)^2 + \frac{1}{8} B_b \left(\frac{r}{R_b}\right)^4 + \frac{1}{16} B_b^2 \left(\frac{r}{R_b}\right)^6$$

or in the form of Equation (203)

$$A_{5_b} = \frac{1}{8} B_b \qquad A_{7_b} = \frac{1}{16} B_b^2 \tag{205}$$

In Figure 29 of Reference 4 are given the various B_b of bodies obtained from various A_{5_s} values in Equation (202). Thus, the results of Reference 4 can be used to obtain the body coefficients for various values of A_{5_s}, $A_{7_s} = 0$. However, in order to compute second derivatives of the various body coefficients other results are needed for $A_{7_s} \neq 0$.

The Ames computer program was used to obtain bodies for non-zero values of A_{7_s}. The output is a series of points representing the body associated with the specific A_{5_s} and A_{7_s}, $R_s = 1$ of Equation (202). A curve is then fitted through three appropriate body points and R_b, A_{5_b} and A_{7_b} algebraically obtained.

Then the functions

$$R_b = R_b\left(A_{5_s}, A_{7_s}, R_s\right) \tag{206a}$$

$$A_{5_b} = A_{5_b}\left(A_{5_s}, A_{7_s}, R_s\right) \tag{206b}$$

$$A_{7_b} = A_{7_b}\left(A_{5_s}, A_{7_s}, R_s\right) \tag{206c}$$

can be plotted for various points if the effect of R_s on the body variables can be found. The initial values (at which the derivatives are found) for each of the variables are $A_{5_s} = 0.08$, $A_{7_s} = 0$, $R_s = 1$. Figure 29 of Reference 4 shows A_{5_s} vs B_b for M_∞ = constant lines and $A_{7_s} = 0$, $R_s = 1$. Figure 30, of the same reference, shows R_b / R_s vs B_b for M_∞ = constant lines and $A_{7_s} = 0$. Thus the desired relationship can be found using $M_\infty = 10$ and $B_b = B_b(A_{5_s})$ from Figure 29, yielding $R_b = R_b(R_s)$ for A_{5_s} = constant, A_{7_s} = constant $= 0$. It must now be realized that R_s is merely a scaling factor and that a change in R_b would only provoke a change in R_s and would not effect A_{5_b} or A_{7_b} which determine the non-dimensional shape of the body and are not functions of what scale is to be used. Thus

$$A_{5_b} \neq A_{5_b}(R_s)$$

$$A_{7_b} \neq A_{7_b}(R_s)$$

and Equations (206) reduce to;

$$R_b = R_b\left(R_s, A_{5_s}, A_{7_s}\right) \tag{207a}$$

$$A_{5_b} = A_{5_b}\left(A_{5_s}, A_{7_s}\right) \tag{207b}$$

$$A_{7_b} = A_{7_b}\left(A_{5_s}, A_{7_s}\right) \tag{207c}$$

The resultant plots are shown in Figures 42, 43, and 44. The results of Figures 29, 30 of Reference 4, coupled with Equations (205), are used for Figures 42 and 43 where $A_{7_s}=0$. The analytic curve fit is used in Figure 43 to obtain the plotted results where $A_{7_s}=0$. Where $A_{7_s}=0$ in this figure, the appropriate results indicated by Reference 4 are shown but not used. The apparent discrepancy between these two methods results from the fact that on the NAA runs of the Ames program the sonic part of the flow field was truncated to facilitate runs using finite A_{7_s}'s which otherwise would give unstable solutions. A second source of difference is the arbitrary location of the three points analytically fitted to solve for the three body shape parameters. Although absolute values may be in error, the trends are believed correct.

The second derivatives may be found from Figures 42, 43, and 44. From Equation (204), the derivatives of the body parameters needed are seen to be:

$n=1$; first order effects:

$$\frac{\partial}{\partial R_s}, \quad \frac{\partial}{\partial A_{5_s}}, \quad \frac{\partial}{\partial A_{7_s}}$$

and

$n=2$; second order effects:

$$\left(\frac{\partial}{\partial R_s}+\frac{\partial}{\partial A_{5_s}}+\frac{\partial}{\partial A_{7_s}}\right)^2 = \frac{\partial^2}{\partial R_s^2}+\frac{\partial^2}{\partial A_{5_s}^2}+\frac{\partial^2}{\partial A_{7_s}^2}+\frac{\partial^2}{\partial R_s\,\partial A_{5_s}}$$
$$+\frac{\partial^2}{\partial R_s\,\partial A_{7_s}}+\frac{\partial^2}{\partial A_{5_s}\,\partial A_{7_s}}+\frac{\partial^2}{\partial A_{5_s}\,\partial R_s}+\frac{\partial^2}{\partial A_{7_s}\,\partial R_s}+\frac{\partial^2}{\partial A_{7_s}\,\partial A_{5_s}}$$

Some of these derivatives may be eliminated since for any variables a and b

$$\frac{\partial^2}{\partial a\,\partial b} = \frac{\partial^2}{\partial b\,\partial a}$$

also;

$$\frac{\partial^2 R_b}{\partial A_{5_s}\,\partial R_s} = \frac{\partial^2 R_b}{\partial R_s\,\partial A_{5_s}} = \frac{\partial}{\partial A_{5_s}}\left[\frac{\partial R_b}{\partial R_s}\right] = \frac{\partial}{\partial A_{5_s}}\left(\frac{R_b}{R_s}\right) = \left(\frac{\partial R_b}{\partial A_{5_s}}\right)_{R_s=1}$$

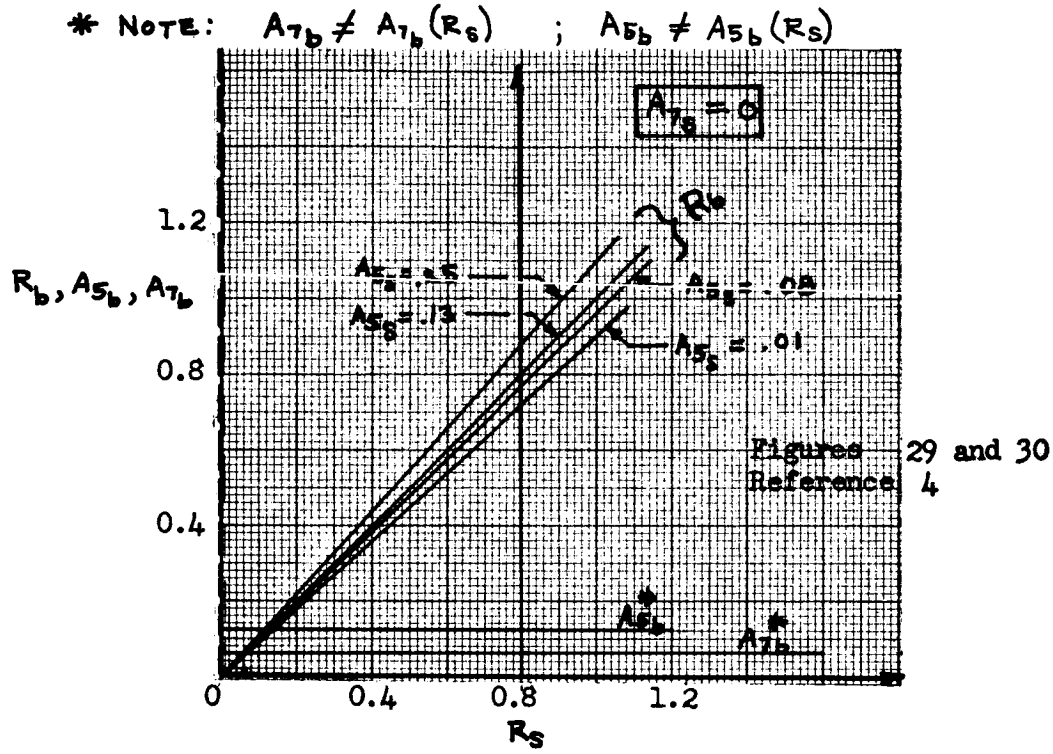

Figure 42. Variation of Body Shape Parameters with R_S

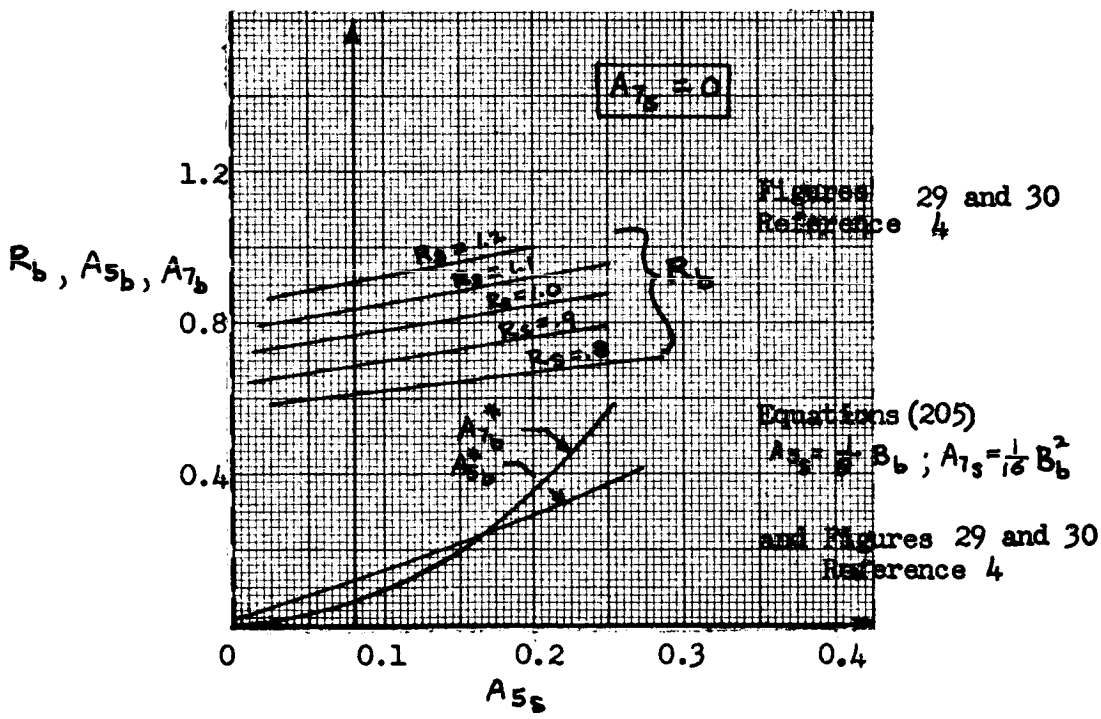

Figure 43. Variation of Body Shape Parameters with A_{5_S}

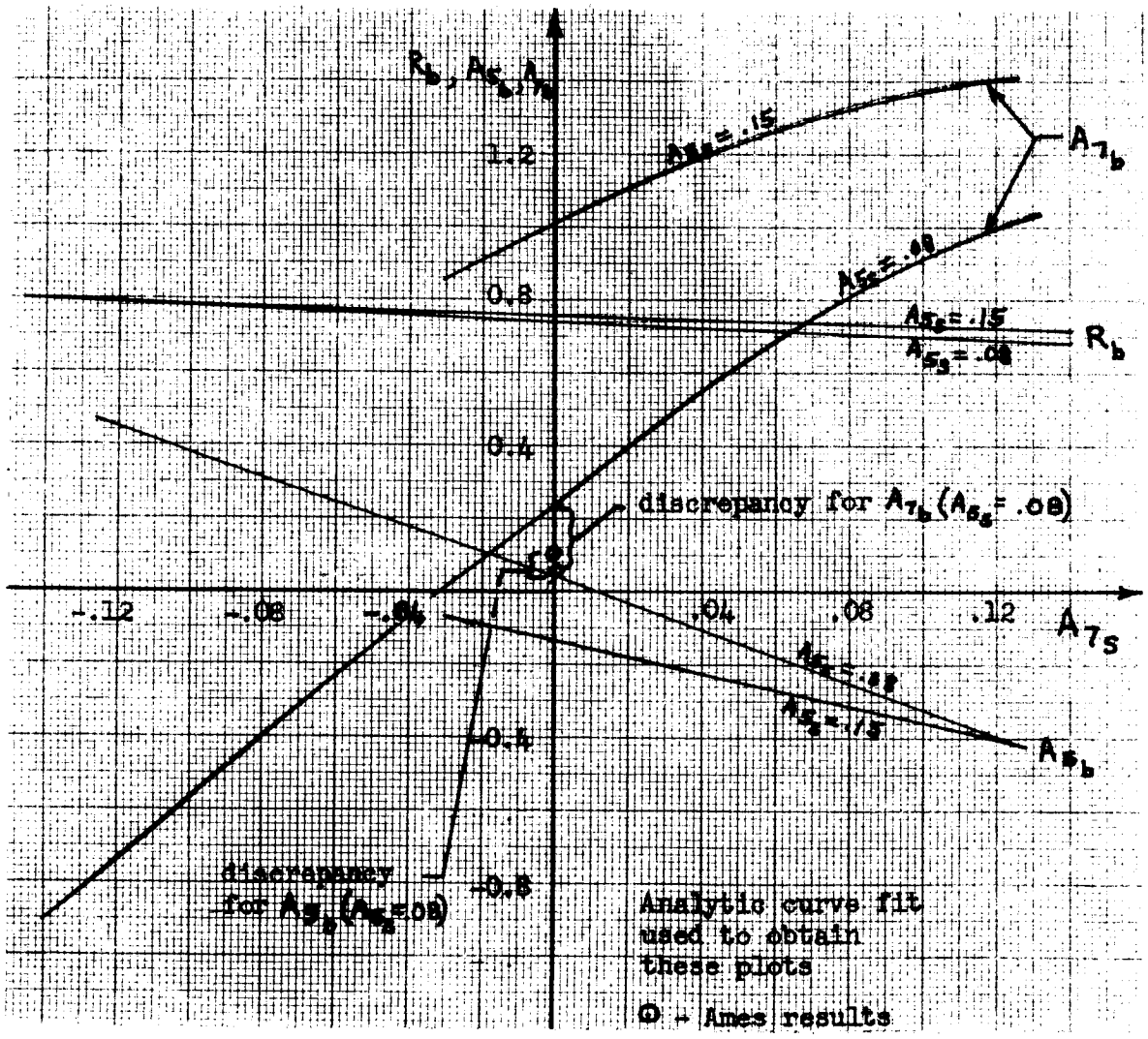

Figure 43. Variation of Body Shape Parameters with A_{7_S}

and similarly

$$\frac{\partial^2 R_b}{\partial A_{7_s} \partial R_s} = \frac{\partial^2 R_b}{\partial R_s \partial A_{7_s}} = \left(\frac{\partial R_b}{\partial A_{7_s}}\right)_{R_s=1}$$

Thus the needed derivatives for first and second order effects become;

$$\frac{\partial}{\partial R_s}, \frac{\partial}{\partial A_{5_s}}, \frac{\partial}{\partial A_{7_s}}, \frac{\partial^2}{\partial R_s^2}, \frac{\partial^2}{\partial A_{5_s}^2}, \frac{\partial^2}{\partial A_{7_s}^2}, \frac{\partial^2}{\partial A_{5_s} \partial A_{7_s}}$$

for A_{5_b}, A_{7_b}, R_b and in addition

$$\frac{\partial^2}{\partial A_{5_s} \partial R_s}, \frac{\partial^2}{\partial A_{7_s} \partial R_s}$$

for A_{5_b}, A_{7_b}

Now the derivatives may be obtained:

For R_b

$$\frac{\partial R_b}{\partial R_s} = 0.76 \qquad \left[\begin{array}{ll} \dfrac{\partial^2 R_b}{\partial R_s^2} = 0 & \text{Figure 42} \\[2ex] \dfrac{\partial^2 R_b}{\partial R_s \partial A_{5_s}} = 0.625 & \text{Figure 42 or 43} \\[2ex] \dfrac{\partial^2 R_b}{\partial R_s \partial A_{7_s}} = -0.50 & \text{Figure 44} \end{array}\right.$$

$$\frac{\partial R_b}{\partial A_{5_s}} = \left(\frac{\partial^2 R_b}{\partial R_s \partial A_{5_s}}\right)_{R_s=1} = 0.625 \qquad \left[\begin{array}{ll} \dfrac{\partial^2 R_b}{\partial A_{5_s}^2} \approx 0 & \text{Figure 42 or 43} \\[2ex] \dfrac{\partial^2 R_b}{\partial A_{5_s} \partial A_{7_s}} = 2.86 & \text{Figure 44} \end{array}\right.$$

$$\frac{\partial R_b}{\partial A_{5_s}} = \left(\frac{\partial^2 R_b}{\partial R_s \partial A_{5_s}}\right)_{R_s=1} = -0.50 \qquad \left[\ \dfrac{\partial^2 R_b}{\partial A_{7_s}^2} \approx 0 \quad \text{Figure 44}\right.$$

For A_{5_b}

$$\frac{\partial A_{5_b}}{\partial R_s} = 0 \qquad \left[\begin{array}{l} \dfrac{\partial^2 A_{5_b}}{\partial R_s^2} = 0 \\ \dfrac{\partial^2 A_{5_b}}{\partial R_s \partial A_{5_s}} = 0 \\ \dfrac{\partial^2 A_{5_b}}{\partial R_s \partial A_{7_s}} = 0 \end{array}\right. \qquad A_{5_b} \neq A_{5_b}(R_s)$$

$$\frac{\partial A_{5_b}}{\partial A_{5_s}} = 1.4 \qquad \left[\begin{array}{ll} \dfrac{\partial^2 A_{5_b}}{\partial A_{5_s}^2} = 10 & \text{Figure 43} \\ \dfrac{\partial^2 A_{7_b}}{\partial A_{5_s} \partial A_{7_s}} = -43 & \text{Figure 44} \end{array}\right.$$

$$\frac{\partial A_{5_b}}{\partial A_{7_s}} = -3.6 \qquad \left[\ \dfrac{\partial^2 A_{5_b}}{\partial A_{7_s}^2} \approx 0 \quad \text{Figure 44}\right.$$

For A_{7_b}

$$\frac{\partial A_{7_b}}{\partial R_s} = 0 \qquad \left[\begin{array}{l} \dfrac{\partial^2 A_{7_b}}{\partial R_s^2} = 0 \\ \dfrac{\partial^2 A_{7_b}}{\partial R_s \partial A_{5_s}} = 0 \\ \dfrac{\partial^2 A_{7_b}}{\partial R_s \partial A_{7_s}} = 0 \end{array}\right. \qquad A_{7_b} \neq A_{7_b}(R_s)$$

$$\frac{\partial A_{7_b}}{\partial A_{5_s}} = 1.1 \qquad \left[\begin{array}{ll} \dfrac{\partial^2 A_{7_b}}{\partial A_{5_s}^2} = 10 & \text{Figure 43 or 44} \\ \dfrac{\partial^2 A_{7_b}}{\partial A_{5_s} \partial A_{7_s}} = -43 & \text{Figure 44} \end{array}\right.$$

$$\frac{\partial A_{7_b}}{\partial A_{7_s}} = 8.0 \qquad \left[\ \dfrac{\partial^2 A_{7_b}}{\partial A_{7_s}^2} \approx 0 \quad \text{Figure 44}\right.$$

The final equations may be computed by substitution in Equation (204). Thus, at $R_s = 1$, $A_{5_s} = 0.08$ and $A_{7_s} = 0$, the equations for the influence coefficient method become

$$-\delta R_b = \left[0.76\,\delta R_s + 0.625\,\delta A_{5_s} - 0.50\,\delta A_{7_s}\right] + \left[0.625\,\delta R_s\,\delta A_{5_s} - 0.50\,\delta R_s\,\delta A_{7_s} + 2.86\,\delta A_{5_s}\,\delta A_{7_s}\right]$$

$$-\delta A_{5_b} = \left[1.4\,\delta A_{5_s} - 3.6\,\delta A_{7_s}\right] + 0.75\left(\delta A_{5_s}\right)^2 + 20\,\delta A_{5_s}$$

$$-\delta A_{7_b} = \left[1.1\,\delta A_{5_s} + 8.0\,\delta A_{7_s}\right] + \left[5\left(\delta A_{5_s}\right)^2 - 43\,\delta A_{5_s}\,\delta A_{7_s}\right]$$

including second order terms

Thus it is seen that unless the errors, δR_b, δA_{5_b}, δA_{7_b} are small, thereby making the shock corrections, δR_s, δA_{5_s}, δA_{7_s}, small, it is very possible that higher order terms will effect the convergence of the influence coefficient method.